- THESIS -
DOCTOR OF PHILOSOPHY

Dynamical Fingerprints of Black Holes in Globular Clusters

by
Ruggero de Vita
ORCID: 0000-0002-0996-4741

September 11, 2019

School of Physics
Faculty of Science
The University of Melbourne

Submitted in Total Fulfillment of the Requirements of the Degree of Doctor of Philosophy

Abstract

Globular clusters (GCs), compact stellar systems orbiting in and around galaxies, are natural laboratories to study a diverse range of astrophysical processes. The current stellar population of the oldest GCs in our Galaxy is the manifestation of more than 12 billion years of combined stellar, dynamical and hydrodynamical evolution, whose interplay is responsible for enhanced presence of star exotica such as millisecond pulsars, blue stragglers and black hole (BH) binaries.

GCs have also been indicated as possible formation sites of intermediate-mass black holes (IMBHs), which might represent the missing link between the well-known populations of stellar BHs (few tens times the Sun's mass) and supermassive BHs (more than a million times the Sun's mass). Despite recent efforts, a clear evidence of their existence is still missing, therefore identifying multiple signatures of their presence has become critical.

In the first part of this thesis, we address two main issues that may affect a possible IMBH detection. The first issue is represented by the systematic uncertainties in classical observational techniques (e.g., integrated-light IFU spectroscopy). In particular, we use state-of-the-art numerical simulations to produce realistic mock observations considering different setups in order to assess under which conditions the presence of an IMBH can be successfully recovered. The second issue is related to the IMBH wandering off-center, which is fundamental to take into account, especially when the presence of IMBHs is constrained through dynamical modeling of stellar kinematics. Guided by the simulation results, we developed a basic yet accurate model that can be used to estimate the average IMBH radial displacement in terms of structural quantities, which can be constrained by the observations.

In the second part of the thesis, we present a new set of cutting-edge direct N-body simulations, which have been specifically designed to study the dynamical influence of BHs on the long-term evolution of GCs. We combined our numerical simulations with analysis techniques from high-resolution observations of GCs with the aim of identifying key indicators that correlate with the black hole mass fraction. Our results offer novel approaches to indirectly characterise black hole populations in star clusters, which in turn can constrain theories of globular cluster formation and estimates of dynamically-induced gravitational wave merging rates.

Preface

This thesis comprises 4 chapters based on original work, including publications.

Chapter 1 features an original introduction and literature review of globular clusters and black holes.

Chapters 2, 3, 4 have been published as separate papers in peer-reviewed journals. As first author of all the publications, I was responsible primarily for the planning, execution and preparation of the work, contributing to more than 50% of their content.

- Chapter 2 is published as: de Vita R., Trenti M., Bianchini P., Askar A., Giersz M., van de Ven G., "Prospects for detection of intermediate-mass black holes in globular clusters using integrated-light spectroscopy", 2017, *Monthly Notices of the Royal Astronomical Society*, 467, 4057.

- Chapter 3 is published as: de Vita R., Trenti M., MacLeod M., "Wandering off the centre: A characterisation of the random motion of intermediate-mass black holes in star clusters", 2018, *Monthly Notices of the Royal Astronomical Society*, 475, 1574.

- Chapter 4 is published as: de Vita R., Trenti M., MacLeod M., "Correlation Between Mass Segregation and Structural Concentration in Relaxed Stellar Clusters", 2019, *Monthly Notices of the Royal Astronomical Society*, 485, 5752.

This work was financially supported by the University of Melbourne through multiple research grants: A.A.H. Pierce Bequest, N.D. Goldsworthy bursary, Science Abroad and Laby PhD Travelling scholarships.

This research made use of Astropy, a community-developed core PYTHON package for Astronomy (Astropy Collaboration et al., 2013).

The computational part of this thesis was carried out using three supercomputers in Melbourne: OzSTAR (Swinburne University), Spartan and Coepp (The University of Melbourne).

Acknowledgements

I would like to thank all the collaborators that provided a substantial contribution to this thesis.

A special thanks to my supervisor, Michele Trenti. Your scientific guidance, moral support and Nespresso machine have been of vital importance in the past years.

I am also grateful to all the collaborators met during fruitful international visits and conferences: Glenn van de Ven and Paolo Bianchini at the MPIA in Heidelberg (Germany), Mirek Giersz and Abbas Askar at the Nicolaus Copernicus Astronomical Centre in Warsaw (Poland) and Morgan MacLeod at the Harvard-Smithsonian Center for Astrophysics in Cambridge (Massachusetts, USA).

On a more personal note, I would like to thank friends and family for huge support and understanding.

Finally, managing distant relationships has not been an easy task, and it could not have been possible without you, Raffaella. To you I dedicate this work, myself, these few lines, which will always remind me how lucky I am to have you in my life.

Contents

List of Figures

List of Tables

1

Introduction

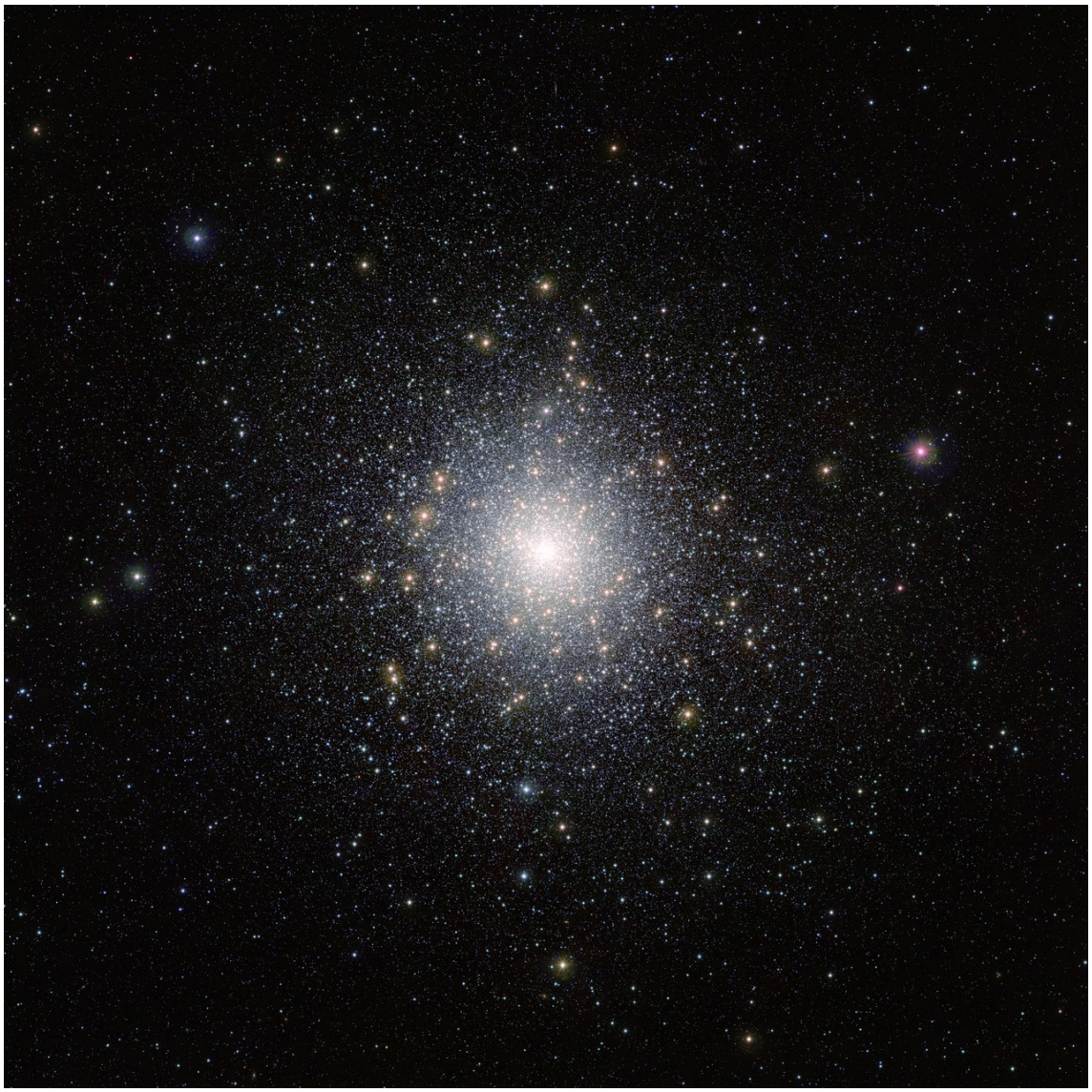

Figure 1.1: Globular Cluster 47 Tucanae (NGC 104), shown here in an image taken by ESO's VISTA (Visible and Infrared Survey Telescope for Astronomy) from the Paranal Observatory in Chile. Credit: ESO.

Globular clusters (GCs) are collections of 10^4-10^6 stars held together by their mutual gravitational attraction and distributed in a spherical region with typical radius of few tens of light-years, much bigger than the solar system but much smaller than a galaxy (see Fig. 1.1). They are thought to be poor in gas and dark matter and their internal dynamics are well described by Newtonian gravity (Spitzer, 1987).

Some of their unique features capture interest from different branches of Astronomy. Studies of colour-magnitude diagrams combined with recent models of stellar evolution suggest that GCs were among the oldest structures in our Galaxy, with ages comparable to the age of the Universe (see, e.g., Forbes & Bridges 2010, Trenti et al. 2015). For this reason, GCs can offer a record of the chemical and dynamical conditions of newborn galaxies, probing current theories of galaxy formation and evolution. All the stars in each cluster were born with

different masses at roughly the same time, so that their present stellar population allows to investigate the results of more than 10 billion years of stellar evolution. In addition, GCs are rich in exotic members (e.g., X-ray binaries, blue stragglers, millisecond pulsars, etc.) but they might also host a class of objects that has not been unequivocally observed yet: intermediate-mass black holes (see, e.g., pioneering works such as Silk & Arons 1975 and Bahcall & Wolf 1976a). Finally, GCs are natural laboratories for the study of the so-called "gravitational N-body problem" (Heggie & Hut, 2003). Indeed, because of their high densities and relatively low number of particles, GCs' long-term dynamical evolution is dominated by the effects of gravitational interactions and collisions between stars.

In this first chapter, we will review well established properties of GCs, with particular emphasis on aspects that are highly relevant for our studies. In the first section, we will present the main classes of observations currently available along with GCs' main dynamical and structural properties. We will dedicate the second section to review the methods currently used to study GCs' dynamical evolution, focusing in particular on the role of numerical simulations as main tool of investigation. Finally, in the third and last section, we will examine the recent progress in the search for intermediate-mass black holes in the Universe.

1.1 Globular clusters

Globular clusters typically reside inside an host galaxy (see Ashman & Zepf 2008). They orbit elliptical as well as spiral galaxies in systems that comprise from few tens to thousands of constituents, depending on the size of the host. GCs' systems are often used as tools to validate theories on formation and evolution of galaxies. For example, they can trace the gravitational field of galaxies providing important constraints on the dark matter mass distribution (Bertin, 2014). As individual objects, the current knowledge of GCs is largely restricted to our Galaxy, in which it is still possible to identify individual stars in the cluster's most crowded regions using telescopes with $\lesssim 0.''1$ angular resolution.

1.1.1 Observed quantities

One of the basic observations of a stellar system is its total luminosity. Such quantity can be measured by the absolute visual magnitude M_V, which, for Galactic GCs, has median value $M_V \approx -7.3$ mag (Harris, 2010).

Another important observable is the luminosity surface-density measured at different radial positions, i.e. the surface brightness profile. Since light can be used as a natural first-order tracer of the baryonic mass, this information represents a crucial constraint for any dynamical model of the star cluster. Typical surface brightness profiles are characterised by a very low luminosity gradient in the central region (called *core*) and a truncation in the outer part, that is a region where the surface brightness becomes vanishingly small (see Fig. 1.2). For a few globular clusters, those that are in a *core collapse* phase, the surface brightness increases towards the centre exhibiting a central cusp, typically associated with marked X-ray emission (see, e.g., Hertz & Grindlay 1983; Grindlay et al. 2001).

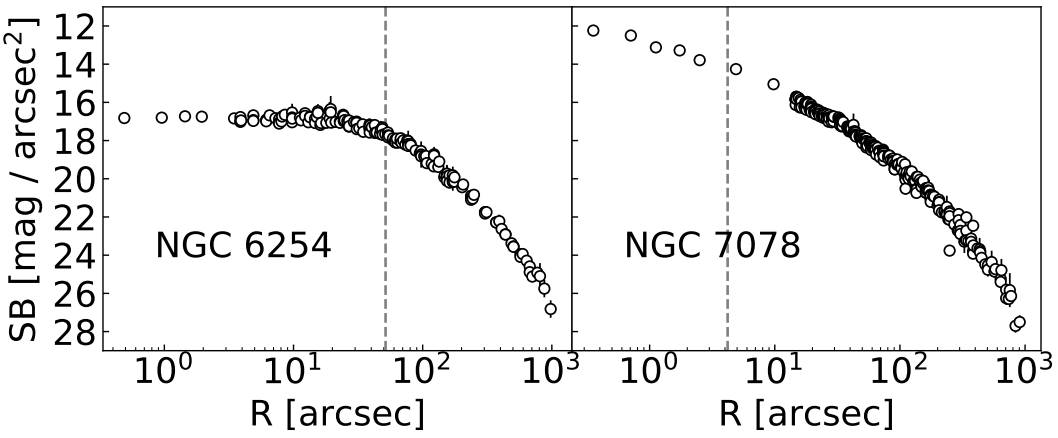

Figure 1.2: Typical surface brightness profiles for two representative Galactic globular clusters: NGC 6254 and NGC 7078. The vertical lines represent the core radii as reported in the Harris (2010) catalogue. NGC 7078 displays a central cusp, consequence of core collapse. [Data: see de Vita et al. 2016 and references therein].

High-quality photometric data can also be adopted to measure proper motions of single stars on the plane of the sky (see Anderson & van der Marel 2010, Bellini et al. 2014). This kind of observations relies on the astrometric comparison of two or more images taken at times with a typical separation of few years. Currently, the main instruments able to measure proper motions are the NASA Hubble Space Telescope and the ESA satellite *Gaia*.

Another important set of observations relies on spectroscopic data. Spectroscopy is used to infer kinematic properties by measuring the line-of-sight velocities (also known as radial velocities) of the most luminous stars through Doppler shift analysis. Spectroscopic surveys are typically carried out by means of ground-based telescopes (e.g., SINFONI and FLAMES at the ESO Very Large Telescope), which rely on two main classes of instruments: multi-object spectographs, used to target specific members in the less crowded regions of GCs and integrated-light spectrographs (IFUs), which can collect cumulative spectra over a two-dimensional field-of-view.

Once velocity data are collected, it is possible to construct velocity dispersion profiles, which quantify stellar random motions as function of the clustercentric distance. The central value of the projected (one-dimensional) velocity dispersion is around 5 km/s for most Galactic GCs, and decreases towards the outskirts as expected for systems in dynamical equilibrium.

1.1.2 Structural and dynamical properties

From a morphological point of view, globular clusters present only small deviations from spherical symmetry (see, e.g., Chen & Chen 2010). Close to the Galactic bulge, they are often more flattened, with major axes preferentially pointing toward the Galactic centre, presumably due to tidal forces.

The structure of a cluster can be defined by considering the values of some

characteristic radii. The truncation radius $r_{\rm tr}$ gives an estimate of the cluster's extent, whereas the core radius $r_{\rm c}$ and the half-light radius $r_{\rm h}$ identify, respectively, the radius at which the surface brightness drops to half of its central value and the radius that contains half of the total luminosity.*

Self-consistent models of globular clusters

Traditionally, dynamical and structural properties of globular clusters are inferred from a one-component family of spherical isotropic models (King, 1966), whose free parameters are chosen as those that best reproduce the observational data (typically the surface brightness profile).

In this modelling framework, globular clusters are described in the continuous limit by specifying a distribution function $f(\boldsymbol{x}, \boldsymbol{v}, t)$ so that the quantity $f(\boldsymbol{x}, \boldsymbol{v}, t) d^3\boldsymbol{x} d^3\boldsymbol{v}$ represents the number of stars that, at time t, occupies an elementary volume centred in $\boldsymbol{x}$ with velocity close to $\boldsymbol{v}$.

The macroscopic quantities can be derived by taking various moments of the distribution functions. In particular, it is possible to define a mass density ρ and a velocity dispersion tensor σ^2_{ij}:

$$\rho(\boldsymbol{x}, t) = \int f \; d^3\boldsymbol{v}, \tag{1.1}$$

$$\sigma^2_{ij}(\boldsymbol{x}, t) = \frac{1}{\rho} \int (v_i - u_i)(v_j - u_j) f \; d^3\boldsymbol{v}, \tag{1.2}$$

where $u_i (i = 1, 2, 3)$ is the mean stellar velocity (i.e. the first moment of f).

The distribution function evolves in the six-dimensional phase space under the action of the mean-field potential $\Phi(\boldsymbol{x}, t)$. At any time f is chosen to satisfy the (collisionless) Boltzmann equation

$$\frac{\partial f}{\partial t} + \boldsymbol{v} \cdot \frac{\partial f}{\partial \boldsymbol{x}} - \frac{\partial \Phi}{\partial \boldsymbol{x}} \cdot \frac{\partial f}{\partial \boldsymbol{v}} = 0. \tag{1.3}$$

For fully self-consistent stellar systems, the mean potential Φ is determined from the distribution of stars in the system by means of the Poisson equation

$$\nabla^2 \Phi = 4\pi G \int f \; d^3\boldsymbol{v}. \tag{1.4}$$

Together, Equations (1.3)-(1.4) define a self-consistent problem for the stellar system. The problem is highly non-linear as the mean potential, which determines the evolution of the distribution f, is not an assigned "external" function but, instead, is determined by the distribution function itself.

Relaxation time

Because of their ages, globular clusters are thought to be systems in which two-body encounters have had time to change significantly the single-star energies bringing the cluster into a state of relaxation, at least in its inner regions.

*As reported in the Harris (2010) catalogue, median values for Galactic GCs are: $\langle r_{\rm tr} \rangle \approx 30$ pc, $\langle r_{\rm c} \rangle \approx 1.5$ pc and $\langle r_{\rm h} \rangle \approx 3.5$ pc.

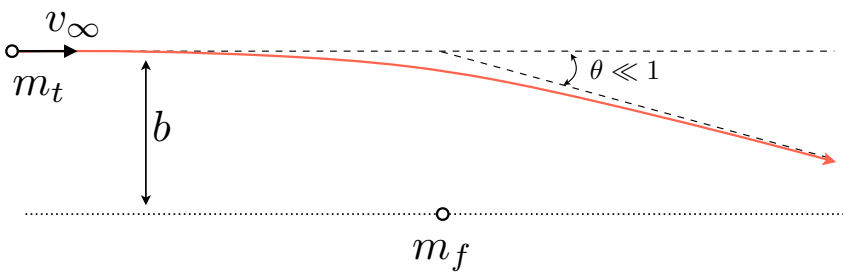

Figure 1.3: Single encounter between a test star of mass m_t and a field star of mass m_f.

A single encounter can bee seen as a Rutherford scattering event between a test mass m_t with initial velocity v_∞ and a field mass m_f at rest (see Fig. 1.3). In a single encounter, the change in the test mass kinetic energy associated with a deflection is due to a change of the velocity $\Delta v_\perp$ perpendicular to the direction of the original motion. With an heuristic approach (shown in Bertin 2014), under the simplification of small scattering angles, the relevant interaction between two stars takes place in a time of order $2b/v_\infty$, where b is the impact parameter, that is, the minimum distance between the test and a field star. Then, the increment of the transverse velocity due to a single encounter may be expressed as

$$\Delta v_\perp \approx \frac{G m_f}{b^2} \frac{2b}{v_\infty}, \tag{1.5}$$

where $G = 6.67 \times 10^{-11} \mathrm{m^3 kg^{-1} s^{-2}}$ is the gravitational constant.

The relaxation time is defined as the time scale beyond which the total change in kinetic energy due to the cumulative effect of single encounters becomes comparable with the initial energy of the test star. Thus, indicating with n the number density of the star field, the relaxation time t_{rel} is defined by

$$v_\infty^2 = t_{\mathrm{rel}} \int_{b_{\min}}^{b_{\max}} (\Delta v_\perp)^2 \, 2\pi v_\infty n b \, db. \tag{1.6}$$

The integration of the right member yields

$$t_{\mathrm{rel}} \approx \frac{v_\infty^3}{8\pi n G^2 m_f^2 \ln \Lambda} \tag{1.7}$$

where $\ln \Lambda = \ln(b_{\max}/b_{\min})$ is the so-called Coulomb logarithm.

It is worth noting that the relaxation time depends on both the initial velocity of the test star and the density of the system. For the first dependence it is possible to show that, in stellar systems where the velocity distribution is approximately a Maxwellian, the velocity dispersion σ can be used as a good approximation of the velocity v_∞ (see Spitzer 1987). For a globular cluster, the local value of the relaxation time typically increases with radius. As reference values, it is appropriate to

distinguish between central $t_{\rm rel,c} \sim \sigma(0)^3/n(0)$ and half-mass $t_{\rm rel,h} \sim \sigma(r_{\rm h})^3/n(r_{\rm h})$ relaxation times (see Fig. 1.4).

A convenient expression for the half-mass relaxation time can be obtained by using the virial theorem $\sigma(r_{\rm h}) \approx 0.4GM/r_{\rm h}$, where M indicates the total mass of the cluster (see Spitzer 1987). If we consider $b_{\rm max} \approx r_{\rm h}$ and $b_{\rm min} \approx \sigma(r_{\rm h})^2/(Gm_f)$, [†] from the virial theorem, the Coulomb logarithm depends only on the total number of stars in the cluster: $\ln\Lambda \approx \ln N$. Thus, after replacing v_∞ with $\sigma(r_{\rm h})$ and applying the virial theorem to Equation (1.7), we obtain the final expression:

$$t_{\rm rel,h} \approx \frac{N^{1/2} r_{\rm h}^{3/2}}{(Gm_f)^{1/2} \ln N}. \tag{1.8}$$

Finally, the relation between the half-mass relaxation time and the dynamical time $t_{\rm dyn,h} = r_{\rm h}/\sigma(r_{\rm h})$, is given by

$$\frac{t_{\rm rel,h}}{t_{\rm dyn,h}} \approx \frac{N}{\ln N}. \tag{1.9}$$

From this relation, it is possible to directly infer the typical ordering of time scales in globular clusters : $t_{\rm dyn} < t_{\rm rel} \lesssim t_{\rm Hubble}$.[‡] From this point of view, after the cluster has reached equilibrium in a few dynamical times, it evolves, driven by collisionality, through adjacent configurations of equilibrium (at least in the inner part of the cluster where the relation $t_{\rm rel} < t_{\rm Hubble}$ typically holds). Such equilibria are described by means of zero-order dynamical models (see previous paragraph) in which the effects of encounters are neglected as they are very small during the orbital periods of the stars. Collisionality is thus treated as a small perturbation on the equilibria that acts over a period of many orbits and produces gradual changes from one zero-order solution to another (see next subsection). Hence at any given time collisionless models can provide an excellent fit for any cluster even if collisionality is present and responsible for the general evolution of the system.

1.1.3 Dynamical evolution at a glance

The initial stages of globular cluster evolution may be driven by a collisionless process known as violent relaxation (see Lynden-Bell 1967). According to this picture, initially the stellar system is far from dynamical equilibrium and collapses under its own gravity. This phase is characterized by rapid fluctuations of the gravitational potential which change star energies providing a source of relaxation. The result of violent relaxation is a gravitationally bound stellar system characterized by virial equilibrium.

The overall evolution of the cluster is due to various time-dependent effects that can be regarded as small perturbations of a steady-state configuration. Such perturbations become relevant over a time scale that is large compared to the orbital period of the stars, measured by the dynamical time $t_{\rm dyn}$.

[†] Note that this expression is consistent with the assumption of small scattering angles: $b_{\rm min}$ is the distance at which the specific kinetic energy $\sigma(r_{\rm h})^2$ of the test star equals its potential energy $Gm_f/b_{\rm min}$.

[‡] $t_{\rm Hubble} \approx 13.8$ Gyr

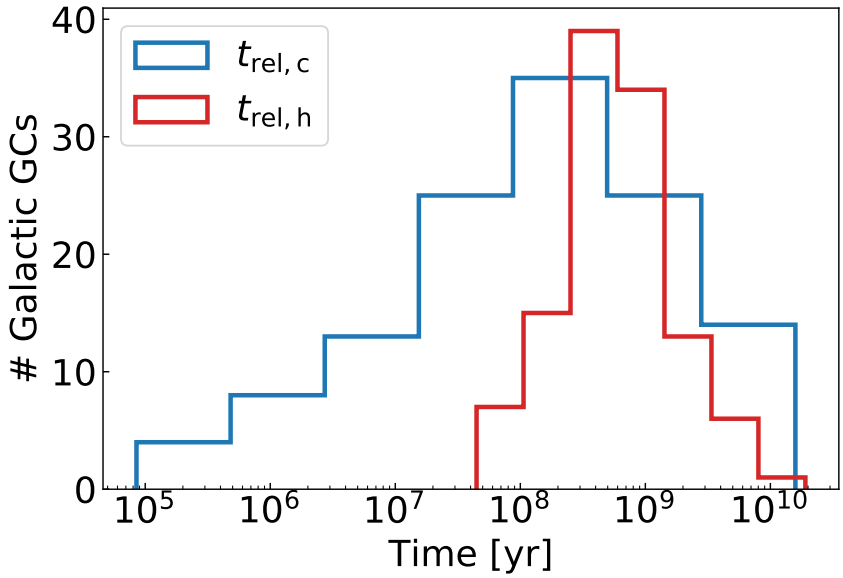

Figure 1.4: Distribution of the central and half-mass relaxation times for Galactic GCs, as reported in the Harris (2010) catalogue.

A crucial effect for the dynamical evolution is represented by the "granular" nature of the gravitational potential produced by N bodies. At any point in space the gravitational field experiences small fluctuations that produce appreciable effects over a relaxation time $t_{\rm rel}$.

There are three main processes related to the two-body relaxation (see Spitzer 1987). The first, known as evaporation, consists in the departure of stars whose velocities exceed the local escape velocity of the cluster.

The second process is the tendency towards energy equipartition among stars with different mass. As a result, high-mass stars sink towards the centre as they lose kinetic energy and, conversely, low-mass stars drift towards the outskirts as they gain kinetic energy. Through this mechanism the cluster reaches a configuration of radial mass segregation. It may be possible that a state of complete equipartition in the core of globular clusters is never achieved as a consequence of the so-called Spitzer instability. Indeed, Spitzer (1969) suggested that, in a two-component system in virial equilibrium, the condition of equipartition in the core is precluded if the total mass of the heavy stars exceeds a certain fraction of the total mass of the cluster. Spitzer's criterion has been extended by Vishniac (1978) to cover systems with a continuous distribution of masses. These theoretical arguments have been later confirmed in numerical simulations (see, e.g., Trenti & van der Marel 2013), in which no system is found to reach a state close to equipartition. Nevertheless, even if complete equipartition is precluded, a certain degree of mass segregation is observed in several globular clusters (see, e.g., Goldsbury et al. 2013).

Finally, the third process is called gravothermal instability (or core collapse). An isolated system of self-gravitating bodies is characterised by negative specific heat, since as it gives up energy it contracts and by the virial theorem increases

its kinetic energy (see, e.g., Binney & Tremaine 2008, Bertin 2014). If there is a net density contrast between the inner and the outer regions of the cluster, the core can contract and heat up, transferring energy to the outer regions, which will heat up but by a lesser amount. Eventually, the core collapse is halted by the formation of tightly bound binary systems, which provide a source of energy by enhancing three-body encounters.

Two-body relaxation is not the only process that influences the long-term dynamical evolution. As the cluster moves through space, it is subject to the gravitational force exerted by the hosting galaxy. This kind of interaction is of particular importance for the rate of star evaporation as, for most cases, the tidal forces can be considered constant in magnitude and direction. More dramatic effects can follow rapid transients caused by a passage either through the galactic disc or close to the galactic nucleus.

In addition, physical changes of stars can affect the overall cluster evolution. From a dynamical point of view, the relevant changes of stars are those concerning their mass. There are at least two ways in which a star can eject its mass. One is through normal evolution of individual stars (Chiosi & Maeder, 1986; Vink, 2018). The second results from a physical impact between two stars. The material ejected can eventually escape from the cluster. The consequent reduction in the total mass may lead to a decrease of the gravitational binding energy and, thus, to an expansion of the cluster.

1.2 Numerical simulations

Different approaches have been proposed to address the gravitational N-body problem (Trenti & Hut, 2008). Depending on the complexity and the accuracy, one method might be more suitable than the others to describe a specific aspect of the overall evolution of a globular cluster.

1.2.1 Mean-field approach

One popular approach is based on a phase-space description of the stellar system. According to this representation, each star is identified by a point in the 6-dimensional space of spatial coordinate $\boldsymbol{r}$ and velocity coordinate $\boldsymbol{v}$. A distribution function $f(\boldsymbol{r}, \boldsymbol{v}, t)$ can be then interpreted as a probability density (i.e. $\int f d^3\boldsymbol{r} d^3\boldsymbol{v} = N$) so that the the problem, originally formulated in a 6N + 1 dimensional space, is reduced to 6 + 1 dimensions. Following this mean-field description, the distribution function is chosen to satisfy the Fokker-Planck equation

$$\frac{\partial f}{\partial t} + \boldsymbol{v} \cdot \frac{\partial f}{\partial \boldsymbol{x}} - \frac{\partial \Phi}{\partial \boldsymbol{x}} \cdot \frac{\partial f}{\partial \boldsymbol{v}} = C, \tag{1.10}$$

where $\Phi = \Phi(\boldsymbol{x}, t)$ is the potential field and C is a collisional term describing the effects of gravitational encounters on the distribution function.

The system of the Fokker-Planck (which corresponds to the Boltzmann equation for the choice $C = 0$) and the Poisson equation (see Equation 1.4) can be solved by means of Monte Carlo techniques in which, at each time interval (much

smaller than the relaxation time and larger than the dynamical time), the velocity of the stars is perturbed by random fluctuations accordingly to the assumed form of the collisional operator C (see, e.g., Giersz 1998).

1.2.2 Direct approach

A mean-field approach has the main advantage of delivering reliable numerical solutions with a minimum amount of computational resources. However, the recent technological advancement allows to address the million-body gravitational problem with direct approaches.

The fundamental N-body problem is expressed by a set of non-linear second order ordinary equations, each relating the acceleration $\partial^2 \boldsymbol{r}_i / \partial t^2$ of a particle i with mass m_i to the gravitational force F_i exerted by all the other stars. In particular, given the Newtonian force

$$\boldsymbol{F}_i = -\sum_{j \neq i}^{N} G \frac{m_i m_j (\boldsymbol{r}_i - \boldsymbol{r}_j)}{|\boldsymbol{r}_i - \boldsymbol{r}_j|^3}, \tag{1.11}$$

the equations of interest are

$$\frac{\partial^2 \boldsymbol{r}_i}{\partial t^2} = \frac{\boldsymbol{F}_i}{m_i} \ \ (i = 1..N). \tag{1.12}$$

When $N > 2$, the solution to this problem requires numerical integration once the initial positions $\boldsymbol{r}_i$ and velocities $\boldsymbol{v}_i = \partial \boldsymbol{r}_i / \partial t$ are specified.

The computational complexity of such integration can be understood in terms of two main issues. The first is related to the brute-force calculation of N equation of motions. For a fixed number of time-steps, each force evaluation requires to take into account the contributions from all the other members of the system, so that the numerical solution scales as N^2. The second issue is represented by the huge dynamical range of temporal and radial scales. In the particular case of globular clusters, we are confronted with length scales spanning the range from kilometres to parsecs (a factor of more than 10^{13}), and with time scales spanning the range from milliseconds (e.g., in the mergers of compact objects) to the life time of the Universe (a factor of more than 10^{20}). As a result, traditional direct N-body integrators have developed special methods to accelerate the calculation without introducing approximations in the solution of Equations (1.12).

1.2.3 NBODY6 code

A state-of-the-art tool used for direct N-body simulations is the publicly available code NBODY6 (see Aarseth 1999, Aarseth 2003). In this case, the numerical integration is performed through a fourth-order Hermite integrator. The time-steps of integration are assigned to each particle individually according to the intensity of the force variation. In order to avoid prohibitively small time-steps, a special treatment for hard binaries and close hyperbolic encounters is introduced. This technique, known as KS-regularisation, is based on the classical Kustaanheimo-Stiefel formalism (Stiefel, 1965). Through a three-dimensional generalisation of

the Levi-Civita transformation, KS-regularisation allows to exactly follow the evolution of a tightly bound subsystem using a perturbative approach over the analytical two-body solution. A chain regularization strategy can be adopted for stable hierarchical multiples.

The NBODY6 code also involves packages for managing complex astrophysical processes. One example is represented by the inclusion of synthetic stellar evolution (see, e.g., Hurley et al. 2000). In order to increase the realism of numerical simulations of star clusters, a number of prescriptions are applied to deal with the mass loss that mostly characterizes the early stages of the evolution. Any mass loss is assumed to be instantaneous because the wind velocity is high compared with the escape velocity. Supernova events or black hole formation are also implemented by assigning a random natal kick to the dark remnant.

1.2.4 Hardware

A consistent part of my PhD project relies on the use of NBODY6 in the variant with GPU (graphics processing unit) support. GPUs allow to accelerate the N-body integration by carrying out individual force evaluations using multiple processors though a parallelised strategy. I could take advantage of two high performance computing (HPC) resources: Spartan at the University of Melbourne and OzSTAR at the Swinburne University. Both these HPC clusters grant multiple computational nodes, each typically containing $\gtrsim 12$ CPUs (central processing units) and $\lesssim 4$ GPUs. Under such conditions, the characteristic wall-time for a numerical simulation that follows 12 Gyr of evolution of a star cluster with 10^5 members is reduced to ≈ 15 days.

1.3 Intermediate-mass black holes

The search for intermediate-mass black holes (IMBHs) with masses between those of stellar-mass ($M_{BH} < 50 - 100 M_\odot$)[§] and super-massive ($M_{BH} > 10^6 M_\odot$) black holes has central relevance for several fields of astrophysics (see van der Marel 2003).

In the field of galaxy evolution, IMBHs have been indicated as the building blocks of the super-massive BHs ubiquitously found at the centre of galaxies (Larson, 2000; Madau & Rees, 2001; Volonteri et al., 2003; Volonteri & Rees, 2005; Volonteri, 2010). The exact formation mechanisms of super-massive BHs are poorly understood, with a major issue represented by the detection of quasars with masses of up to $10^{10} M_\odot$ at high redshift ($z \gtrsim 7$), when the Universe was only 800 Myr old (Bañados et al., 2018).

1.3.1 Strategies of detection

Despite recent efforts, unambiguous detections of individual IMBHs are still missing (Mezcua, 2017).

[§]Solar mass: $1 M_\odot = 1.989 \times 10^{30}$kg

One observational method relies on the detection of both X-ray and radio emission associated, respectively, to the accretion flow of gas on to the BH and to the synchrotron radiation from the emitted jets (see Strader et al. 2012). These observations, however, are complicated by the typical lack of gas in GCs (see e.g. Farrell et al. 2012, Mezcua et al. 2013, Haggard et al. 2013. One illustrative case is represented by the centre of the globular cluster G1 in M31 (Pooley & Rappaport, 2006), for which the observed X-ray source (Ulvestad et al., 2007) does not show a clear sign of radio activity (Miller-Jones et al., 2012).

As an alternative, the mass of an IMBH can be also constrained through the use of second-generation ground-based interferometers, which are able to detect the gravitational waves produced by possible mergers of massive compact objects into the IMBH. (see e.g. Mandel et al. 2008, Konstantinidis et al. 2013, MacLeod et al. 2016). However, this method has not provided with any IMBH candidate yet (Abadie et al., 2012).

Finally, the most secure approach to infer the presence of an IMBH is through the use of stellar dynamics. However, as the sphere of influence of an IMBH of $10^5 M_\odot$ is limited to ≈ 0.5pc, it can only be resolved within the Local Group (i.e. within ≈ 1Mpc).

1.3.2 IMBHs in globular clusters

Globular clusters have been traditionally indicated as promising candidates for hosting a central IMBH (see, e.g., Silk & Arons 1975, Bahcall & Wolf 1976a). Indeed, the very high density reached in the core provides with optimal conditions for the growth of an IMBH from direct collapse of compact seeds (see Portegies Zwart et al. 2004a).

Additionally, the search for IMBHs in globular clusters is motivated by an established relation (also known as $M_\bullet$-σ relation) between the bulge velocity dispersion and the mass of the central super-massive BH in galaxies (see Ferrarese & Merritt 2000, Gebhardt et al. 2000). Given the typical velocity dispersions measured in globular clusters, the evidence for the presence of IMBHs would imply that this relation continues to hold also in the regime of low-mass stellar systems (see Lützgendorf et al. 2013b).

The best observational evidence for a dark point-source mass comes from multi-epoch studies ($\sim$ 20 yr) of the proper motions of individual stars around the super-massive BH ($4 \times 10^6 M_\odot$) at the centre of the Milky Way (see Ghez et al. 2008). However such technique can hardly be applied to IMBHs. Indeed, considering that for Keplerian motions around a BH of mass M_{BH} the period of revolution for orbiting stars scales as $T \propto 1/M_{BH}^{1/2}$, under the same observational conditions of Ghez et al. (2008) (note that the distance to the Milky Way center is comparable to the typical distance to a globular cluster as reported in the Harris 2010 catalogue), it would be about 30 times larger ($\sim (M_{SMBH}/M_{IMBH})^{1/2}$) for an IMBH a thousand time less massive than the Milky Way's central SMBH.

A more suitable approach used to infer the presence of an IMBH is based on the collective motions of stars in the core. N-body simulations show that a central massive object causes a rise in the central velocity dispersion profile,

which can be used to constrain the IMBH mass through fitting with dynamical models. The traditional velocity measurements in the crowded central region of GCs rely on two different strategies: resolving the individual star velocities (line-of-sight velocities and proper motions) or using unresolved kinematic measurements (IFU spectroscopy). In a few instances, integrated-light spectroscopy has detected rising central velocity dispersions, leading to claims of IMBH detection (see Noyola et al. 2010, Lützgendorf et al. 2011). Conversely, for the same objects, resolved kinematic measurement were more consistent with a flat velocity dispersion profile and no massive BH (see van der Marel & Anderson 2010 and Lanzoni et al. 2013). Besides the observational difficulties, a possible limitation for this approach is represented by the adoption of dynamical models that have to rely on assumptions on both the degree of velocity isotropy and the mass-to-light ratio M/L. This represents a crucial and delicate step for the traditional modelling. In fact, it has been shown that models that include velocity anisotropy can describe state-of-the-art observations without the need for an IMBH (see Zocchi et al. 2017). Similarly, the presence of a concentrated population of dark remnants is able to increase the inner M/L profile and, thus, to produce effects on the kinematics of the luminous component similar to those of a central IMBH (see e.g. Arca-Sedda 2016, Peuten et al. 2016, Zocchi et al. 2018).

Finally, a complementary tool to search for IMBHs in globular clusters is that of finding novel dynamical signatures for their presence. Such signatures are generally identified though the study of numerical simulations. These investigations have shown that a central massive black hole is expected to induce the formation of a shallow cusp in the projected surface brightness and to prevent the core collapse by enhancing three-body interactions within its sphere of influence (see Baumgardt et al. 2004a, Baumgardt et al. 2004b, Trenti et al. 2007a). In addition, it has been shown that the IMBH is able to quench the process of mass segregation (see e.g. Gill et al. 2008, Pasquato et al. 2009). However, one important caveat is that these signatures may be only necessary but not sufficient conditions to infer the presence of an IMBH, because other dynamical processes could mimic them (see e.g. Hurley 2007, Trenti et al. 2010, Arca-Sedda 2016).

Therefore, identifying key dynamical indicators that can be adopted to characterise the BH population in star clusters has represented the main goal of our recent studies, and it will be discussed in details in the following Chapters of this thesis.

2

Detection of intermediate-mass black holes

The detection of intermediate mass black holes (IMBHs) in Galactic globular clusters (GCs) has so far been controversial. In order to characterize the effectiveness of integrated-light spectroscopy through integral field units, we analyze realistic mock data generated from state-of-the-art Monte Carlo simulations of GCs with a central IMBH, considering different setups and conditions varying IMBH mass, cluster distance, and accuracy in determination of the center. The mock observations are modeled with isotropic Jeans models to assess the success rate in identifying the IMBH presence, which we find to be primarily dependent on IMBH mass. However, even for a IMBH of considerable mass (3% of the total GC mass), the analysis does not yield conclusive results in 1 out of 5 cases, because of shot noise due to bright stars close to the IMBH line-of-sight. This stochastic variability in the modeling outcome grows with decreasing BH mass, with approximately 3 failures out of 4 for IMBHs with 0.1% of total GC mass. Finally, we find that our analysis is generally unable to exclude at 68% confidence an IMBH with mass of $10^3\ M_\odot$ in snapshots without a central BH. Interestingly, our results are not sensitive to GC distance within 5-20 kpc, nor to mis-identification of the GC center by less than $2''$ ($< 20\%$ of the core radius). These findings highlight the value of ground-based integral field spectroscopy for large GC surveys, where systematic failures can be accounted for, but stress the importance of discrete kinematic measurements that are less affected by stochasticity induced by bright stars.

2.1 Introduction

The existence of intermediate mass black holes (IMBHs) with masses between few $M_\odot$ (stellar black holes of $\approx 100\ M_\odot$) and billions of $M_\odot$ (supermassive black holes of $\approx 10^6\ M_\odot$) is of particular interest, especially in the context of the formation and evolution of galaxies and dense stellar systems such as globular clusters (GCs). The natural extension of the well-known $M - \sigma$ relation for galaxies suggests that the typical central velocity dispersions in GCs might be associated to the presence of IMBHs with masses of $10^{3-4}\ M_\odot$ (see, e.g., Ferrarese & Merritt 2000, Gebhardt et al. 2000). To support this extrapolation, several scenarios for the formation of such objects have been proposed, including run-away collapse of massive stars (Portegies Zwart et al., 2004a), early-time accretion of ejecta from asymptotic giant branch stars in the context of multiple stellar population formation (Vesperini et al., 2010), dynamical interactions of hard binaries (Miller & Hamilton, 2002; Giersz et al., 2015), or possibly seeding from massive Population III stars if the oldest globular clusters form during the epoch of reionization at redshift $z \sim 8 - 10$ (Trenti et al., 2015; Ricotti et al., 2016).

In recent years there have been many studies focused on searching for these objects. Some tentative detections have been claimed, but a non-controversial proof of their presence is still lacking (e.g., Haggard et al. 2013 and references therein). Some of the observational techniques used are based on the detection of the radio and X-ray emission associated with accretion processes, but these are complicated by the lack of gas in the old globular clusters in our Galaxy (see, e.g,

Farrell et al. 2012, Mezcua et al. 2013). Stellar dynamics, and in particular modeling of the central velocity dispersion profile is another tool for searching IMBHs, but measurements are very challenging because the sphere of influence of the BH is limited to a few arcsec, even for the closest and most massive GCs such as ω Cen (see Noyola et al. 2010; van der Marel & Anderson 2010). Finally, the fact that these events are expected to be also sources of gravitational radiation promotes the interferometers such as advanced-LIGO as further instruments to search for IMBHs (see, e.g., Mandel et al. 2008, Konstantinidis et al. 2013, MacLeod et al. 2016).

A complementary tool to approach the problem is that of identifying novel dynamical signatures for the presence of IMBH in globular clusters based on numerical modeling of globular cluster dynamics in presence of an IMBH. Starting from initial direct N-body simulations more than a decade ago (Baumgardt et al., 2004a,b; Trenti et al., 2007a), simulations have progressed significantly, and are now approaching realistic particle numbers with direct integration algorithms that include post-newtonian corrections (e.g. MacLeod et al. 2016; Wang et al. 2016), and routinely include more than one million particles through Monte Carlo methods (Giersz et al. 2015; see also Rodriguez et al. 2015). These investigations have shown that a central massive black hole is expected to induce the formation of a shallow cusp in the projected surface brightness and to prevent the core collapse by enhancing three-body interactions within its sphere of influence (see, e.g, Baumgardt et al. 2005). In addition, it has been shown that the IMBH is able to quench the process of mass segregation (see e.g., Gill et al. 2008, Pasquato et al. 2009, Pasquato et al. 2016). However, one important caveat is that these signatures may be only necessary but not sufficient conditions to infer the presence of an IMBH, because other dynamical processes could mimic them (see, e.g., Hurley 2007; Trenti et al. 2010; Vesperini & Trenti 2010).

Recently, the majority of the observational claims about the presence of IMBHs comes from kinematic measurements in the inner core of Galactic GCs. Kinematic observations suggesting the presence of IMBHs are traditionally based on the search for a rise of the central velocity dispersion. This method requires both high spatial resolution, to resolve the very crowded central region of GCs (few central arcseconds), and very precise velocity measurements with accuracy ≈ 1 km s^{-1}.

So far, the available observations of the central regions of Galactic GCs have led to contradictory results when applied to the same object in a few instances (e.g., Noyola et al. 2010, van der Marel & Anderson 2010, Lützgendorf et al. 2013a, Lanzoni et al. 2013, Lützgendorf et al. 2015). In general, two different strategies are used in order to infer the presence of IMBHs: resolving individual star velocities (line-of-sight velocities or proper motions) or using unresolved kinematic measurements, for example with integral field unit (IFU) spectroscopy. Both these methods suffer technical difficulties in obtaining the critically needed kinematic measurements in the very center of the system (e.g., the problem of shot-noise for integrated-light measurements and the effects of crowding for line-of-sight velocities and proper motions). In particular, integrated-light spectroscopy tends to detect rising central velocity dispersions, suggesting the presence of IMBHs

(see for example, Noyola et al. 2010 for ω Cen, or Lützgendorf et al. 2011 for NGC 6388), while resolved stellar kinematics are consistent with a flat velocity dispersion profile, that is no massive black hole (see van der Marel & Anderson 2010 for proper motion measurements of ω Cen, and Lanzoni et al. 2013 for discrete line-of-sight measurements in NGC 6388). However, in a few other cases where both discrete and integrated-light profiles are available for the inner $10''$, the observational methods agree (e.g., see NGC 2808, NGC 6266, NGC 1851 in Lützgendorf et al. 2013a).

For both unresolved and resolved kinematics, the constraints on the IMBH mass are generally determined by fitting the observed velocity dispersion profiles with different families of Jeans models (e.g, van der Marel & Anderson 2010). These models are typically constructed by making assumptions on the mass-to-light ratio profile $M/L(r)$ in order to calculate the intrinsic mass distribution of the luminous component from the surface brightness profile. The velocity dispersion profile is then calculated by solving the Jeans equation for hydrostatic equilibrium in a spherical stellar system (see e.g., Bertin 2014). Besides the Jeans modeling, other analysis techniques used include the Schwarzschild's orbit superposition method used in van de Ven et al. 2006 or a method in which the fit of the observed velocity dispersion profiles is performed using a grid of N-body simulations (see e.g., Jalali et al. 2012; Baumgardt 2017).

The main goal of this work is to characterize under which conditions (IMBH mass, GC distance, accuracy in the determination of the center) the integrated-light IFU data are able to measure accurately the mass of the IMBH, as inferred from realistic mock observations of simulated star clusters with a central IMBH. By means of the software SISCO developed by Bianchini et al. 2015, we are able to create mock IFU observations of the central regions of GCs. The set of observations is produced starting from a set of Monte Carlo cluster simulations (MOCCA simulations by Giersz et al. 2015; Askar et al. 2017b; see also Askar et al. 2017a, for a similar application of SISCO to MOCCA simulations) that include a range of different IMBH masses (from 0 to 10^4 $M_\odot$). In order to quantify the significance of a central rise in the simulated velocity dispersion profiles, we fit these profiles with a one-parameter family of isotropic Jeans models. In this way, we are able to estimate quantitatively and objectively the IMBH mass and, thus, to directly test the ability of the observations to successfully recover the mass of the central black hole.

The paper is organised as follows. In Sect.2.2 we present the set of simulations used and we briefly describe the SISCO code used to produce the mock IFU observations. Moreover, we describe the dynamical models used to fit the observed profiles. In Sect.2.3 we present the results of our analysis and in Sect.2.4 we give our conclusions.

Table 2.1: Set of MOCCA simulations, labeled S0-S5, used in this paper and taken from MOCCA-SURVEY Database I Askar et al. (2017b). For each simulation we report the quantities relative to the snapshot at 12 Gyr: number of stars N; total mass M and IMBH mass $m_\bullet$ (solar units); binary fraction f_b; projected truncation radius R_t, projected core radius R_c (from the surface brightness profile), projected half-light radius R_h and intrinsic radius for the IMBH sphere of influence $r_\bullet$ (pc); concentration parameter $C = \log(R_t/R_c)$.

	S0	S1	S2	S3	S4	S5
N	1.1×10^6	1.0×10^6	1.0×10^6	2.9×10^5	5.6×10^5	6.3×10^5
M	3.0×10^5	3.0×10^5	3.4×10^5	9.6×10^4	1.8×10^5	2.0×10^5
$m_\bullet$	1.0×10^4	9.9×10^3	5.6×10^3	1.6×10^3	2.3×10^2	-
f_b	7%	8%	4%	5%	5%	3.6%
R_t	102.6	80.9	89.6	59.8	69.1	89.1
R_c	0.3	0.4	0.2	0.4	0.6	1.3
R_h	1.9	2.1	2.6	2.2	2.0	2.3
$r_\bullet$	0.452	0.559	0.198	0.260	0.012	-
C	2.53	2.30	2.64	2.17	2.06	1.8

2.2 Methods

2.2.1 MOCCA simulations

In this work we resort to Monte Carlo simulations of GCs that include the presence of a central IMBH. These simulations are part of about 2000 GC models run in the framework of the MOCCA SURVEY I project (see Askar et al. 2017b for a description of the Survey). The IMBH in the simulated clusters is formed dynamically from stellar-mass BH seeds as a result of dynamical interactions and mergers in binaries.

All models have a stellar initial mass function (IMF) given by Kroupa (2001) with minimum and maximum stellar masses taken to be $0.08\ M_\odot$ and $100\ M_\odot$, respectively. Supernovae (SN) natal kick velocities for neutron stars and BHs were drawn from a Maxwellian distribution with a dispersion of 265 km/s (Hobbs et al., 2005). For most models, natal kicks for BHs were modified according to the mass fallback procedure described by Belczynski et al. (2002). To model the Galactic potential, a point mass approximation with the Galaxy mass equal to the mass enclosed inside the cluster Galactocentric distance is assumed. Additionally, it is also assumed that all clusters have the same rotation velocity, equal to 220 km/s. So, depending on the cluster mass and tidal radius the Galactocentric distances span from about 1 kpc to about 50 kpc.

Here, we selected a subsample of MOCCA runs for analysis, and report in Table 2.1 the key properties at time $t = 12$ Gyr. In addition to this snapshot, we also consider three additional snapshots at 11.7, 11.8, 11.9 Gyr to assess the robustness of our conclusions against variance introduced by a different dynamical state of a system of otherwise similar global properties.

2.2.2 SISCO software

The software SISCO (Simulating Stellar Cluster Observation) produces a mock IFU data cube starting from a simulated star cluster (for a detailed description see Bianchini et al. 2015). The software derives a medium-high resolution spectrum ($R \approx 20000$) in the wavelength range of the Ca triplet (8400-8800 Å) for every star of the simulation, based on mass, effective temperature, luminosity and metallicity. The spectral coverage and resolution are tailored to mock observations of typical IFU instruments like FLAMES@VLT in ARGUS mode (Pasquini et al., 2012). SISCO allows users to define specific instrumental setups: we fix the size of the field-of-view (FOV) to 20×20 arcsec^2 and the spaxel scale to 0.25 arcsec; we adopt a Moffat shape for the point spread function with seeing condition of 1 arcsec and shape parameter $\beta = 2.5$. Finally, we mimic an observation with an average signal-to-noise ratio of $S/N \simeq 10$ per Å (for a discussion on the fixed values of the parameters used in our mock observations, see Bianchini et al. 2015). In order to simulate different observing conditions, we change three parameters: the distance to the cluster, the direction of its projection in the sky, and optionally introduce an off-set between the centre of the simulated IFU field and the centre of the cluster, to reflect the uncertainty in determining the centre of an observed GC. The final output of the code is a three-dimensional data cube in which each spatial pixel has an assigned spectrum.

2.2.3 Determination of the velocity dispersion profile

In order to mimic real observation as closely as possible, we construct the observed velocity dispersion profile by integrating our mock IFU data available for the region inside the FOV, and combine it with a line-of-sight velocity dispersion obtained for the outer parts of the system. The outer profile is obtained directly from the simulation by using only the velocities of the red giant stars, which are those generally used for resolved kinematics from the ground. For this analysis, we treat the binary stars as single objects with the velocity of their center of mass. For the inner profile, once the IFU data cube is simulated through SISCO, we divide the FOV in radial bins, summing the spectra in each bin, with the aim of interpreting the data cube through a spherical dynamical model. The binned spectra are analysed with the pPXF code (Cappellari & Emsellem 2004) to derive the velocity dispersion (and the corresponding error) from line broadening.

As highlighted in Bianchini et al. (2015), when integrated-light measurements are used, the presence of a few bright stars can introduce systematic effects in the reconstruction of the observed velocity dispersion profile. For this reason, we introduced masking of the brightest sources. Specifically, we exclude from the analysis the spaxels in which the contribution of a single stars exceeds the 60% of the total luminosity (we adopt the same percentage used in Lützgendorf et al. 2013a). This information is provided directly by the simulation, thus, from an observational point of view, we are considering an ideal case scenario. In Fig. 2.1 we show the luminosity map (left panel) and the radial velocity dispersion profile (right panel) for the central region of simulation S0 at a distance of 10 kpc. The velocity dispersion profile constructed from the simulation (blue circles) is

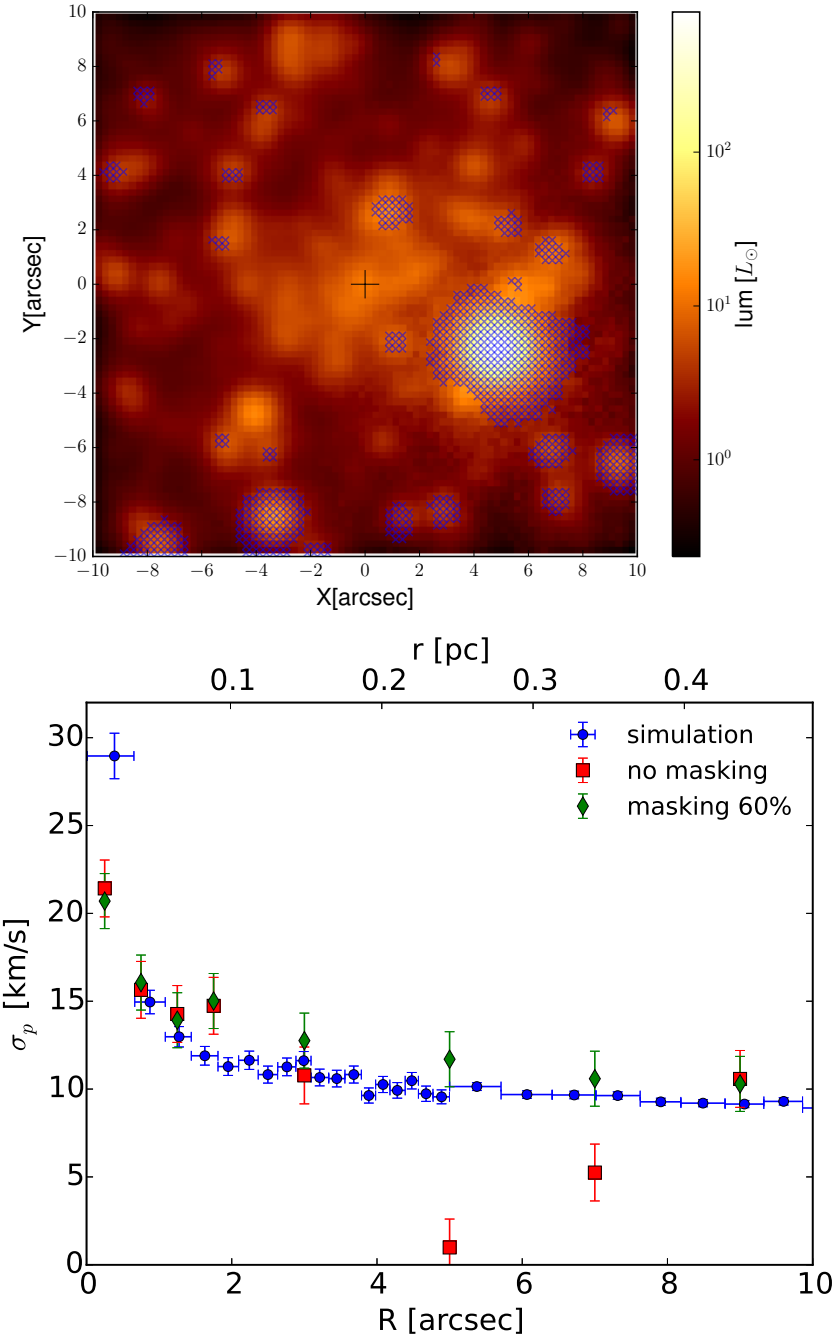

Figure 2.1: *Top panel:* luminosity map of the simulated cluster S0 observed at a distance of 10 kpc with a FOV around the centre of the cluster. The masked spaxels are indicated with the 'x' symbols. *Bottom panel:* Central velocity dispersion profiles for the same cluster. The blue circles show the profile measured directly from the MOCCA simulation considering objects with masses between 0.7 $M_\odot$ and 1 $M_\odot$ and using the barycentre velocity for binary systems. The profile inferred from analysis of the mock IFU data cube is plotted in red squares without masking, and in green diamonds with the bright-object masking procedure discussed in the text.

obtained by considering objects with mass in the range $0.7 - 1\ M_{\odot}$ to mimic the average (luminosity weighted) mass in the FOV and by using the barycentre line of sight velocities for the binary stars to avoid great scatter in the profile (the binning must be fine in order to sample the central region). The velocity dispersion profile obtained by masking the IFU data over the regions shown as green diamonds is consistent with that constructed directly from the simulation. Without the masking, there is an evident discrepancy in the range $4-8$ arcsec between the observed profile and the expected one. The presence of a very bright star in this radial bin thus influences the observed velocity dispersion with the tendency of underestimating the measurement.

Despite the masking of the brightest sources, the observed profiles tends to slightly overestimate the velocity dispersion for radii $> 2''$. This effect is possibly due to the presence of hard binaries which may influence the velocity dispersion determination. Indeed, the observed velocity associated to a binary system could largely exceed the mean field velocity because of the high-speed orbital motions. This effect is merely an observational feature associated to line-of-sight velocity dispersion measurements, and in principle it could be accounted for if proper-motion kinematic is available (see e.g., Bianchini et al. 2016a), or through theoretical modeling of the binary population, both in energy and position space. However, this investigation is beyond the scope of the present paper and we limit our analysis to include the effects of the population of binaries into the construction of our mock observations.

Finally, we produced different realisations of the same simulation to test the intrinsic scatter of the velocity dispersion profile. In particular, we changed the direction of the line-of-sight for the mock observation of the cluster S0 under canonical conditions (that is, at 10 kpc and with the FOV pointing to the centre). For three different projections of the simulated cluster we obtained a velocity dispersion profile for which the scatter is uniform along the entire profile and it does not exceed the 30% of the central value (see Fig. 2.2). Especially for the outer points, where the signal is stronger, the intrinsic scatter is much larger than the errors calculated by the pPXF software from line broadening. For this reason, for the rest of our analysis, we will consider an error $\delta\sigma$ for all the points in the observed profile calculated by considering the error $\delta\sigma_0$ obtained by pPXF for the innermost point. In particular, the error for any outer point is given by $\delta\sigma = \delta\sigma_0(\sigma/\sigma_0)$, where σ_0 and σ are the velocity dispersions of the innermost point and the outer point, respectively.

2.2.4 Dynamical modeling

As usually done in the literature, we fit the velocity dispersion profile derived from the mock observations with a family of dynamical models in which the IMBH mass is treated as a free parameter. We place ourself under the ideal conditions of assuming a perfect knowledge of the spherically symmetric distribution of the stellar particles. Thus, we adopt a spherical and isotropic Jeans model in which the total gravitational potential of the system, $\Phi(r)$, is given by the sum of the stellar/remnant contribution $\Phi_*(r)$ and the IMBH contribution

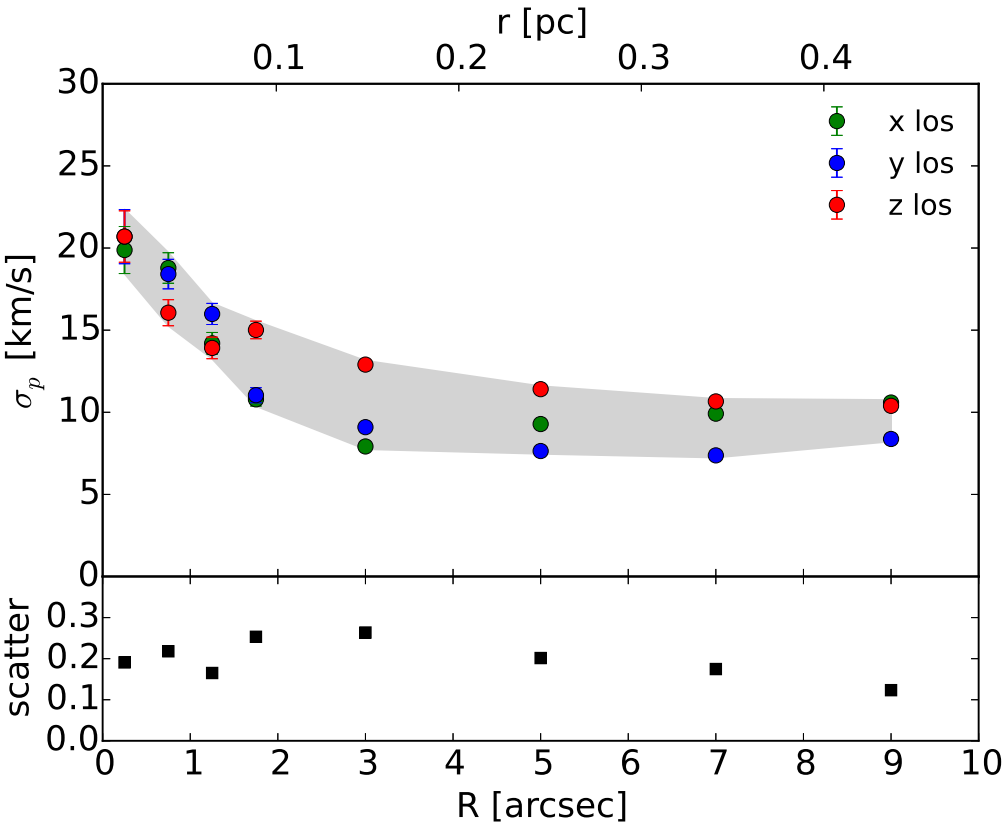

Figure 2.2: Observed velocity dispersion profiles of the cluster S0 at a distance of 10kpc for three different directions of the line-of-sight. The bottom panel shows the scatter in the velocity dispersion, that is, the difference of the greater and the lower value for each radial position divided by an average central value for the velocity dispersion.

$\Phi_\bullet(r) = -m_\bullet/r$ (we fixed the gravitational constant G=1). The mass distribution of stars and remnants is directly inferred from the simulation. * The density ρ at each radius r is estimated using spherical cells, by dividing the total mass (including the IMBH in the innermost cell) of the particles by the shell volume. The radial profile $(d\Phi_*/dr)(r)$ follows from the Gauss theorem as

$$\frac{d\Phi_*}{dr}(r) = \frac{M(<r)}{r^2}, \tag{2.1}$$

where $M(<r)$ is the stellar and remnants mass (excluding the central IMBH) contained in the sphere of radius r.

We then calculate the intrinsic velocity dispersion profile $\sigma(r)$ from the spherical isotropic Jeans equation

$$\frac{1}{\rho}\frac{d}{dr}\left(\rho\sigma^2\right) = -\frac{d\Phi}{dr}, \tag{2.2}$$

which has the solution

$$\sigma^2(r) = \frac{1}{\rho(r)}\int_r^\infty \rho(r')\frac{d\Phi}{dr}(r')\,dr'. \tag{2.3}$$

By defining the first derivative of the gravitational potential as

$$\frac{d\Phi}{dr}(r) = \frac{m_\bullet}{r^2} + \eta^2\frac{d\Phi_*}{dr}(r), \tag{2.4}$$

where η is a constant, the total velocity dispersion in Eq. (2.3) can be explicitly written as the sum of the IMBH contribution and the stellar/remnant contribution. In this way, for a given mass density profile, the velocity dispersion profile depends only on the mass $m_\bullet$ of the central IMBH and on η, which are free parameters of the model. Note that the second parameter $\eta \sim 1$ (a global multiplicative rescaling of the velocity dispersion) has been added in order to take into account two aspects of the kinematics. The first and most relevant is related to possible observational biases due to the presence of binary stars. The effect of considering individual motions in binary systems should be that of increasing the observed velocity dispersion, as orbital speeds may arbitrarily differ from the average field velocity. The second aspect is related to the presence of (partial) energy equipartition. In fact, the velocity dispersion of a population of kinematic tracers will in general depend on their characteristic mass compared to the average particle mass in the system, as well as from the dynamical state of the system, with realistic mass spectra achieving only a partial equipartition (Baumgardt & Makino, 2003; Trenti & van der Marel, 2013; Bianchini et al., 2016b). For these considerations we find convenient to limit η to the plausible range $[0.5, 2.0]$.

Finally, for a proper comparison with the observation we consider the projected velocity dispersion profile $\sigma_p(R)$ obtained by integrating the density-weighted

*Note that this approach is different from what usually done in real observations, for which the inferred mass distribution can be affected by observational biases or specific assumptions on the mass-to-light ratio profile.

intrinsic profile along the line-of-sight direction:

$$\sigma_p(R) = \left[\frac{\int_R^\infty r(r^2 - R^2)^{-1/2} \rho(r) \sigma^2(r)\, dr}{\int_R^\infty r(r^2 - R^2)^{-1/2} \rho(r)\, dr} \right]^{1/2} . \tag{2.5}$$

In Fig. 2.3 we show the dynamical modeling predictions for the velocity dispersion profiles obtained by changing the mass of the central IMBH for the simulation S0 (we fixed $\eta = 1$). As reference, we plot also the velocity dispersion profile constructed directly from the simulation for object in the mass range $[0.7 - 1.0 M_\odot]$, that is the range that includes the average mass observed in our FOV. It is noteworthy that there is good agreement between the inner profile and the Jeans model profile with an IMBH of $10^4\ M_\odot$, which is the actual value for this simulation.

To quantify the recovery of the IMBH mass we carry out a maximum likelihood fit by minimizing the two-dimensional chi-square function

$$\chi^2(m_\bullet, \eta) = \sum_{i=1}^{N} \left[\frac{\sigma_{obs}(R_i) - \sigma_p(R_i; m_\bullet, \eta)}{\delta\sigma(R_i)} \right]^2 , \tag{2.6}$$

where $\sigma_{obs}(R_i)$ are the observed velocity dispersion values (with the error $\delta\sigma(R_i)$) for the N radial bins in which the FOV has been divided (see the previous subsection for a proper description of the error $\delta\sigma(R_i)$).

2.3 Results

2.3.1 Canonical model

In this section we consider the cluster S0 at 12Gyr. This cluster is characterized by a central IMBH of $1.0 \times 10^4\ M_\odot$ which represents $\sim 3\%$ of the total mass (and it thus serves as a clear case to test detection in our study under the favourable conditions of a massive central IMBH).

At a distance of 10 kpc, a total of 38400 stars fall in the field of view (see the luminosity map in Fig. 2.1). The observed velocity dispersion profile is constructed by masking the IFU data following the procedure described in Sec. 2.2.3. Then, the chi-square function in Eq. (2.6) is minimised in the two dimensional parameter space, giving a best fit value for the IMBH mass of $6.0^{+0.6}_{-1.0} \times 10^3\ M_\odot$ and a value for η of $1.19^{+0.04}_{-0.04}$ (the errors are estimated with 68.3% confidence). In the left panel of Fig. 2.4 we plot the best fit Jeans model in comparison with the observed velocity dispersion profile. We also identify the regions corresponding to confidence levels of 68.3%, 95.4% and 99% (see Fig. 2.4, right panel) finding that the true IMBH mass is higher by a factor ≈ 1.25 with 3σ confidence.

2.3.2 Dependence on the IMBH mass

As described in Sec. 2.2.1, our set of simulations includes systems with a range of IMBH masses but otherwise similar properties. By applying the same analysis presented in Sec. 2.3.1 to the different models listed in Table 2.1, we aim to study

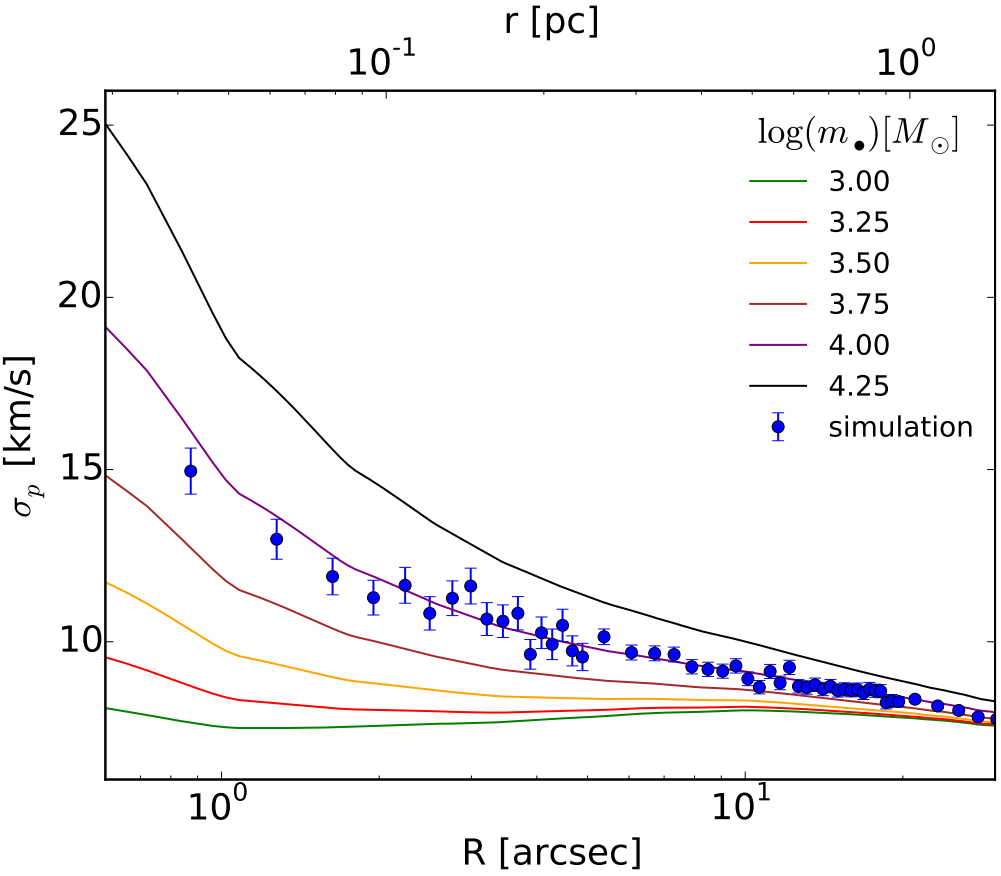

Figure 2.3: Projected velocity dispersion profiles in the centre of the cluster in simulation S0 considered at a distance of 10 kpc. The solid lines represent six velocity dispersion profiles derived from different Jeans model obtained by varying the IMBH mass from 10^3 to $10^{4.25}$ $M_\odot$ with a logarithmic separation of 0.25. By increasing the mass, the central peak becomes steeper. The circles represent the velocity dispersion profile derived directly from the simulation considering objects with masses between 0.7 and $1 M_\odot$.

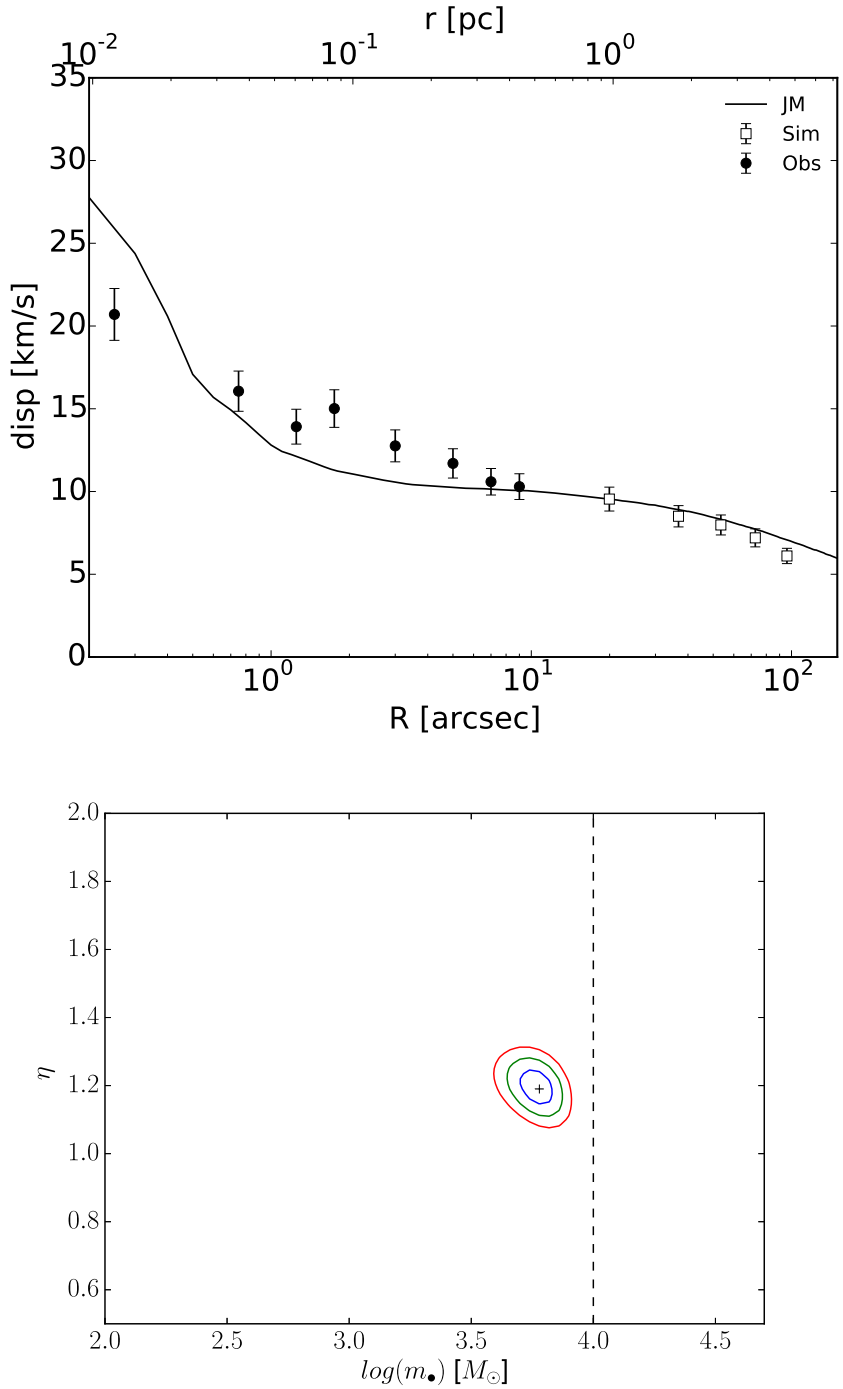

Figure 2.4: *Top panel:* Best fit Jeans model for the cluster in simulation S0 at 12 Gyr. The observed inner profile (solid circles) is obtained at a distance of 10 kpc pointing the FOV to the right centre of the cluster. The outer profile (open squares) is obtained directly from the simulation by considering only the velocities of the red giants. *Bottom panel:* 2D map of the chi-square function in the two parameters η and $m_\bullet$. The three regions correspond to confidence levels of 68.3%, 95.4% and 99%. The dotted line indicates the true mass of the IMBH. The Jeans model is not able to recover the mass of the IMBH (10^4 $M_\odot$) in the 3-sigma confidence.

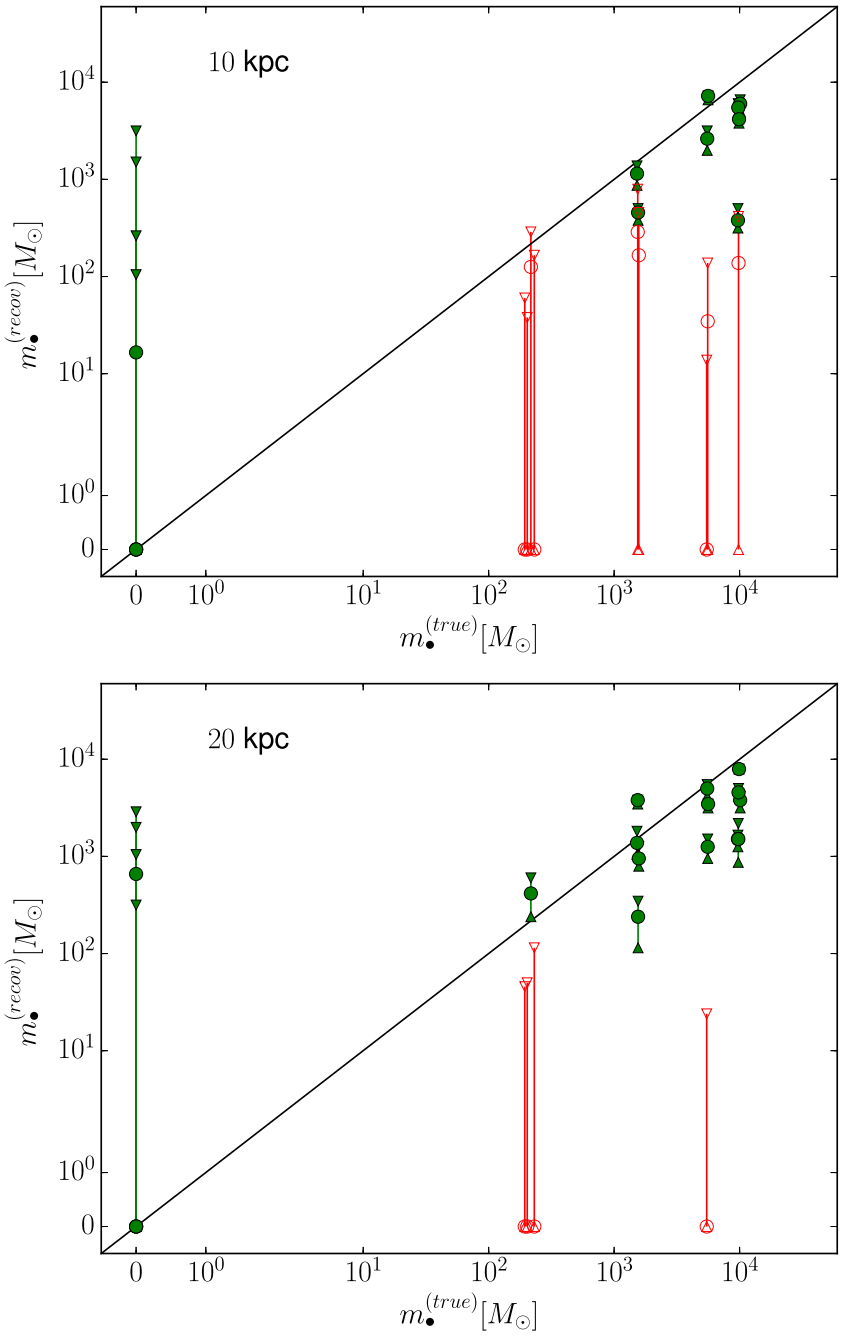

Figure 2.5: Comparison between the true mass of the IMBH from the simulations and the mass recovered for the best fit of the mock observation. All the clusters are considered at a fixed distance of 10 kpc (*top panel*) and 20 kpc (*bottom panel*) by identifying the right centre for the FOV. The black line represents the relation $m_\bullet^{(true)} = m_\bullet^{(recov)}$. Every circle is the best fit mass $m_\bullet$ of the IMBH, while the error bars correspond to the confidence interval of 68.3%. As solid green circles we show the successful cases in which the observations are able to determine a lower limit greater than zero for the IMBH mass, while as open red circles we represent the cases in which the best fit mass is consistent with zero. For the simulation without the IMBH we plot in green those cases in which the best fit mass is consistent with zero within 1-sigma confidence.

the fidelity of the IMBH mass measurement as a function of mass itself. Qualitatively, we expect that, at fixed observational setup, the chances of recovering the IMBH mass correctly increase with mass (since the sphere of influence and the IMBH contribution to the central velocity dispersion profile are both larger).

In Fig. 2.5 we show the IMBH mass recovered from the best fitting Jeans models as a function of the intrinsic IMBH mass. We present the results for each of the 4 snapshots (at 11.7, 11.8, 11.9 and 12 Gyr) of the simulations S1-S5 considered at a distance of 10 and 20 kpc (for the simulation S0 we considered only the snapshot at 12 Gyr). The results are color-coded according to the ability of the models to infer the presence of an IMBH with 1-sigma confidence. The red open circles represent the cases in which a solution without an IMBH is allowed at 1-sigma (or, for the simulation S5, in which a solution with $m_\bullet > 0$ is found at 1-sigma), and are flagged as failures. The green circles represent the cases identified as proper detections. This means that the best fit model is able to find a lower limit greater than 0 to the IMBH mass (or, in the case of the simulation S5 without the IMBH, a lower limit equal to 0). Note that these observations include cases in which the IMBH mass is greater than 0, but not consistent with the real mass of the simulation. These subcases are the majority in our sample as the mass inferred from the mock observations is found to generally underestimate the true mass. This might possibly happen because of systematic introduced by binary stars. The increment in the velocity dispersion due to the presence of binaries may exhibit radial variations which are not captured by our simple radial-independent correction factor η. Thus, our analysis may tend to overestimate the contribution of stars (and, subsequently, underestimate the contribution of the IMBH) to the central velocity dispersion. By taking into consideration this effect in a more refined modeling we would expect the green circles below the reference line to uniformly shift upwards and, eventually, intercept the true mass. However a more sophisticated treatment of the impact of binaries would rely on knowledge that is generally not available, nor used, in Jean-model analysis of actual observations, rather than mock data. Therefore, it would not be appropriate to implement such modeling to our mock IFU dataset.

The expected trend with the IMBH mass is partially recovered (see Fig. 2.5). Indeed, from an IMBH of few hundred $M_\odot$ to a high mass IMBH of 10^4 $M_\odot$ the successful probability increases from the 0% to the 80% of the cases considered at 10kpc. Also, we notice that, even for the high range of IMBH mass, some observations fail. This confirms how the stochasticity, which affects integrated-light measurements, arises even for a single cluster observed at different dynamical times. Finally, for the simulation S5 without the IMBH, all the cases at both distances are consistent with a cluster with no IMBH, even though the model is in general unable to exclude at 68% confidence a IMBH with mass of $10^3 M_\odot$.

Besides the dependence on the IMBH mass, we are interested in studying how two other parameters can affect the probability of recovering the IMBH mass. In particular, we want to quantify the importance of identifying the right centre for the observation and to explore the dependence on the distance to the cluster.

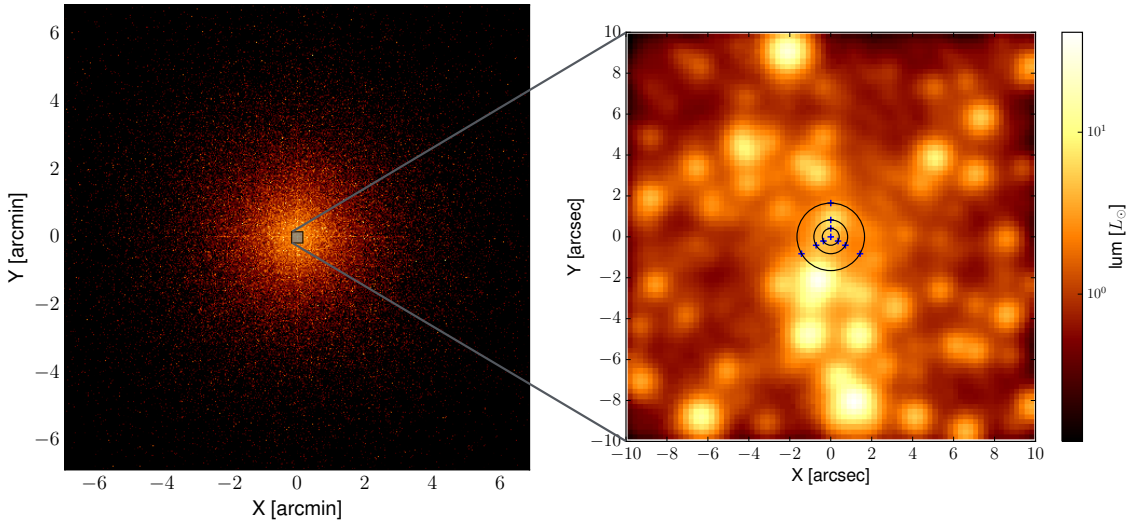

Figure 2.6: *Left panel*: Luminosity map of the cluster S1 at a distance of 10 kpc. *Right panel*: detail of the $20'' \times 20''$ FOV. The blue crosses represent the 9 different centres of the analysis we investigate, distributed at three different radial positions with a 5%, 10% and 20% off-sets with respect to the projected core radius from the intrinsic density centre of the simulation.

2.3.3 The identification of the centre

The identification of the centre in which to carry out the analysis is fundamental within the typical observational assumption of modeling in spherical geometry. In practical cases, there are two main sources of uncertainty associated with the centre. First, it is often challenging to determine the position of the cluster centre to high accuracy, as illustrated, for example, by the extensive debate on where the centre of ω Cen is (see, e.g, Noyola et al. 2010; van der Marel & Anderson 2010). In addition, even when the centre of light (or the kinematic centre) of the system is identified with high-accuracy, there is no guarantee that the BH location coincides with it, especially in the case of a light IMBH (see e.g., Giersz et al. 2015, Haster et al. 2016).

For two snapshots (at 11.7 and 12 Gyr) of the simulations S1 (high mass IMBH) and S3 (low mass IMBH), we analyse FOVs placed at different radial offsets of the centre (the distance to the clusters is fixed at 10 kpc). We consider a total of 9 different centres, three for each radial positions $0.4125''$, $0.825''$ and $1.65''$ corresponding for both clusters to radial offsets of 5%, 10% and 20% of the core radius (see Fig. 2.6). In terms of the sphere of influence of the central IMBH (whose radius $r_\bullet$ is defined as the radius at which the cumulative mass equals the IMBH mass), the offsets are in the range $0.03 - 0.14 r_\bullet$ for the simulation S1 and in the range $0.08 - 0.3 r_\bullet$ for the simulation S3.

With the same notation used in the previous subsection we show the results of the analysis in Fig. 2.7. For both the clusters we analyse two different snapshots at 11.7 and 12 Gyr. In both cases the probability of detecting an IMBH slightly decreases by increasing the off-set. However, this trend is deeply influenced by the stochasticity as for a fixed radial off-set the success of the observation changes

according to the angular position of the centre (e.g., see the high IMBH mass case with a fixed off-set of $1.6''$).

We wish to emphasise the fact that for our observations we are using all the information available from the simulation to produce the Jeans models used in the fitting procedure. The same modeling procedure is unavailable for real observations and, thus, we expect a wrong identification of the centre to reduce the successful probability found in our work (for a comparison with real observations, see the discrepancy of $\simeq 8\%\ R_c$ for the centre of Omega Cen in Noyola et al. 2008 and van der Marel & Anderson 2010).

2.3.4 Changing the distance

Among the parameter that we change in our mock observations there is the distance to the cluster. The central IMBH is characterized by a sphere of influence that, in first approximation, depends only on its mass. Therefore, for one particular simulation and for a fixed resolution of the instrument, increasing the distance to the cluster has the same effect of reducing the sphere of influence of the black hole. As consequence, the central peak in the velocity dispersion is expected to reduce with increasing distance. As opposite effect, a more crowded FOV obtained by considering higher distances should limit discreteness effects such as the shot noise introduced by bright stars.

We consider 3 different selected distances: 5, 10 and 20 kpc. In Fig. 2.8, we plot the recovered mass as a function of the distance to the cluster for each of the 4 snapshots available for the simulations S1 and S3. The probability of recovering an IMBH is marginally influenced by the distance to the cluster with the higher number of successes found at 20 kpc, where the influence of shot noise on the velocity dispersion profile is reduced.

2.4 Conclusions

We simulated different integrated-light IFU observations for a sample of MOCCA simulations characterized by a series of realistic ingredients (high number of stars, stellar evolution, primordial binaries) and by different IMBH mass. Our goal was to test under which conditions the IMBH is recovered from the fit of a family of Jeans models to the mock observed velocity dispersion profile. We started by considering the different simulated clusters in canonical observational conditions, that is at a typical distance of 10 kpc and by identifying the right centre of the field of view. Even though we adopted an optimal masking procedure to limit the effect of the most bright stars, we find that our results are significantly influenced by the intrinsic stochasticity of the IFU measurements. Indeed, for every class of IMBH considered we found at least one snapshot in four for which the observed IMBH mass is consistent with the case without black hole. Decreasing the IMBH mass leads to a larger probability of failing to infer the BH presence from Jeans modeling, with probability of obtaining a null result going up to $\sim$75% for IMBH mass 0.1% of the total cluster mass. In addition, even when the IMBH presence is successfully recovered from the modeling, the inferred mass is sys-

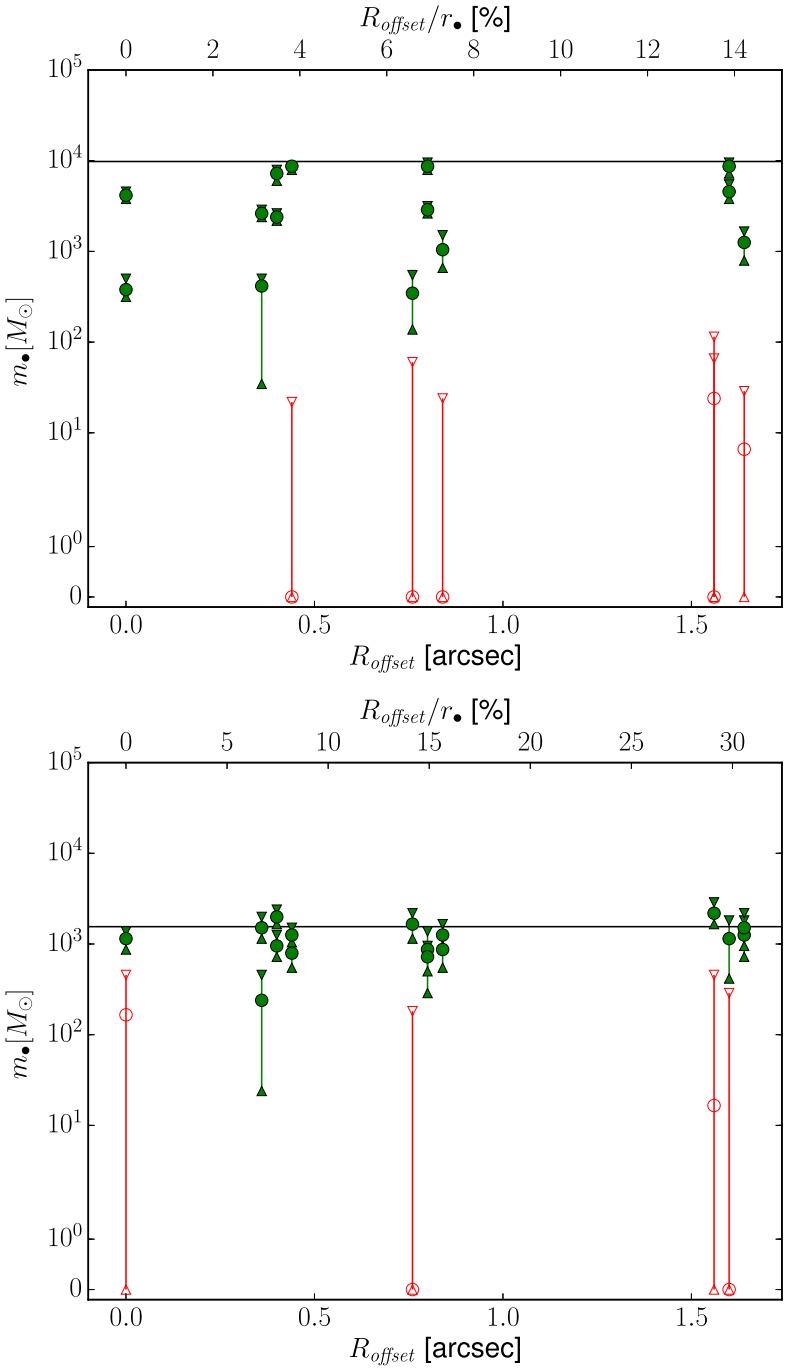

Figure 2.7: Recovered IMBH mass for the 11.7 and 12 Gyr snapshots of the cluster S1 (*top panel*, high BH mass) and the cluster S3 (*bottom panel*, low BH mass) considered at a distance of 10 kpc (for a detailed descriptions of the symbols used see Fig. 2.5). For every (positive) radial off-set there are 6 estimates of the mass, two (from different snapshots) for each of the three points equidistant from the centre (see Fig. 2.6), which are shown with a slight shift along the x-axis in the figure for improving clarity. The probability of detecting an IMBH slightly decreases by increasing the off-sets.

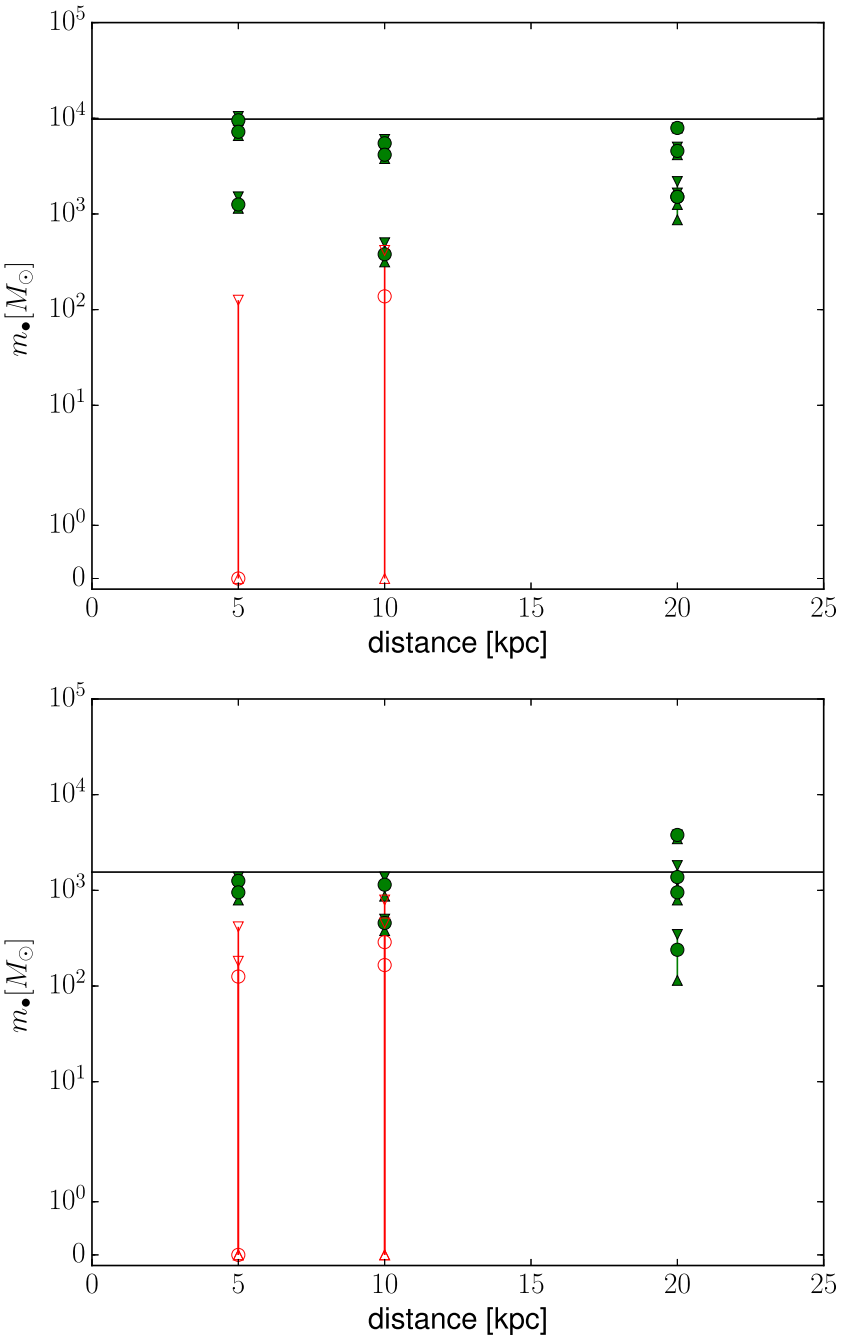

Figure 2.8: Recovered IMBH mass as function of the distance to the sun for the cluster S1 (*top panel*, high BH mass) and S3 (*bottom panel*, low BH mass) at 11.7, 11.8, 11.9 and 12Gyr. The symbol used are the same of Fig. 2.5.

tematically under-estimated, possibly because of the hard-to-quantify impact of binary stars (see Fig. 2.5). Finally, in the large majority of snapshots without an IMBH, the Jeans modeling was not able to set reasonably low constraints to the inferred IMBH mass, that is even if the best fit mass was consistent with 0, it was impossible to exclude the presence of a massive IMBH at 68% confidence.

In the second part of the paper we focused on changing crucial parameters of the observational setup. In particular, we explored the effects that the distance to the cluster and the centre of the field of view have to the inferred IMBH mass. The dependences on these two observational features have been analysed for two different regimes: high IMBH mass and low IMBH mass. In both cases we found similar trends.

For a misidentification of the cluster centre not greater than the 5-20% of the core radius we find that the presence of a central IMBH is successfully recovered in most observations. For both simulations, the highest number of failed observations corresponds to an off-set of $20\%\ R_c$ (corresponding to $\sim 1.6''$ at 10 kpc), suggesting a slight dependence of the successful probability with the centre off-set. We expect that this trend dramatically increases in real observations, for which the Jeans modeling is based on some assumptions on the light distribution.

Finally, the recovered IMBH mass is not particularly influenced by changing the distance between 5 and 20 kpc, even if the number of successes is higher at 20 kpc. According to the Harris catalogue (Harris 1996, 2010 edition) the 71% of all the Galactic GCs are found in this range of distances.

Overall, our findings demonstrate that ground-based IFU observations of the cores of GCs can be very helpful tools to investigate whether IMBHs are present in galactic GCs, especially because it does not appear that increased distance induces a higher failure rate in the recovery of input IMBHs. However, a large sample of objects would be required in order to draw meaningful conclusions on the average IMBH occupation fraction in GCs. In fact, the failure rate of any single observation is high (25-100% depending on BH mass) due to stochastic superposition of bright stars along the line of sight to the IMBH, and this bias needs to be corrected for. In conclusion, this work shows how any future IFU observation needs to be supported by other techniques with the purpose of providing complementary approaches. Even with their own observational limitations, either proper-motion based kinematics, such as that available from Hubble Space Telescope imaging at multiple epochs (Anderson & van der Marel, 2010; Bellini et al., 2014), or discrete kinematics from resolved-star spectroscopy (Lanzoni et al., 2013; Kamann et al., 2016) may be used to constrain (especially in the outer regions) any tentative detection from integrated-light IFU observations .

3

IMBH dynamics in dense stellar clusters

Despite recent observational efforts, unequivocal signs for the presence of intermediate-mass black holes (IMBHs) in globular clusters (GCs) have not been found yet. Especially when the presence of IMBHs is constrained through dynamical modeling of stellar kinematics, it is fundamental to account for the displacement that the IMBH might have with respect to the GC centre. In this paper we analyse the IMBH wandering around the stellar density centre using a set of realistic direct N-body simulations of star cluster evolution. Guided by the simulation results, we develop a basic yet accurate model that can be used to estimate the average IMBH radial displacement ($\langle r_{\rm bh} \rangle$) in terms of structural quantities as the core radius ($r_{\rm c}$), mass ($M_{\rm c}$), and velocity dispersion ($\sigma_{\rm c}$), in addition to the average stellar mass ($m_{\rm c}$) and the IMBH mass ($M_{\rm bh}$). The model can be expressed by the equation $\langle r_{\rm bh} \rangle / r_{\rm c} = A(m_{\rm c}/M_{\rm bh})^{\alpha}[\sigma_{\rm c}^2 r_{\rm c}/(GM_{\rm c})]^{\beta}$, in which the free parameters A, α, β are calculated through comparison with the numerical results on the IMBH displacement. The model is then applied to Galactic GCs, finding that for an IMBH mass equal to 0.1% of the GC mass, the typical expected displacement of a putative IMBH is around $1''$ for most Galactic GCs, but IMBHs can wander to larger angular distances in some objects, including a prediction of a $2.5''$ displacement for NGC 5139 (ω Cen), and $> 10''$ for NGC5053, NGC6366 and ARP2.

3.1 Introduction

Investigating the existence of intermediate-mass black holes (IMBHs) in the Universe is a central goal in modern theories of galaxy evolution. In fact, IMBHs with masses in the range $10^2 - 10^5\ M_{\odot}$ would represent the missing link between the well-known populations of the stellar BHs ($\lesssim 50\ M_{\odot}$; see, e.g., Gies & Bolton 1986, Orosz et al. 2011, and the recent gravitational waves detections Abbott et al. 2016b, Abbott et al. 2016a, Abbott et al. 2017), which represent the final result in the evolution of massive stars, and the supermassive BHs ($\gtrsim 10^5\ M_{\odot}$; see, e.g., Ghez et al. 2008, Bentz et al. 2014, Czerny et al. 2016), which are ubiquitously observed at the centres of galaxies.

In recent years, globular clusters (GCs) have been indicated as promising candidates for hosting a central IMBH. Because of their high density cores ($\sim 10^{3-4}\ M_{\odot}\ {\rm pc}^{-3}$), they might represent optimal environments to grow IMBHs through runaway collapse of massive stars at their formation (see, e.g., Portegies Zwart & McMillan 2002, Portegies Zwart et al. 2004b Giersz et al. 2015). Alternatively, ejecta from first-generation massive stars might collect in the core of GCs, where the high gas density can lead to substantial accretion onto an existing BH seed (see Vesperini et al. 2010). Another motivation to establish whether IMBHs are present in GCs is connected to the $M_{\bullet} - \sigma$ relation (see Ferrarese & Merritt 2000; Gebhardt et al. 2000) between the mass of the supermassive BH and the average velocity dispersion in the bulge of galaxies. Given the range of typical core velocity dispersions in GCs, the existence of IMBHs would imply that this relation continues to be valid also in the low-mass regime (see, e.g., Lützgendorf et al. 2013b).

Yet, despite significant recent efforts to confirm (or falsify) these arguments, a clear evidence for the presence of IMBHs in GCs is still missing. Many differ-

ent observational techniques can be used to identify IMBHs (see Mezcua 2017 for a review). One possible method relies on the detection of both X-ray and radio emission associated, respectively, to the accretion flow of gas onto the BH and to the synchrotron radiation from the emitted jets (Strader et al., 2012). In particular, X-ray and radio observations can be used together to discriminate an IMBH against other plausible emitters and, thus, to set quantitative constraints on the IMBH mass (see Merloni et al. 2003; Falcke et al. 2004). These observations, however, are complicated by the typical lack of gas in GCs (see, e.g, Farrell et al. 2012; Mezcua et al. 2013; Haggard et al. 2013). One illustrative case is represented by the centre of the globular cluster G1 in M31 (Pooley & Rappaport, 2006), for which no clear sign of radio activity associated to the X-ray source has been found (see Ulvestad et al. 2007 and Miller-Jones et al. 2012 for details).

Another method for IMBH detection in GCs is represented by stellar dynamics measurements. This approach has led to the majority of the recent observational claims of detection in GCs, and, in a few instances, to debated results when applied to the same object (e.g., Omega Centauri in Noyola et al. 2010 and van der Marel & Anderson 2010 or NGC 6388 in Lanzoni et al. 2013 and Lützgendorf et al. 2013a, 2015). For this method the constrains on the IMBH mass are generally determined by fitting the observed velocity dispersion profile with a family of Jeans models (see, e.g., van der Marel & Anderson 2010). These models are typically constructed by making assumptions on the mass-to-light ratio profile $M/L(r)$ in order to calculate the intrinsic mass distribution of the visible stars from the surface brightness profile. This represents a crucial and delicate step for the traditional Jeans modeling. In fact, a population of centrally concentrated dark remnants would be able to increase the inner M/L profile and, thus, to produce effects on the kinematics of the luminous component similar to those of a central IMBH (see e.g., Arca-Sedda 2016; Peuten et al. 2017; Gieles et al. 2017). Further challenges for this method are represented by the necessity to make assumptions on the presence (or absence) of velocity anisotropy (see e.g. Zocchi et al. 2017), and on the symmetry of the system. Finally, observations need to be able to measure accurately the velocity dispersion profile within the BH sphere of influence, which is expected to be limited to a few arcsec for most GCs.

Another opportunity for IMBH detection is through the use of modern interferometers (see, e.g., Mandel et al. 2008; Konstantinidis et al. 2013; MacLeod et al. 2016), which can be able to detect the gravitational waves produced by possible mergers of massive compact objects into the IMBH.

Finally, other complementary approaches are focused on indirect evidence of the IMBH presence. N-body numerical simulations suggest that a central IMBH is expected to form a shallow cusp in the projected surface brightness profile and to prevent the core collapse by enhancing three-body interactions within its sphere of influence (see e.g, Baumgardt et al. 2005). In addition, IMBHs are shown to quench the phenomenon of mass segregation (see e.g. Trenti et al. 2007a; Gill et al. 2008; Pasquato et al. 2016) and energy equipartition (Trenti & van der Marel, 2013), and such suppression may be constrained observationally through measurements of pulsar acceleration (Kızıltan et al., 2017). However, measuring these effects in real GCs do not represent a sufficient condition to infer the existence of

IMBHs, as other dynamical processes could be responsible for the same signatures (see e.g. Hurley 2007; Trenti et al. 2010; Vesperini et al. 2010).

Especially for dynamical modeling that rests on (spherical) symmetry assumptions, such as Jeans modeling of the surface brightness and velocity dispersion profiles, one possible source of systematic uncertainties may be represented by the wandering of the IMBH around the centre of the system (see e.g., Giersz et al. 2015, Haster et al. 2016, de Vita et al. 2017). From a dynamical point of view, the IMBH describes a random motion as a consequence of continual fluctuations in the global gravitational field induced by star encounters. The classical treatment for a point mass $M_{\rm bh}$, assuming energy equipartition with the background stars in the globular cluster's core, requires that $M_{\rm bh}\sigma_{\rm bh}^2 = m_{\rm c}\sigma_{\rm c}^2$, where $m_{\rm c}$ is the typical mass of a field star and $\sigma_{\rm bh}^2$, $\sigma_{\rm c}^2$ are the velocity dispersions of the IMBH and the field stars, respectively. Under the assumption that the IMBH moves in a specific gravitational potential, a simple model for the IMBH displacement can be obtained (see Bahcall & Wolf 1976b; Merritt 2001). However, this way of describing the IMBH motion is based on simplifying assumptions which need to be tested and potentially refined in order to reproduce the general behaviour found in N-body simulations.

The main goal of the present work is to produce a physically motivated model for the IMBH radial displacement by comparison with N-body simulations. The scope of this paper is dual. On one side we aim at identifying the main ingredients that contribute to the complex dynamics of IMBHs in star clusters. On the other side we aim at providing with a simple instrument to estimate the IMBH radial displacement on the base of few observational quantities. The model we propose represents an extension of the one discussed by Bahcall & Wolf (1976b) (see Equation (3.8) below), with two main physical ingredients added (degree of energy partition and core dynamical state), which will be constrained through comparison with numerical simulations. The paper is structured as follows. In Section 3.2 we present the set of simulations used in this work together with important definitions for quantities relevant to our analysis. In Section 3.3, we derive a scaling relation which describes the IMBH average displacement in terms of relevant observational quantities by comparing our model to the simulations. In Section 3.4 we apply the model to an existing catalogue of 85 Galactic GCs in order to give reasonable predictions for the mean radial displacements of IMBHs that are assumed to constitute the 0.1% of the total cluster mass. Finally, in Sect.3.5, we give our conclusions.

3.2 Numerical framework

3.2.1 Set of simulations

The numerical simulations used in this paper are those from MacLeod et al. (2016). The reader is directed to Section 2 of that paper for details. Here we summarise their main characteristics.

The set of direct N-body simulations is produced by means of the NBODY6 distribution (Aarseth 1999, 2003) that embeds the SSE and BSE codes of Hurley

Table 3.1: Table of N-body simulation groups A-D. For each group we report (from left to right) the number of initial stars (N_*); the number of equivalent simulations ($N_{\rm sim}$), which are different realisations of the same initial conditions; the King parameter W_0 and the initial half-mass radius $r_{\rm h,0}$ in pc; the initial IMBH mass in $M_\odot$; the total duration of the simulation in Gyr, and the kick imparted to stellar remnants in terms of the initial cluster velocity dispersion σ_*.

	N_*	$N_{\rm sim}$	W_0	$r_{\rm h,0}$	$M_{\rm bh,0}$	$t_{\rm max}$	σ_k/σ_*
A	100k	3	7	2.3	150	6	2.5
B	100k	3	7	2.3	150	6	1.0
C	100k	3	7	2.3	75	9	2.5
D	200k	4	7	2.3	150	10.4	2.5

et al. (2000, 2002) to account for stellar evolution. Star clusters with $1-2\times10^5$ initial stars (corresponding to low-mass Galactic GCs) are evolved in a realistic tidal field. The stellar distribution of each cluster is initialised following King (1966) models with $W_0=7$. The stars in the initial conditions follow a Kroupa (2001) initial mass function (IMF), within the mass range $0.1-30\ M_\odot$, with no binaries. The metallicity is one-tenth solar.

At the beginning of the simulation, an IMBH of $75-150\ M_\odot$ and with zero velocity is initialised at the centre of mass of the system. The IMBH mass grows modestly during the evolution because of tidal disruption events following close encounters (typically, by the end of the evolution, the IMBH mass increases by a factor $1.2-1.4$, depending on the simulation group). In these events, which take place when the pericenter radius is less than $r_{\rm t}=(M_{\rm bh}/M_*)^{1/3}R_*$, a fraction of the star mass is accreted into the IMBH (for weakly-bound orbits typically half of the mass is retained by the BH).

Finally, MacLeod et al. (2016) consider two different cases for the velocity kicks imparted to stellar remnant (neutron stars and BHs). In both cases remnants are given a kick drawn from a Maxwellian distribution with sigma of either 1 or 2.5 times the initial cluster velocity dispersion, producing different retention fractions of stellar remnants.

The simulations have been divided in 4 groups, which differ for the initial parameters. Within each group, statistically different realisations of the same initial conditions are considered. The main properties of the simulations groups are summarised in Table 3.1.

3.2.2 IMBH displacement definition

In order to characterise the motion of the IMBH in our simulated GCs with respect to the GC centre, we need to properly define a coordinate-independent centre of the system. Following what suggested by Casertano & Hut (1985), we use a density centre for the purpose. For this, we associate to each particle in a snapshot (excluding the IMBH) a local density calculated considering the six closest neighbours. In particular, we define the local density for the i-th star as

$$\rho_i=\frac{M-m_i-m_6}{4/3\pi r_6^3}, \tag{3.1}$$

where m_i is the mass of the i-th star, m_6 and r_6 are the mass and the distance of the sixth neighbour to the i-th star, respectively, and M is the total mass within a sphere of radius r_6 centred in the i-th star position. The density-weighted centre of the system $\vec{x}_\rho$ is then defined by

$$\vec{x}_\rho = \frac{\sum_i \vec{x}_i \rho_i}{\sum_i \rho_i}, \tag{3.2}$$

where $\vec{x}_i = (x_i, y_i, z_i)$ is the position of the i-th star with respect to the initial reference frame. Finally, we consider a mass/density-weighted radius defined as

$$r_\rho = \frac{\sum_i |\vec{x}_i - \vec{x}_\rho| \, \rho_i m_i}{\sum_i \rho_i m_i}. \tag{3.3}$$

As tested in Trenti et al. (2010), the density radius r_ρ generally represents a good estimate for the core radius as determined by fitting the surface-brightness profile with a King model, especially for systems that are not core-collapsed (see Fig. 10 in Trenti et al. 2010). With these definitions, the IMBH radial position can be expressed in a coordinate-independent way as

$$r_{\rm bh} = \sqrt{|\vec{x}_{\rm bh} - \vec{x}_\rho|^2}. \tag{3.4}$$

All the definitions given so far can be easily extended in order to deal with projected and luminosity-weighted quantities. We define the local surface-brightness for the i-th star as

$$\mu_i = \frac{L - l_i - l_6}{\pi R_6^2}, \tag{3.5}$$

where l_i is the luminosity of the i-th star, l_6 and R_6 are the luminosity and the projected distance of the sixth neighbour to the i-th star, respectively, and L is the total luminosity within a circle of radius R_6 centred in the i-th star position. We calculate luminosity-weighted quantities by considering only main-sequence stars, thus avoiding the fluctuations in the light profile that arise from the small number of luminous giants. Moreover, we consider stars with mass higher than $0.4 M_\odot$ in order to exclude the faint end of the main sequence, since those stars would be likely unresolved in typical GC observations. For main sequence stars we assume that luminosity scales with mass as $l \propto m^{7/2}$. Then, the 2 dimensional luminosity centre $\vec{X}_\mu$ is obtained by projecting the stars' positions along the z-axis and by replacing ρ_i with μ_i in Equation (3.2):

$$\vec{X}_\mu = \frac{\sum_i \vec{X}_i \mu_i}{\sum_i \mu_i}, \tag{3.6}$$

where $\vec{X}_i = (x_i, y_i)$. Finally, analogous to the mass/density-weighted radius in Equation (3.3) is the surface-brightness density radius R_μ, which is defined by

$$R_\mu = \frac{\sum_i \left|\vec{X}_i - \vec{X}_\mu\right| \mu_i l_i}{\sum_i \mu_i l_i}. \tag{3.7}$$

3.2.3 IMBH displacement results

For one simulation in group A, we report in Fig. 3.1 the evolution of the ratio of the IMBH displacement along different axes as a function of time. We exclude the first part of the evolution from our analysis because, in this phase, the internal dynamics is still dominated by rapid stellar evolution processes. In particular, there is a significant mass loss as higher mass stars evolve out of the main sequence. From the figure it is evident how the IMBH is experiencing an isotropic motion around the centre. Together with the single values from each snapshot in the simulation, we plot also a running average for the sample. It is worth noting that, when rescaled with the density radius, the displacement on each axis is approximately time-independent.

In Fig. 3.2 we show the displacement distribution in the range 1-5 Gyr for 4 typical simulations, one for each group analysed in this paper (see Table 3.1). As expected, the distributions in each direction are well fitted by a normal distribution with zero mean, suggesting that the IMBH is actually experiencing a Brownian random motion. This motivates and justifies the approach to consider only radial quantities for further analysis.

Finally, in Fig. 3.3 we report the radial displacement evolution for the 4 groups of simulations considered. For all the simulations, the minimum average displacement for the IMBH is $\gtrsim 0.02\, r_\rho$ with 95% confidence. According to the classic derivations for the Brownian motion of a point mass object, the IMBH mean radial displacement $\langle r_{\rm bh} \rangle$ in terms of the density radius r_ρ is represented by

$$\frac{\langle r_{\rm bh} \rangle}{r_\rho} \approx \left(\frac{m_\rho}{M_{\rm bh}} \right)^{1/2}, \tag{3.8}$$

where m_ρ is the average stellar mass within the density radius. This result is obtained by Bahcall & Wolf 1976b under the assumptions that the IMBH is a single object in complete energy equipartition with the surrounding stars in the core and is moving in an harmonic potential well. For typical values in our simulations, $m_\rho \approx 0.65 M_\odot$ and $M_{\rm bh} \approx 150 M_\odot$, we have $\langle r_{\rm bh} \rangle / r_\rho \approx 0.07$, which is in good agreement (at least as order of magnitude estimate) with the measured displacements. In addition, the radial IMBH displacement increases significantly in the group of simulations with the less massive IMBH (see group C). Moreover, both the different way of treating the velocity kicks imparted to stellar remnants and the initial number of stars seems to play a secondary role in the IMBH wandering (compare groups A, B and D).

3.3 A scaling relation for the IMBH displacement

3.3.1 Physical foundations

The basic assumption behind Equation (3.8) is that the IMBH has reached a state of energy equipartition with the surrounding stars in the core. As shown in Trenti & van der Marel (2013), a condition of complete energy equipartition is not achieved in the context of direct N-body simulations. Thus, for our purposes,

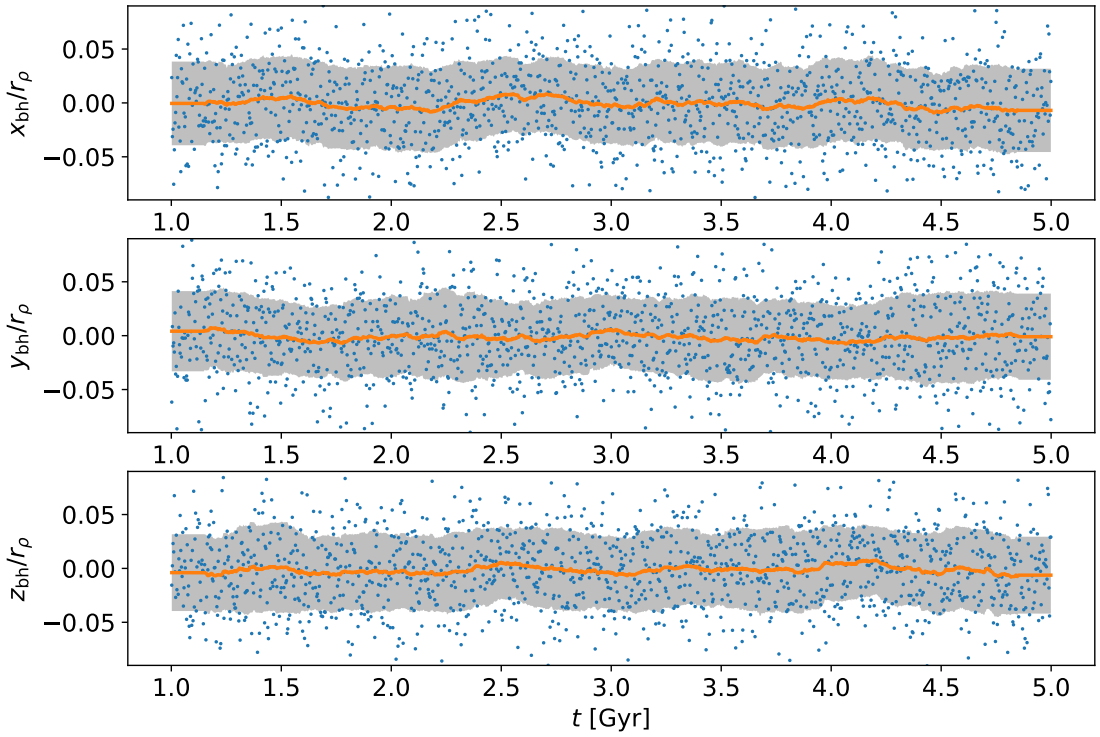

Figure 3.1: Evolution of the IMBH displacement relative to the density radius ($\sim$ core radius) for one simulation in group A in each direction. Each data point represents a single measurement coming from one snapshot of the simulation. The orange line is a running average, calculated by averaging the values obtained from 50 snapshots, corresponding to roughly 150 Myr. The shaded area encloses two standard deviations with respect to the running average (one above and one below).

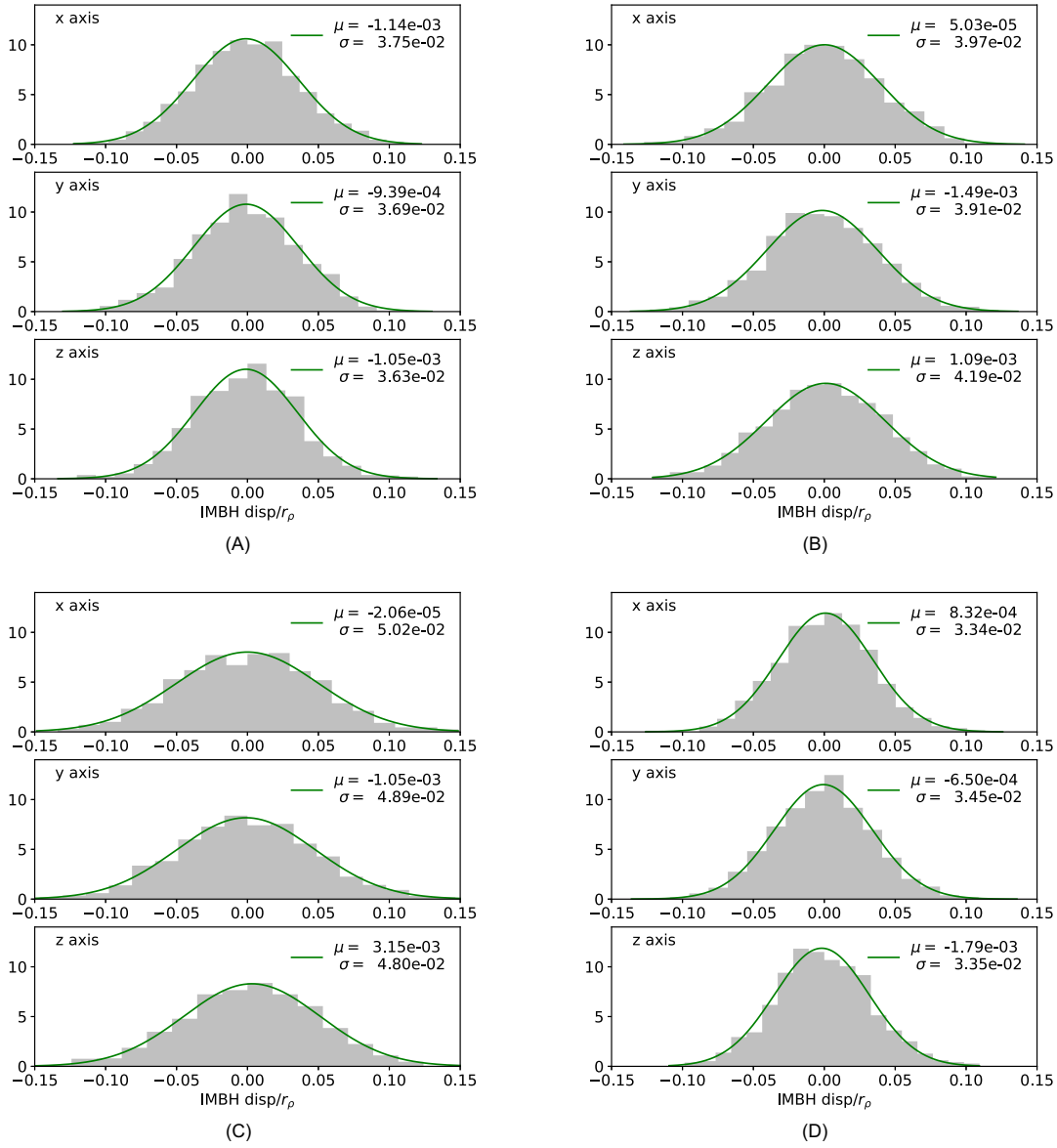

Figure 3.2: Distribution of the ratio between the IMBH displacement and the density radius in three directions (x, y, z) for the 4 groups of simulations used in this paper (see Table 3.1) . Each distribution refers to the time interval 1-5 Gyr and is fitted with a Gaussian distribution with mean value μ and standard deviation σ. The average displacement, identified as the σ of the best-fit normal distribution, is higher in panel C which shows the simulation with the less massive IMBH (75 $M_\odot$).

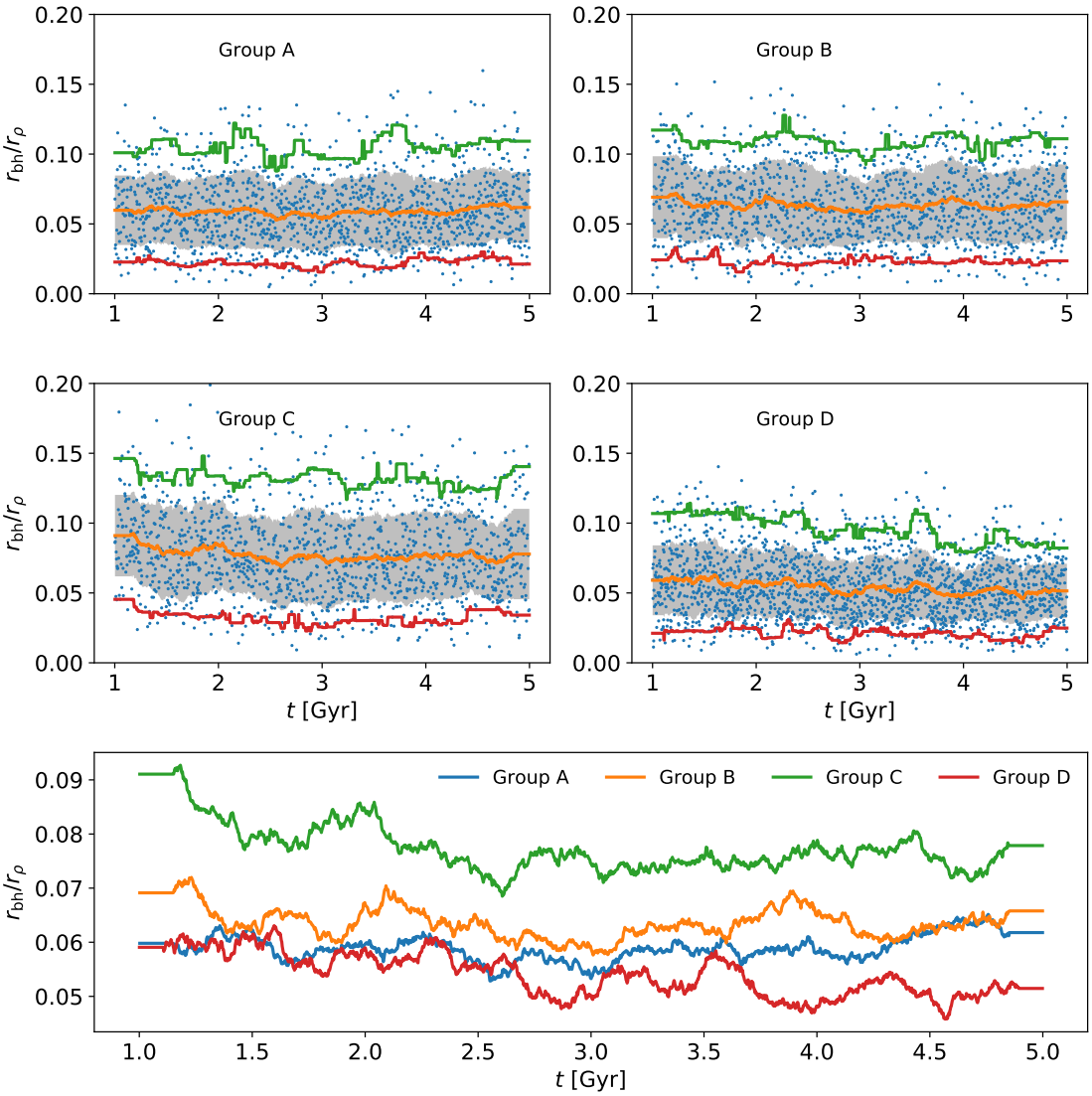

Figure 3.3: Evolution of the IMBH displacement for 4 simulations, one for each group analysed in this paper (see Table 3.1). *Upper panels:* each data point represents a single measurement of the ratio $r_{\rm bh}/r_\rho$ coming from one snapshot of the simulation. The orange, red and green line represent respectively the running average, the 5% quantile and the 95% quantile, calculated from the distribution of the values obtained from 50 snapshots, corresponding to roughly 150 Myr for groups A-B-C and to 100 Myr for group D. The shaded area encloses two standard deviations with respect to the running average (one above and one below). The average IMBH displacement slightly varies during the evolution as a direct consequence of processes as mass segregation in the core (m_ρ increases), IMBH accretion ($M_{\rm bh}$ increases) and core collapse (r_ρ decreases). *Lower panel:* Running averages for each group above but shown in a a single plot for direct comparison. On average, the displacement in group C (low-mass IMBH) is significantly higher than the others.

we will consider a more general relation between the IMBH velocity dispersion $\sigma_{\rm bh}$ and the core velocity dispersion $\sigma_{\rm c}$:

$$\sigma_{\rm bh}^2 = \left(\frac{m_{\rm c}}{M_{\rm bh}}\right)^{2\alpha} \sigma_{\rm c}^2, \tag{3.9}$$

where α is a free parameter that measures the degree of energy equipartition in the core (we expect $0 \leq \alpha < 0.5$).

If we Taylor expand a King potential (King, 1966) in $\langle r_{\rm bh} \rangle \approx 0$ and we equal the IMBH kinetic energy with its gravitation potential energy, we are able to associate the IMBH velocity dispersion to a physical mean displacement. In particular, given the total mass $M_{\rm c}$ enclosed in the core radius $r_{\rm c}$, we have

$$\sigma_{\rm bh}^2 \propto \frac{GM_{\rm c}}{r_{\rm c}} \left(\frac{\langle r_{\rm bh} \rangle}{r_{\rm c}}\right)^2, \tag{3.10}$$

where, for King models, the constant of proportionality is determined by fixing the central dimensionless potential W_0. By substituting $\sigma_{\rm bh}^2$ using the combination of Equation (3.9) and Equation (3.10), the mean IMBH displacement can be expressed as

$$\frac{\langle r_{\rm bh} \rangle}{r_{\rm c}} \propto \left(\frac{m_{\rm c}}{M_{\rm bh}}\right)^{\alpha} \left(\frac{\sigma_{\rm c}^2 r_{\rm c}}{GM_{\rm c}}\right)^{1/2}. \tag{3.11}$$

Finally, in order to be more general, we define the exponent of the factor $\sigma_{\rm c}^2 r_{\rm c}/(GM_{\rm c})$ as β and consider it as a free parameter related to the dynamical state of the core.

In conclusion, we obtain the following equation for the average IMBH displacement

$$\frac{\langle r_{\rm bh} \rangle}{r_{\rm c}} = A \left(\frac{m_{\rm c}}{M_{\rm bh}}\right)^{\alpha} \left(\frac{\sigma_{\rm c}^2 r_{\rm c}}{GM_{\rm c}}\right)^{\beta}, \tag{3.12}$$

with A, α and β free parameters of the model.

The main goal of this work is to find the parameters' values that best represent our simulations. We wish to emphasis here that our model intentionally relies on a low number of free parameters. This choice is motivated by the aim of describing a complex dynamical phenomenon with the minimal number of ingredients, which are based on understandable and basic physical arguments. Despite its simplicity, the number of free parameters is still higher with respect to the model of Equation (3.8) presented by Bahcall & Wolf (1976b), but we show in Subsection 3.3.3 that the addition of β is supported by data-model comparison.

3.3.2 Binary versus three-body interactions

One possible extension for the physical treatment presented in the previous Subsection is to consider the IMBH as one component of a binary system (see Merritt 2001), which is the most likely IMBH dynamical state observed in numerical simulations (see MacLeod et al. 2016). The Brownian motion of a binary in a background field differs from that of a single massive object because of inelastic scattering events. These occur when a perturber star strongly interacts with the binary, and is ejected after one or several encounters carrying away part of the

binary binding energy, thus not conserving the total kinetic energy of the three-body system. If the binary mass is much greater than the average field mass, the net result of many close three-body interactions is to increase the recoil velocity of the binary centre of mass as a consequence of linear momentum conservation.

Merritt (2001) compares the rate of diffusion in the velocity of the binary due to three-body superelastic scatterings $\langle(\Delta v)^2\rangle_{\rm se}$, with that of a point mass due to two-body encounters $\langle(\Delta v)^2\rangle_{\rm C}$ (see Equations 3 to 11 in that paper). The ratio of these quantities is given by

$$\frac{\langle(\Delta v)^2\rangle_{\rm se}}{\langle(\Delta v)^2\rangle_{\rm C}} \sim \frac{H}{32\sqrt{2\pi}\log\Lambda}, \tag{3.13}$$

where $\log\Lambda$ is the Coulomb logarithm, which for typical GCs is $3 \lesssim \log\Lambda \lesssim 5$ (see, e.g., Bertin 2014) and H represents the hardening rate of the binary. From three-body scattering experiments, even for hard binaries (i.e., those for which $\sqrt{GM_{12}/a} \gg \sigma_{\rm c}$, with M_{12} total binary mass and a semi-major axis), $H \lesssim 20$ for a wide range of mass ratios (see Quinlan 1996). Thus, Equation (3.13) implies that the enhancement of the IMBH random motion via three-body encounters might be negligible at first instance ($\approx 6\%$ correction). This conclusion seems even more appropriate for massive star clusters (we recall that the numerical simulations used in this paper may only represent the low-mass end of the Galactic GCs' system). In fact, we expect the $\log\Lambda$ term in Equation (3.13) to slightly increase with the number of stars, reducing the impact of three-body encounters on the binary diffusion rate.

To further investigate the impact of three-body interactions, we directly searched for a correlation between the IMBH radial displacement and three-body scattering events in our fiducial simulation (group A in Table 3.1). We flagged the three-body interactions as those where the IMBH is one component of an hard binary system for which $r_{\rm p}/a < 3$, with $r_{\rm p}$ representing the closest approach distance of a perturber star to the binary. In Fig. 3.4 we plot the displacement evolution in comparison with the ratio $a/r_{\rm p}$. In order to characterise a possible dependence between the two signals, we calculated the discrete correlation function by means of the `pyDCF` software (see Robertson et al. 2015), which is specifically designed to deal with unevenly sampled time series. We expect this function to be peaked at a certain lag time $t_{\rm lag}$ if $r_{\rm bh}$ increments follow close three-body scattering events (those for which $a \gg r_{\rm p}$) with a characteristic time delay $t_{\rm lag}$. The cross-correlation coefficients are shown in Fig. 3.4. The time range considered for $t_{\rm lag}$ is of the order of the typical half-mass relaxation time $0.5{\rm Gyr} \lesssim {\rm t_{rh}} \lesssim 1.5{\rm Gyr}$ (see Trenti et al. 2010 for a definition). Note that we plot the amplitudes of the correlation also for negative values of $t_{\rm lag}$. Quantifying the amplitude of such correlations (which are not expected to be present in the system) provides us with a characteristic noise level that can be directly and easily compared with the amplitudes of interest in the range $t_{\rm lag} > 0$, showing that there is no difference in amplitudes and thus that the correlations at positive lag times are dominated by noise.

Overall, all these tests confirm that inelastic scattering events are not dominating the IMBH radial displacement variations and thus we neglect them in the following analysis.

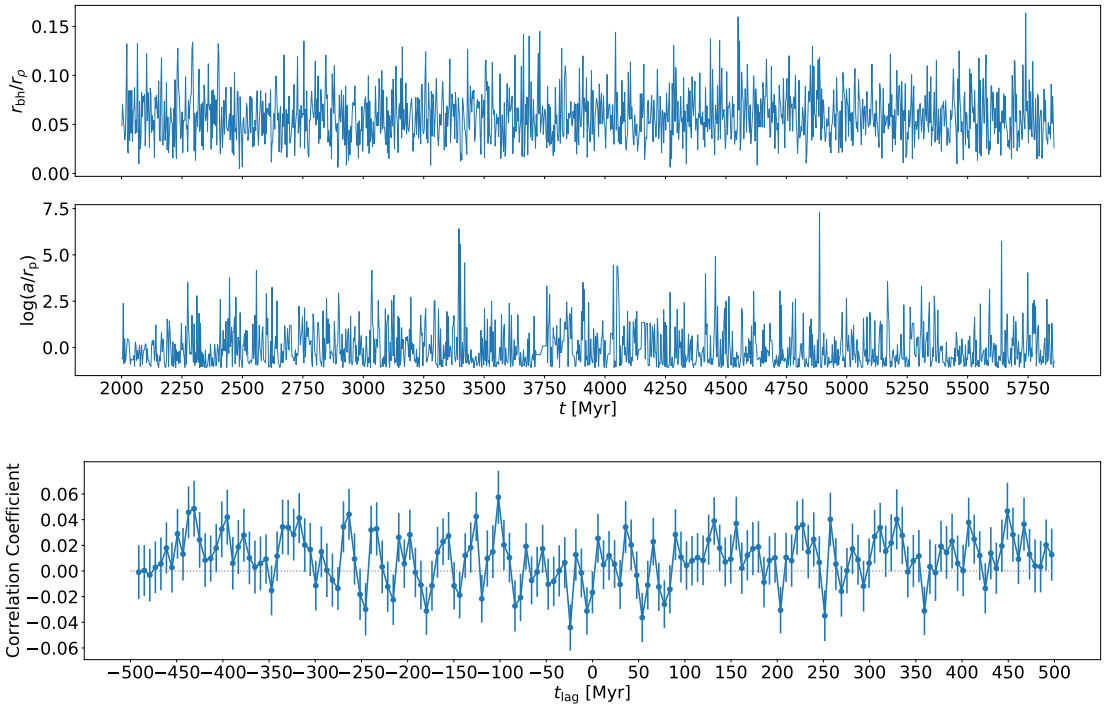

Figure 3.4: Cross-correlation of the IMBH radial displacement with three-body interactions. *Upper panels:* evolution of the IMBH radial displacement compared to the most energetic three-body events quantified by the ratio a/r_p of the semi-major axis of a binary with the IMBH and the closest distance of a perturber star. *Lower panel:* discrete correlation coefficients of the two time signals r_bh/r_ρ and a/r_p as function of the lag time. The low and uniformly distributed values of the coefficients might suggest that the IMBH radial displacement is not significantly affected by strong three-body encounters. The dynamical time for the simulation is $t_\mathrm{dyn} \approx 0.3$ Myr.

3.3.3 Results

In Fig. 3.5 we plot the evolution of the 3D mass-weighted density radius r_ρ, of the 2D luminosity-weighted surface brightness radius R_μ and of the IMBH radial displacement, both intrinsic $r_{\rm bh}$ and projected $R_{\rm bh}$. In order to test the ability of the model in Equation (3.12) to predict the IMBH displacement, we divide the range $4-5.5$ Gyr for simulations A-B and the range $4-7$ Gyr for simulations C-D into equal time intervals of 0.3 Gyr each. The time ranges are selected both to exclude the post core-collapse phase in which the density radius oscillates rapidly and to avoid the first part of the evolution dominated by stellar evolution and characterised by high discrepancy between the luminosity-based and mass-based radii. For each time interval we compare the direct measurement of the average IMBH displacement (presented in Subsection 3.2.3) with the displacement predicted by the model. We carry out this analysis for both 3D mass-weighted and 2D luminosity-weighted quantities. Accordingly, we replace the core terms in Equation (3.12) with corresponding quantities in each case (see subsections below).

In both cases we are able to obtain a total of $N = 100$ measurements for the relevant quantities in our model averaged over the 0.3 Gyr time interval (the average over time is indicated using the brackets $\langle ...\rangle$). Then, the fit of the model to the data is carried out by maximising the Gaussian likelihood function

$$\ln \mathcal{L} = -\frac{1}{2}\sum_{i=1}^{N}\left[\frac{f_i(A,\alpha,\beta) - \langle \log\left(r_{\rm bh}/r_{\rm c}\right)\rangle_i}{\delta_i}\right]^2, \tag{3.14}$$

with respect to the free parameters A, α and β. Here δ_i is the standard error of $\langle \log\left(r_{\rm bh}/r_{\rm c}\right)\rangle_i$ and f_i is the model prediction (see Equation 3.12) defined by

$$f_i \equiv \log A + \alpha\left\langle \log\left(\frac{m_{\rm c}}{M_{\rm bh}}\right)\right\rangle_i + \beta\left\langle \log\left(\frac{\sigma_{\rm c}^2 r_{\rm c}}{G M_{\rm c}}\right)\right\rangle_i. \tag{3.15}$$

The maximisation process is performed using a Markov chain Monte Carlo (MCMC) estimator (see Foreman-Mackey et al. 2013).

Mass-based analysis

For the mass-based analysis we rely on the maximum information available from the simulations, and use the intrinsic core radius with the intrinsic density radius defined by Equation (3.3) as proxy for $r_{\rm c}$. Similarly, the average stellar mass in the core $m_{\rm c}$ and the total core mass $M_{\rm c}$ are replaced by the same quantities calculated within the density radius (we will use the the subscript ρ instead of c to indicate quantities calculated within the density radius). Finally, we replace the core velocity dispersion $\sigma_{\rm c}$ with the 3D velocity dispersion σ_ρ, calculated from the velocity standard deviations along each axis of the stars (including dark stellar remnants) within the density radius.

In Fig. 3.6 we show the result of the fit. In particular, we plot the relative difference between the IMBH displacement (relative to the density radius) measured in the simulations to the corresponding displacement calculated with the best fit

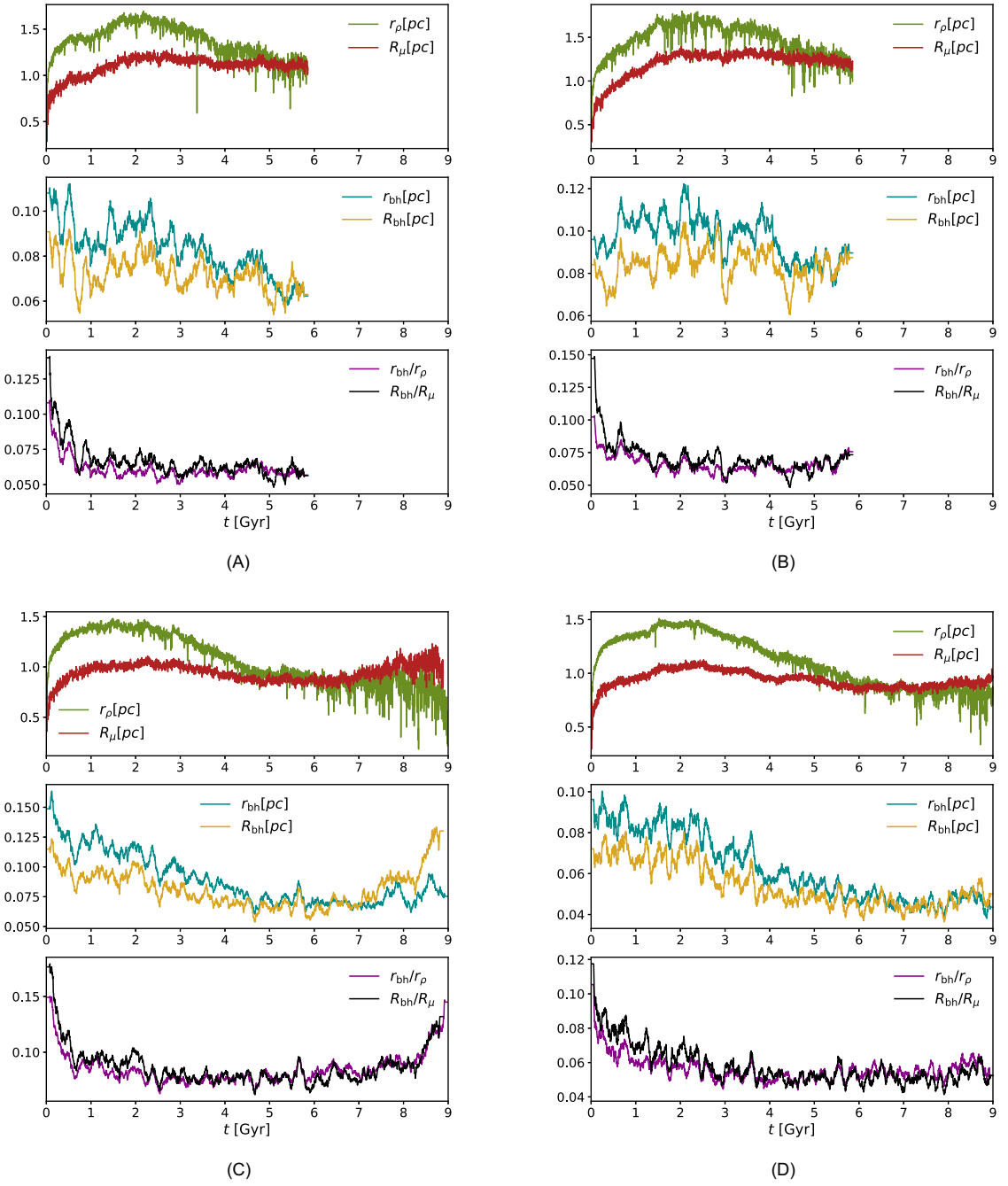

Figure 3.5: Evolution of the 3D mass-weighted density radius r_ρ, the 2D luminosity-weighted surface brightness radius R_μ, the intrinsic ($r_{\rm bh}$) and the projected ($R_{\rm bh}$) IMBH radial displacement for the 4 groups of simulations used in this paper (see Table 3.1).

model. In addition, we report the histograms produced by the MCMC code to sample the parameter space. The best-fit value $\alpha = 0.48 \pm 0.01$ suggests that the IMBH is very close to a state of complete energy equipartition with the surrounding stars. [*] Moreover, we find that a non-zero value of β is needed in order to reproduce the data. This result supports the introduction of an additional parameter in our model related to the shape of the overall gravitational potential (see discussion in Subsection 3.3.1). The chi-square per degree of freedom calculated with the best fit parameters is $\tilde{\chi}^2_{\rm bf} = 1.08$, which corresponds to a 0.55σ deviation from the expected median value $\tilde{\chi}^2_{\rm bf} = 1$, and indicates that our model describes the numerical data well.

Finally, we test the quality of the fit performed with the model in Equation (3.12) against other three models that rely on a lower number of free parameters. These models are readily obtained from Equation (3.12) by imposing respectively (i) $\alpha = 0.5$ and $\beta = 0$; (ii) $\beta = 0$ and (iii) $\alpha = 0.5$. The first case represents the one-dimensional model of Bahcall & Wolf (1976b) expressed in Equation (3.8), while the second case is the corresponding 2-dimensional version in which the hypothesis of complete energy equipartition has been relaxed. Finally, in the third case, the dynamical state of the core (as measured by β) is the only physical parameter, with the degree of energy equipartition fixed to its maximum value.

In Fig. 3.7, we plot the best-fit of the data through the most simple model of Equation (3.8). The relevant best-fit values relative to the four different models are reported in Table 3.2. From the Akaike information criterion [†] (see, e.g., Liddle 2007) we can conclude that the model in Equation (3.12) (for which AIC ≈ 110) and the analogous model with the constraint $\alpha = 0.5$ (for which AIC ≈ 111) are generally more appropriate to describe the IMBH dynamical behaviour when compared to the others (for which AIC ≈ 290). A likelihood ratio test for the model with $\alpha = 0.5$ gives a value of 2.79, indicating marginal significance (at the 90% confidence level) that the modeling needs to allow for a departure from full-energy equipartition of the IMBH. Motivated by this, for the following analysis we adopt the most general model expressed by Equation (3.12). However, we would expect to find similar results for the $\alpha = 0.5$ model.

Luminosity-based analysis

For an easier application of our model for the IMBH displacement to observed globular clusters, we carry out also an analysis in which the quantities involved are projected and luminosity-weighted. Thus we decide to replace the intrinsic core radius in the model presented in Subsection 3.3.1 with the projected surface-brightness density radius R_μ, defined in Equation (3.7). Following the convention used for the mass-weighted analysis we use the subscript μ to indicate quantities

[*] Note that the near-complete energy equipartition for a single massive remnant does not imply that the whole cluster's core is in the same dynamical state, and our finding is consistent with the results of Trenti & van der Marel (2013), which highlight that massive (dark) remnants have a higher degree of equipartition compared to visible stars because of their rarity.

[†] The AIC is defined by AIC $= -2\ln\mathcal{L}_{\rm bf} + 2k + 2k(k+1)/(N-k-1)$, where $\mathcal{L}_{\rm bf}$ is the maximum likelihood from the fit of a model with k degrees of freedom to N data points. The best model is the one which minimises AIC.

Table 3.2: Quality of the fit. For four models (specified by Equation 3.12) with different degrees of freedom (k), we report the best-fit parameters ($\alpha_{\rm bf}$, $\beta_{\rm bf}$), the minimum chi-square ($\chi^2_{\rm bf}$), the reduced chi-square ($\tilde{\chi}^2_{\rm bf}$), the deviation of $\tilde{\chi}^2_{\rm bf}$ from 1 in terms of the variance (σ^2) of the $\tilde{\chi}^2$ distribution, and the AIC value.

k	$\alpha_{\rm bf}$	$\beta_{\rm bf}$	$\chi^2_{\rm bf}$	$\tilde{\chi}^2_{\rm bf}$	$(\tilde{\chi}^2_{\rm bf}-1)/\sigma$	AIC
1	0.5	0	286.79	2.89	13.34	288.80
2	0.49 ± 0.03	0	285.57	2.91	13.40	289.57
2	0.5	0.54 ± 0.04	107.36	1.09	0.67	111.36
3	0.48 ± 0.01	0.55 ± 0.04	104.57	1.07	0.54	110.57

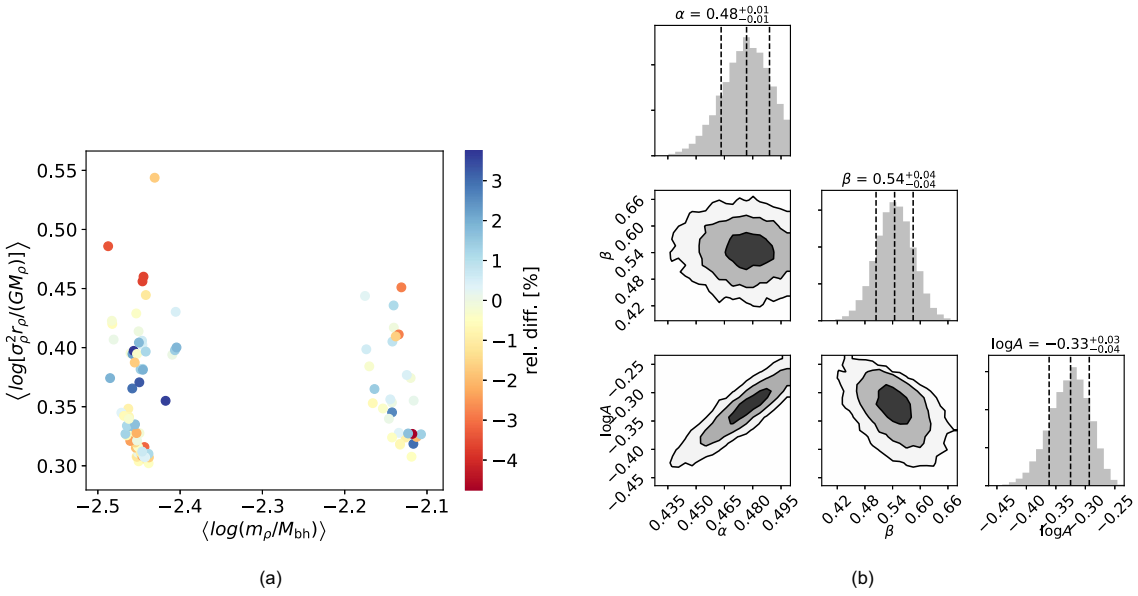

Figure 3.6: Best fit model for the IMBH displacement. Panel (a) shows a map of the IMBH displacement residuals, namely the relative difference between the displacement calculated with the model and the displacement measured in the simulation. Panel (b) shows the 1-D and 2-D histograms produced with the maximum likelihood estimator. The best fit values for $\log A$, α and β are reported together with 1σ, 2σ and 3σ confidence levels. The chi-square per degree of freedom for this data set is $\tilde{\chi}^2_{\rm bf} = 1.08$ (0.55σ).

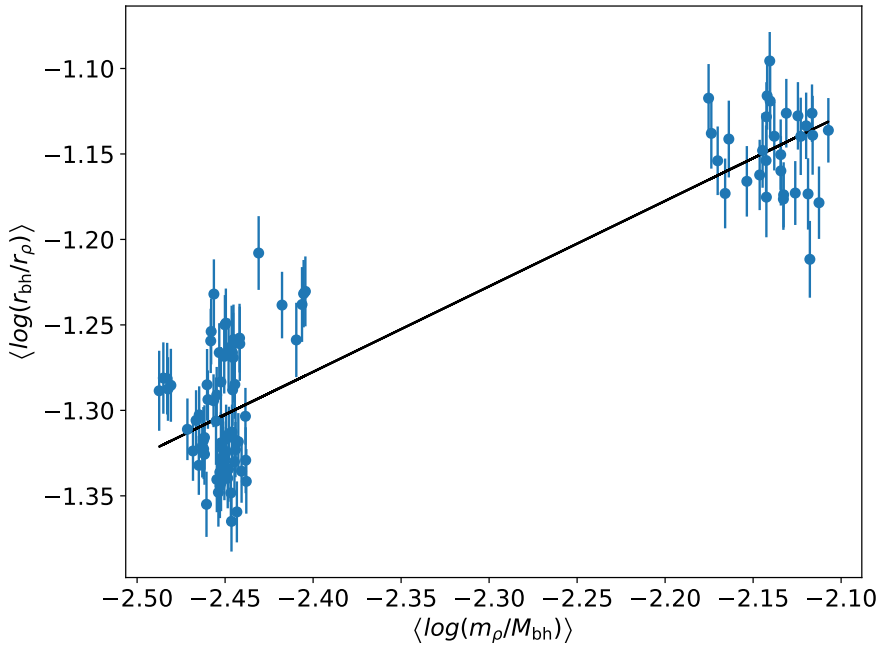

Figure 3.7: Linear fit of the IMBH displacement predicted by Equation (3.8), namely the model of Equation (3.12) with constrains $\alpha = 0.5$ and $\beta = 0$. The mean relative displacement is reported as function of the ratio $m_\rho/M_{\rm bh}$ and the best linear fit of the data is shown. The chi-square per degree of freedom for this data set is $\tilde{\chi}^2_{\rm bf} = 2.89$ (13.3σ).

calculated within R_μ. With this convention, m_μ and M_μ represent the average stellar mass and the total mass calculated by considering all the stars (including dark remnants) enclosed in a projected circle with radius R_μ. Finally, we indicate with $\sigma_{0,z}$ the standard deviation of the velocities along the z-axis of the luminous stars (namely main sequence stars with mass greater than $0.4M_\odot$) within a small circle around the centre (with radius $\approx 5\%$ of R_μ).

In Fig. 3.8 we show the result of the fit based on luminosity-weighted and projected quantities. The chi-square per degree of freedom calculated with the best fit parameters is $\tilde{\chi}^2_{\rm bf} = 1.66$, which corresponds to a 4.60σ deviation from the expected median value $\tilde{\chi}^2_{\rm bf} = 1$. Overall, even if luminosity-based quantities are less effective as input for the dynamical modeling compared to mass-based measurements, we find good agreement between the best-fit parameters. This suggests that the model we present provides a basic yet effective tool to estimate the IMBH radial displacement on the basis of few parameters which are broadly available from GC observations.

3.4 Wandering of putative IMBHs in Galactic globular clusters

With the model presented in Subsection 3.3.1, we have a tool to calculate the displacement expected in Galactic globular clusters. If applied to Equation (3.12), the best fit values found in the luminosity-based analysis give the final version of

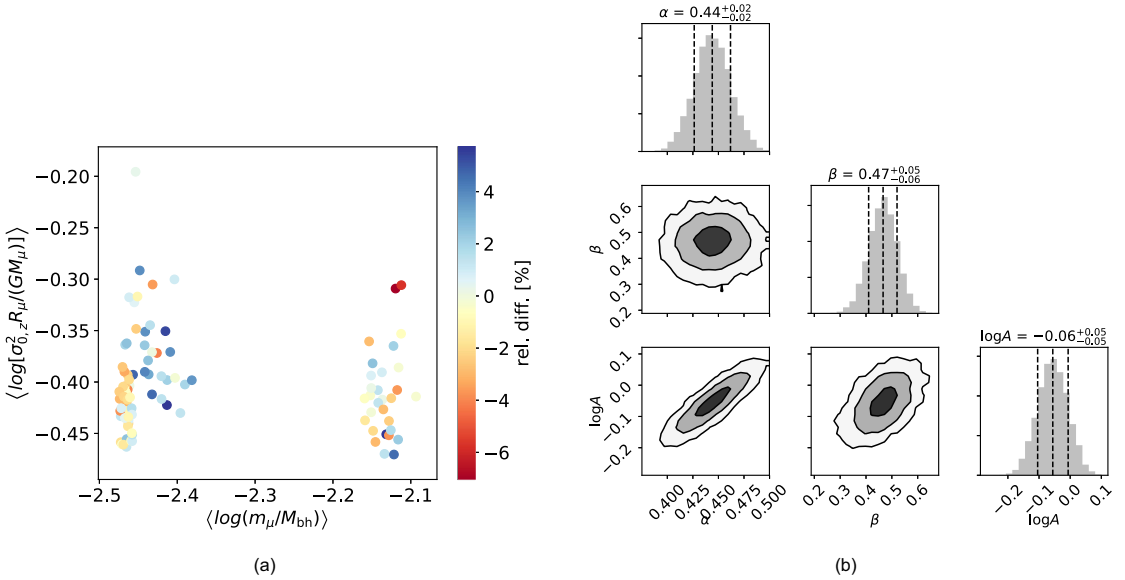

Figure 3.8: See Fig. 3.6 for a detailed description. The chi-square per degree of freedom for this data set is $\tilde{\chi}^2_{\rm bf} = 1.66$ (4.60σ).

the expected mean IMBH displacement:

$$\langle R_{\rm bh}\rangle \approx 0.055 \left(\frac{5{\rm km/s}}{\sigma_{0,z}}\right)^{0.94} \left(\frac{m_\mu}{0.6 M_\odot}\right)^{0.44} \times \\ \times \left(\frac{150 M_\odot}{M_{\rm bh}}\right)^{0.44} \times \left(\frac{1{\rm pc}}{R_\mu}\right)^{0.47} \times \\ \times \left(\frac{M_\mu}{3\times 10^3 M_\odot}\right)^{0.47}. \qquad (3.16)$$

We consider the McLaughlin & van der Marel (2005) catalogue to analyse the best fit King models of 85 Galactic GCs. We used the tabulated W_0, core radius, and total inferred mass of the cluster to constraint a King model. Then, with the use of the limepy software developed by Gieles & Zocchi (2015), we derived relevant quantities as the central projected velocity dispersion ($\sigma_{0,z}$), and the total mass enclosed in the core radius ($\sim M_\mu$). Finally we identify R_μ with the tabulated projected core radius, and we considered a fixed average stellar mass $m_\mu = 0.65\ M_\odot$ and a fixed ratio $M_{\rm tot}/M_{\rm bh} = 10^3$ for every cluster.

In Fig. 3.9 we plot the IMBH displacements calculated with our model for the selected sample of GCs. For the majority of the clusters the average IMBH radial displacement is around $1''$, with some outliers (NGC5053, NGC6366, and ARP2) showing a $\gtrsim 10''$ displacement. According to our analysis, the debated case of ω Cen (see, e.g., the $\sim 3.5''$ discrepancy in the determination of the centre position between Noyola et al. 2010 and Anderson & van der Marel 2010), is expected to show a rms displacement of $\approx 2.5''$ from the light center of the system. Another debated system in the literature is represented by NGC6388 (see Lanzoni et al. 2013 and Lützgendorf et al. 2015), which in our estimate shows a relatively modest rms displacement of less than $0.5''$.

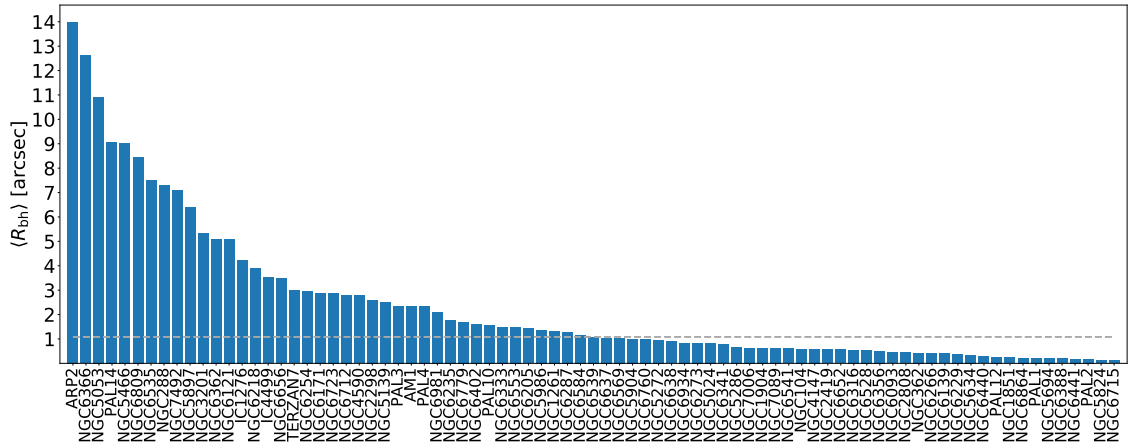

Figure 3.9: Expected IMBH radial displacement as calculated through Equation (3.16) with a fixed ratio $M_{\rm tot}/M_{\rm bh} = 10^3$ for a sample of 85 Galactic GCs in the McLaughlin & van der Marel (2005) catalogue. The dashed horizontal line represents a median value of $\approx 1''$.

In typical integrated-light integral field unit (IFU) observations the instrumental field of view is approximately $10'' \times 10''$ with a spaxel resolution of $0.3'' - 0.5''$, with the latter corresponding to the typical uncertainty in the centre determination (see, e.g., Lützgendorf et al. 2013a). In this observational framework, the IMBH median displacement we estimate for Galactic GCs is not expected to introduce major systematic errors in the IMBH detection (see de Vita et al. 2017). However, effects of larger displacements ($\langle R_{\rm bh} \rangle \gtrsim 2''$) would require tailored data-modeling comparison, since the effects of departure from spherical symmetry may affect the ability to correctly recover an unbiased BH mass. Furthermore, in the case of ω Cen, the best-fit mass inferred from spherical Jeans models may vary up to 30% when cluster centres with a $\sim 10''$ separation are considered (see Noyola et al. 2010). This implies that an accurate observational determination of the dynamical centre of the system and a modeling that account for wandering of a putative central IMBH would be crucial for a precise estimate of its mass and associated uncertainty. In particular, if an IMBH is present off-center and data are analysed through a standard spherically symmetric Jean model, then the recovered IMBH mass is expected to be under-estimated.

3.5 Discussion and conclusions

In this work we analysed the motion of IMBHs around the centres of globular clusters. First, we presented a simple model for the IMBH displacement (see Equation 3.12), which has been constructed based on few physical ingredients and on the comparison with realistic direct N-body simulations. The total number of free parameters of the model has been kept low in order to reduce the complexity of the dynamical processes involved in the IMBH random motion to two main aspects: the dynamical state of the core and the degree of energy equipartition between the IMBH and the field stars. A possible extension of this treatment might contemplate the inclusion of the effect that a IMBH companion

should have on the binary's barycentre motion (Merritt, 2001). However, for our simulations, we find that the IMBH radial displacement is not significantly affected by three-body scattering events, which we expect to represent a secondary aspect of the overall dynamics also in the case of more massive GCs ($\lesssim 6\%$ relative correction).

The negligible contribution of three-body scattering events to the IMBH displacement also implies that our results are likely to remain representative of more realistic simulations that include a non-zero fraction of primordial binaries. In fact, Trenti et al. (2007a) showed (see Section 6 in that paper) that while the presence of a central IMBH enhances the disruption rate of primordial binaries, its effect is indirect since binaries on orbits that would put them in at sufficiently close impact parameters have a low probability of reaching the IMBH without being disrupted first through three of four body encounters with other particles inside the sphere of influence of the BH. Thus, we expect that even in presence of primordial binaries the dominant energy exchanges with the IMBH would be through two-body encounters, with a modest overall enhancement of the typical displacement from the cluster center.

After providing with a physical motivation for the model in Equation (3.12), we focused on finding the set of model's parameters that best reproduces our numerical simulations. This analysis has been carried out for two distinct cases. In the first case, we considered three dimensional and mass-based quantities, getting advantage of the whole information available from the simulations. We find that the best fit model gives an overall good description of our data and generally offers a better performance when compared to related models with a lower number of free parameters (in particular, those models for which the dynamical state of the core is constrained a priori). The best-fit parameters indicate that the dynamical state of the core has to be considered in order to reproduce the data ($\beta \neq 0$ in Equation 3.12), and that the IMBH is very close to a state of complete energy equipartition with the stars in the core ($\alpha \approx 0.5$ in Equation 3.12). In the second case, we adopted projected and luminosity-weighted quantities in order to provide with a more direct tool for application to real observations. The results of the luminosity-based fit are consistent with the mass-based fit output, and are summarised by Equation (3.16), which gives the IMBH radial displacement as function of the IMBH mass and globular cluster structural parameters.

We note that our modeling is focused on the long-term dynamical evolution of the simulated clusters (we limit the analysis to the time range $4-7$ Gyr), when massive stars have already evolved off the main sequence. For this reason we expect that our conclusions would not be critically altered by different choices for the IMF, the metallicity and the stellar evolutionary tracks adopted in the simulations, since these aspects affect primarily the early-time dynamical evolution of the simulated star clusters, whose memory is erased from the system over the relaxation timescale (below 1.5 Gyr for a typical cluster). The only important exception is that, as shown in Spera et al. (2015), a different stellar evolution parameterisation would produce a different fraction of massive remnants. For example, more NSs and stellar-mass BHs would be present at late times as a consequence of a lower rate of mass loss from stellar winds, increasing the average mass in the

core, and in turn the average IMBH displacement.

Finally, to illustrate an application of Equation (3.16), we resorted to the structural parameters catalog of McLaughlin & van der Marel (2005) (which includes the majority of galactic objects) to derive the expected distribution of average IMBH radial displacements by assuming a fixed ratio for the total cluster mass to the IMBH mass. For the ratio $M_{\rm tot}/M_{\rm bh} = 10^3$, we find that the median value of the IMBH displacement is $\langle R_{\rm bh}\rangle \approx 1''$, with a few objects being significant outliers. In particular, predictions for Omega Centauri show an average offset from the centre $\langle R_{\rm bh}\rangle \approx 2.5''$. We note that given the lack of consensus on IMBH mass determinations in GCs, our assumptions rely on the uncertain extrapolation of the relations observed in galaxies between bulge and BH masses (e.g. see Gültekin et al. 2009). However, they can be promptly rescaled to arbitrary BH masses through Equation (3.16), which is derived from an analytical modeling designed exactly to bypass the limitations of running a small number of N-body simulations that can explore only a limited mass range (in our case $M_{\rm tot}/M_{\rm bh} = 400-700$, which is within the 1σ uncertainty of the scaling relation derived by Lützgendorf et al. 2013a).

In conclusion, our findings suggest that while the median displacement is unlikely to significantly affect dynamical BH mass estimates, adding tailored dynamical modeling to include the IMBH displacement would lead to more precise estimates of both BH masses and associated systematic uncertainties. In particular, generalising spherical Jeans modeling to account for a separation between the center of the stars' gravitational potential and the center of the point-mass potential generated by an IMBH would be the most useful improvement. In this framework, higher orders in the multipole expansion of the combined gravitational potential should be included in the modeling process and would potentially help in solving the tension between different interpretations of velocity dispersion data for globular clusters in which a central IMBH has been claimed to be present.

4

Long-term evolution with black holes

The level of mass segregation in the core of globular clusters has been previously proposed as a potential indicator of the dynamical constituents of the system, such as presence of a significant population of stellar-mass black holes (BHs), or even a central intermediate-mass black hole (IMBH). However, its measurement is limited to clusters with high-quality Hubble Space Telescope data. Thanks to a set of state-of-the-art direct N-body simulations with up to 200k particles inclusive of stellar evolution, primordial binaries, and varying BH/neutron stars, we highlight for the first time the existence of a clear and tight linear relation between the degree of mass segregation and the cluster structural concentration index. The latter is defined as the ratio of the radii containing 5% and 50% of the integrated light (R_5/R_{50}), making it robustly measurable without the need to individually resolve low-mass stars. Our simulations indicate that given R_5/R_{50}, the mass segregation Δm (defined as the difference in main sequence median mass between center and half-light radius) is expressed as $\Delta m/M_\odot = -1.166 R_5/R_{50} + 0.3246$, with a root-mean-square error of 0.0148. In addition, we can explain its physical origin and the values of the fitted parameters through basic analytical modeling. Such correlation is remarkably robust against a variety of initial conditions (including presence of primordial binaries and IMBHs) and cluster ages, with a slight dependence in best-fit parameters on the prescriptions used to measure the quantities involved. Therefore, this study highlights the potential to develop a new observational tool to gain insight on the dynamical status of globular clusters and on its dark remnants.

4.1 Introduction

Old ages and high stellar densities make globular clusters (GCs) natural laboratories for a range of diverse astrophysical processes (Heggie & Hut, 2003). In fact, their current stellar populations are the manifestation of more than 10 Gyr of combined stellar, dynamical, and hydrodynamical evolution, whose interplay is primarily responsible for enhanced presence of exotic objects (e.g. Bailyn, 1995), including blue stragglers stars (see e.g. Ferraro et al. 1997; Lanzoni et al. 2007) and binary pulsars (Camilo & Rasio, 2005; Benacquista & Downing, 2013). GCs have also been indicated as possible formation sites of intermediate-mass black holes (IMBHs, Portegies Zwart & McMillan 2002; Vesperini et al. 2010) and as favourable environments for mergers of dark compact objects (e.g. Samsing et al., 2014; Abbott et al., 2016b; MacLeod et al., 2016; Rodriguez et al., 2016; Samsing et al., 2017, 2018).

However, understanding the dynamical evolution of GCs remains challenging, in particular with respect to the presence and contribution of dark constituents (BHs, neutron stars) which cannot be observed directly (see e.g. Noyola et al. 2008; Lanzoni et al. 2013; Lützgendorf et al. 2015). In this context, a variety of different tracers for the BHs presence have been proposed, with one of them relying on the characterization of the long-term dynamical evolution of GCs (Gill et al., 2008; Pasquato et al., 2009; Trenti & van der Marel, 2013; Peuten et al., 2016; Bianchini et al., 2017; Weatherford et al., 2017; Arca Sedda et al., 2018; Askar et al., 2018), which is driven by the tendency of the system to evolve towards a state of

energy equipartition through two-body relaxation (see Binney & Tremaine 2008).

Because GC constituents have a spectrum of masses, the evolution toward (partial) energy equipartition causes the system to become spatially mass segregated. More massive objects become preferentially restricted toward the minimum of the gravitational potential (the cluster's central region) as they trend toward energy equipartition with lighter counterparts through gravitational two-body encounters. Correspondingly, the velocity dispersion and spatial extent of lighter-than-average stars increases. Complete energy equipartion is never reached (see Trenti & van der Marel 2013; Bianchini et al. 2016b; Spera et al. 2016) because GCs are open systems – stars that gain too much energy become unbound. The two-body relaxation time (which has a median value of $\approx 10^8$ yr for galactic GCs; Heggie & Hut 2003) is the relevant time-scale over which globular clusters undergo mass segregation, and it depends primarily on mass and radius, with compact low-mass clusters characterized by shorter relaxation times compared to extended and high-mass counterparts.

In this context, it is well established by early numerical modeling studies that massive dark remnants, and in particular IMBHs, affect mass segregation and energy equipartition, specifically quenching them (Trenti et al., 2007a; Gill et al., 2008; Pasquato et al., 2009; Trenti & van der Marel, 2013). Partial suppression of mass segregation has also be shown to be induced by a population of primordial binaries (Gill et al., 2008; Beccari et al., 2010; Pasquato et al., 2016; Webb & Vesperini, 2017), as well as by a significant presence of stellar BHs (Alessandrini et al., 2016; Peuten et al., 2016; Baumgardt & Sollima, 2017; Weatherford et al., 2017). These three different classes of objects are thought to act (either in combination or individually) by enhancing strong three-body scattering events in the GC core, which enhance the probability of imparting significant kicks to objects interacting with them almost independently of their mass. This partially redistributes core objects (preferentially more massive on average) throughout the system, thus reducing the amount of mass segregation and energy equipartion (Trenti & van der Marel, 2013).

These theoretical/numerical studies suggest that the level of mass segregation (and energy equipartion) in a GC can thus be used to infer useful information on its dynamical state and (dark) constituents. However, the measurement of such quantities is observationally challenging, mainly because it requires sufficiently high resolution images of the central crowded regions of star clusters that can resolve individual stars of low mass. While feasible and demonstrated for GCs such as NGC2298 (Pasquato et al., 2009), M10 (Beccari et al., 2010), as well as for Omega Centauri (Anderson & van der Marel, 2010; Trenti & van der Marel, 2013), in practice observational limitations restrict the mass segregation/energy equipartition dynamical analysis to the subset of galactic GCs that have relatively low densities and high quality Hubble-Space-Telescope photometry in multiple bands/epochs (see e.g., Beccari et al. 2010; Bellini et al. 2014; Webb et al. 2017; Libralato et al. 2018).

Such observational challenges highlight the need for alternative observables that can be used to characterize the dynamical state of GCs (see e.g. Bianchini et al. 2016b) and, in turn, to infer the properties of the dynamical constituents of

a broader range of galactic and extragalactic GCs. To this purpose, we analyze in this study a large set of realistic direct N-body simulations of star clusters, which includes a variety of different initial conditions and setups, searching for quantities that correlate with the degree of mass segregation once the system becomes dynamically old (i.e. old compared to its two-body relaxation timescale). We present evidence for a tight correlation between the level of mass segregation of dense stellar systems and their structural concentration, measured in a novel but easy to asses way by considering the ratio of the radii containing 5% and 50% of the projected light. The correlation is then tested for robustness against a variety of operational choices for defining mass segregation and concentration, overall demonstrating remarkable resilience and low residuals across the whole set of simulations, despite their significant diversity in initial conditions.

The paper is organized as follows. In Sec.4.2 we describe the simulations used in this work and define mass segregation and structural concentration, focusing in particular on prescriptions that can be implemented from actual GC observations. In Sec.4.3 we demonstrate the existence of the mass-segregation structural concentration correlation, and test for robustness against different observational and simulation setups. In Sec.4.4 we present a physical interpretation for this correlation by means of a simplified order-of-magnitude model. Finally, we conclude in Sec.4.5 with an outlook for future observational testing and applications of this newly discovered tool to investigate GC dynamics.

4.2 Methods

4.2.1 Numerical framework

The set of star cluster simulations used in this paper is obtained using the direct N-body integrator NBODY6 (Aarseth, 2003) inclusive of GPU support (Nitadori & Aarseth, 2012), as well as the SSE and BSE packages (originally presented in Hurley et al. 2000), which simulate stellar evolution for single and binary stars respectively.

The simulated clusters (see Table 4.1) have initial conditions sampled from a King (1966) model distribution with central dimensionless potential $W_0 = 7$ and half-mass radius $r_{\rm h,0} = 2.5$ pc, and up to $N = 200000$ particles. For the set of simulations considered in this study the adopted initial star distribution represents a fixed condition, which may potentially affect other physical processes such as the kick velocity of dark remnants (see e.g. Baumgardt & Makino 2003; Contenta et al. 2015) and, in turn, the degree of mass segregation. Despite this numerical limitation related to the computationally challenging task of running large sets of direct N-body models, we expect different values of W_0 or $r_{\rm h,0}$ to affect only the first stages of the cluster evolution, with differences in the main structural parameters becoming unimportant after a few relaxation times (Trenti et al., 2010).

Initial stellar masses are drawn from a Kroupa (2001) initial mass function (IMF) in the mass range 0.1-$100\ M_\odot$ irrespective of their radial position in the system. In fact, we do not include primordial mass segregation as its effects on the overall mass function evolution should be lost at later times, when clusters

begin losing stars via tidal stripping (see Subsec. 3.5 of Webb & Vesperini 2016). The simulations include tidal forces, computed assuming that the clusters follow circular orbits in a point-mass galactic gravitational field (see Trenti et al. 2007b for details), underfilling the tidal radius by a factor of 3.

A subset of the initial conditions include a central IMBH of 100-400$M_\odot$ which represents 0.15-0.3 per cent of the initial cluster mass (see MacLeod et al. 2016 and de Vita et al. 2018 for details of the setup). The IMBH is initialized with zero velocity at the center of mass of the system, but it is free to wander through the core as a result of dynamical interactions with other constituents. In addition, because of tidal disruption events which follow close encounters with the IMBH, its mass increases during the simulation (generally by $20-40\%$).

Compared to earlier works that characterized mass segregation (see e.g., Gill et al. 2008, Pasquato et al. 2009, Trenti & van der Marel 2013), we resort to a larger set of realistic simulations that not only include stellar evolution but also have higher number of particles. Since one debated aspect of stellar evolution is the typical velocity distribution of natal kicks imparted to dark remnants (white dwarfs, neutron stars and black holes), we employ different scenarios to investigate systems that include different retention fractions. Specifically, we assign black holes and neutron stars natal kicks drawn from the same Maxwellian distribution with a dispersion σ_* of either 1 or 2 times the initial cluster velocity dispersion, $\sigma_* = \sqrt{GM_{\rm tot}/r_{\rm hm}}$, with $r_{\rm hm}$ half-mass radius. No natal kick is given to white dwarfs. While these assumptions do not rely on a specific model of stellar evolution (see Mirabel 2017; Mapelli 2018 for recent reviews on the topic), the aim of our work is to test GCs' simulations against different retention fractions of stellar remnants, which radically affect the long-term dynamical evolution (see, e.g., Contenta et al. 2015), and the simple recipe employed is thus sufficient for our scope.

In addition to the retention fraction, the mass spectrum of stellar-mass BHs is also a critical factor influencing the dynamical evolution of the system and the development of mass segregation. Recent development in theories of supernova explosion might suggest that BHs form with masses larger than previously thought (see e.g. Fryer et al. 2012; Spera et al. 2015). To explore different scenarios in regards to this, we generate the initial conditions assuming a different metallicity Z, which in turn affects the stellar evolution packages, leading to more massive stellar BHs formed in metal-poor environment (see Hurley et al. 2000). This way we can effectively simulate conditions where BHs have masses in excess of $20M_\odot$ with the standard (and extensively validated) stellar evolution packages of NBODY6. A more rigorous treatment of stellar-BH formation is based on different population synthesis codes (see Kruckow et al. 2018; Spera et al. 2019, which naturally form BHs as massive as $50M_\odot$, in line with recent gravitational-waves detections (Abbott et al., 2016b,a, 2017). We should consider including these stellar evolution packages in future development of the present study.

Furthermore, our simulations include realizations starting with 1-10% primordial hard binaries. The initial binary fraction is defined as $f = 2n_b/(n_s+2n_b)$, with n_s and n_b number of singles and binaries, respectively. The semi-major axis for each binary pair is computed from a flat distribution in logarithmic space within

Table 4.1: Summary of N-body simulations. For each simulation (identified by a unique ID) we report (from left to right) the initial number of stars; the initial IMBH mass in $M_\odot$; the velocity dispersion of the natal kick imparted to stellar remnants σ_k normalized to the initial cluster velocity dispersion σ_*; the fraction of primordial binaries f; the metallicity Z and the number of distinct realizations of the same initial conditions ($N_{\rm sim}$). Finally, each simulation is assigned to a specific sub-GROUP, which indicates, through a self-explanatory label, the main parameter that was varied with respect to the canonical initial conditions.

ID	GROUP	N	$M_{\rm bh,0}$	σ_k/σ_*	f	Z	$N_{\rm sim}$
can50k	can	50k	-	1.0	-	0.002	4
fb1050k	bin	50k	-	1.0	0.10	0.002	1
IMBH50k	imbh	50k	100	1.0	-	0.002	1
Z50k	low-met	50k	-	1.0	-	0.001	2
kick50k	high-kick	50k	-	2.0	-	0.002	1
can100k	can	100k	-	1.0	-	0.002	7
fb01	bin	100k	-	1.0	0.01	0.002	1
fb03	bin	100k	-	1.0	0.03	0.002	1
fb05	bin	100k	-	1.0	0.05	0.002	2
fb07	bin	100k	-	1.0	0.07	0.002	1
fb10	bin	100k	-	1.0	0.10	0.002	1
imbh	imbh	100k	100	1.0	-	0.002	1
IMBH	imbh	100k	200	1.0	-	0.002	1
Z	low-met	100k	-	1.0	-	0.001	1
kick	high-kick	100k	-	2.0	-	0.002	1
kickfb05	bin & high-kick	100k	-	2.0	0.05	0.002	1
kickfb10	bin & high-kick	100k	-	2.0	0.10	0.002	1
can200k	can	200k	-	1.0	-	0.002	1
fb10200k	bin	200k	-	1.0	0.10	0.002	1
IMBH200k	imbh	200k	400	1.0	-	0.002	1
Z200k	low-met	200k	-	1.0	-	0.001	1
kick200k	high-kick	200k	-	2.0	-	0.002	1

the range 0.1-10 AU, while eccentricities are drawn from a thermal distribution. This particular choice guarantees that most of the binaries ($\gtrsim 80\%$) are not disrupted in the initial stages of evolution (see e.g. Heggie 1975; Heggie et al. 2006; Trenti et al. 2007b).

Finally, the chaotic nature of the N-body problem requires to test the robustness of our results at a statistical level. Therefore, we performed multiple simulations that represent different realizations of equivalent initial conditions in order to characterize the typical run-to-run variation of mass segregation and structural concentration.

4.2.2 Structural concentration index

In this work we introduce a novel definition for the concentration of a star cluster that can be readily applied to observations and is based on the integrated light

profile. Our structural concentration index R_5/R_{50} is defined as follows.

For each snapshot in our simulations, we consider a random projection in two dimensions and then restrict the analysis to the luminous component as identified by main-sequence stars only, including stars with mass $M \geq M_{\rm min}^{\rm MS}$, where generally $M_{\rm min}^{\rm MS} = 0$ (i.e. no lower cutoff is applied).

Considering only the main sequence stars that pass the mass cutoff, the center of the system is determined through a two step iteration: first, we compute the center of light of the system and then identify a first estimate of the projected half-light radius R_{50} (i.e. the radius that encloses half of the total light); second, we restrict the cluster to the region inside $2R_{50}$ and take the new center of light as the final center of the cluster.

Finally, we calculate the concentration index as the ratio R_5/R_{50} which is given by the projected radii enclosing 5% and 50% of the light respectively. This is our standard definition for the structural concentration, which has the following advantages:

- It is robust against confusion of low-mass stars in actual observations, as it only requires to mask effectively the light from stars brighter than main-sequence turn-off. This makes it potentially broadly applicable for galactic and nearby extragalactic globular clusters;

- Unlike the classical definition of concentration, which is the ratio of the core to the tidal radius of the system, it does not require fitting the surface brightness profile with a model to infer core and tidal radius. Therefore, it is easier to implement in the analysis of observational data, and does not suffer from possible systematic biases induced by the specific algorithm used for the King model fit.

Finally, we also adopt a mass-based approach with the aim of testing the robustness of our results as well as mimicking high-quality observations in which stars are resolved individually. In this case, in addition to the standard analysis with $M_{\rm min}^{\rm MS} = 0$, we also apply a non-zero lower cutoff for main sequence stars, which is chosen as representative of state-of-the-art Hubble Space Telescope observations (see e.g. Libralato et al. 2018). Also, the center of the system is determined using the center of mass and the structural concentration R_5/R_{50} is calculated using radii that enclose a fraction of the total projected mass instead of light.

4.2.3 Mass segregation

Different definitions have been proposed to quantify the degree of mass segregation of a stellar system. They can be broadly divided into two main approaches, with focus either on measuring the difference in mass at two given radii typically considering only main sequence stars (Gill et al., 2008), or on the difference in the radial distributions of low versus high mass objects (Alessandrini et al., 2016; Weatherford et al., 2017). For the latter, generally the "low mass" population is identified with main sequence stars, while the high-mass objects are giants or blue stragglers.

Given the potential introduction of Poisson noise in the measurement from the lower number of giants/blue stragglers in both simulated and observed GCs, we adopt the approach of measuring the difference in average main sequence mass at different cluster radii. Specifically, we define the mass segregation indicator Δm as:

$$\Delta m = \langle m \rangle_0 - \langle m \rangle_{\rm h}, \tag{4.1}$$

where $\langle m \rangle_0$ is average main-sequence stellar mass calculated at the center of the system (i.e. inside $0.1R_{50}$) while $\langle m \rangle_{\rm h}$ is calculated for main sequence stars in the radial interval $[0.8R_{50} : 1.2R_{50}]$. While our canonical approach is to consider light-based radii, when the concentration is computed with a mass-based approach, a consistent definition for R_{50} as the projected half-mass radius is also used. Also, the low-mass cut-off $M_{\rm min}^{\rm MS}$ used for computing the concentration is self-consistently adopted for the mass segregation analysis. Finally, we note that we introduce a slightly idealized treatment of the simulations, motivated by computational convenience, and we assume we can resolve single masses in binary systems.

4.2.4 Dynamical evolution overview

Due to the cumulative effects of two-body encounters, star clusters experience dynamical relaxation on a time-scale comparable with the half-mass relaxation time $t_{\rm rh} = 0.138 N r_{\rm hm}^{3/2} / \log(0.11N)$ (Spitzer, 1987). In addition, stellar evolution also has an impact on dynamics, as stars lose mass due to winds and explosive end-of-life events that ultimately lead to production of compact remnants. The gas lost by stars is generally not retained in the shallow potential well of GCs, thus perturbing the virial equilibrium and promoting expansion of the system. This naturally introduces an additional time scale in the system, independent of the relaxation time. Because of the interplay between stellar evolution and stellar dynamics, the study of the cluster's dynamical state becomes more challenging to link to fundamental physical processes and basic order-of-magnitude modeling, yet the approach clearly delivers a more realistic modeling of actual GCs compared to earlier studies of mass segregation that included gravity only (e.g., Gill et al. 2008, Pasquato et al. 2009).

In Fig.4.1, we plot the entire evolution of mass segregation and concentration up until 12.5 Gyr for selected groups of simulations. At early times, we can observe a rise in Δm as the massive stars preferentially segregate toward the center, while the concentration decreases because of the expansion induced by mass loss due to stellar evolution. After a few 10^8 yr, the main sequence turn-off has evolved to significantly lower masses, and thus the mass segregation indicator decreases in value. In turn, the stellar mass-loss rate decreases (the turn-off mass evolves slowly at later times), hence the cluster expansion decelerates and eventually contraction starts once two-body relaxation (gravothermal collapse) becomes the dominant evolutionary driver of the system. The system settles in a quasi-equilibrium long-term evolution after the first ~ 2 Gyr, and a clear trend of correlation between concentration and mass segregation emerges for all the different runs shown in the figure. The slow time evolution of Δm in Fig. 4.1

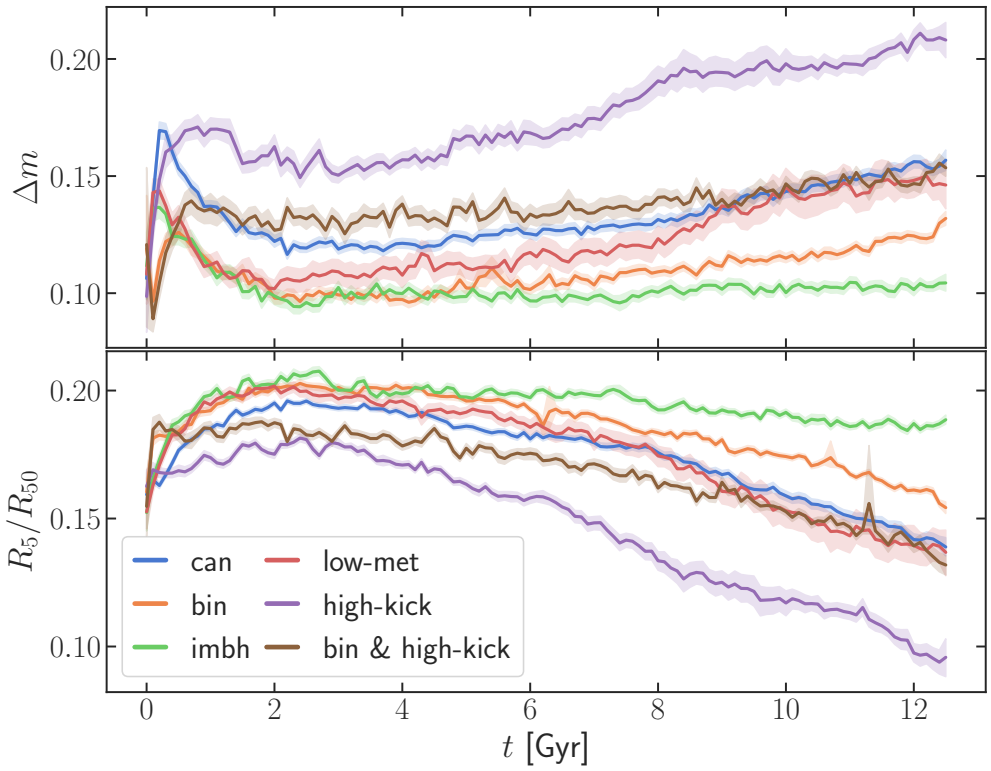

Figure 4.1: Time evolution of mass segregation (top panel) and concentration (bottom panel) for different groups of simulations (see Table 4.1). At late times, the anti-correlation between the two quantities is apparent.

is likely associated to steady mass loss from stellar evolution at late times, and was not observed in earlier studies, which reported instead a rapid settling of an equilibrium Δm value after a few relaxation times in gravity-only simulations (Gill et al. 2008, Pasquato et al. 2009), thus highlighting the importance of including stellar evolution in the modeling.

4.3 Results: mass segregation - concentration correlation

The main result of our work is summarized in Fig.4.2, which investigates the relation between structural concentration and mass segregation for old star clusters. This plot highlights for the first time that a tight correlation between the level of mass segregation and the structural concentration index (as defined in subsection 4.2.2) exists for simulations characterized by a variety of different initial conditions. The figure has been obtained from all snapshots between 7.5 and 12.5 Gyr of age and includes all the simulations in Table 4.1, clearly showing that the more concentrated the cluster, the stronger the mass segregation.

4.3.1 Linear model

To describe the correlation with the simplest meaningful model, we employ a linear model defined by

$$\frac{\Delta m}{M_\odot} = a + b\frac{R_5}{R_{50}}, \tag{4.2}$$

with a and b as free parameters.

Their values ($a = 0.3246 \pm 0.0008$ and $b = -1.166 \pm 0.005$; see top entry in Table 4.2) are determined through a Markov-Chain Monte Carlo algorithm (Salvatier et al., 2016) as follows. We consider the targeted values of mass segregation as normally-distributed with standard deviation $\sigma = 0.1$ and an expected value that is a linear function of the concentration index through Equation (4.2). Then, we evaluate the posterior distributions for the free parameters of the model, and determine the best-fit values together with the associated uncertainties from the mean, 2.5-th and 97.5-th percentiles of such distributions (see Fig.4.3).

In addition to the linear model, we also performed a fit using a power-law, which is defined as in Equation (4.2), but with an extra free parameter as exponent of the concentration index. The best-fitting power law returned is close to linear, and the Akaike information criterion* (see e.g. Liddle 2007) applied to the two different best-fit models indicates that the linear relation (AIC = 24.39) is slightly favored to describe our data compared to the power-law relation (AIC = 26.34). Hence, we consider the linear model as the preferred choice to describe the relation between mass segregation and structural concentration.

4.3.2 Time dependence

In order to measure the light-based quantities in Equation (4.2), we rely on the complete set of simulations in Table 4.1. For the specific case of Fig. 4.2, the data-points are obtained in advanced stages of the evolution, namely considering the time interval Δt between 7.5 and 12.5 Gyr. However, we also repeated the analysis at earlier times and for different sizes of the time interval (see Table 4.2). We find that a change of Δt has a marginal effect on the best-fit parameters and root mean square error, with the largest relative difference below 20%. This suggests that both mass segregation and concentration evolve with time in a strongly correlated fashion, with each simulation moving towards the upper left corner of Fig. 4.2 remaining constrained along the linear relation (4.2) (see also Fig.4.1).

Finally, we note that the spread in the level of mass segregation and structural concentration increases with time. This is evident from Fig. 4.1, where the concentration index lies in the range 0.17-0.20 at 2 Gyr and in the range 0.10-0.19 at 12 Gyr (the same trend can be noticed for the degree of mass segregation). As a consequence, even though the correlation (4.2) is not severely affected by the age of the cluster, the data-points in Fig. 4.2 present a narrower distribution in both axes at earlier times, so that the differences in the degree of mass segregation and concentration among the various simulation groups are reduced.

*According to the definition $\mathrm{AIC} = -2\ln\mathcal{L}_{\max} + 2k$, where $\mathcal{L}_{\max}$ is the maximum likelihood from the fit of a model with k degrees of freedom, the best model is the one that minimises AIC.

4.3.3 Correlation robustness

To further investigate the robustness of our results, we repeated the analysis adopting mass-based definitions of the concentration. As we restrict our study to MS stars only, we find that using mass-based quantities has no significant impact on the best-fit parameters (relative differences within 15%) but it increases the quality of the fit (lower RMSE). We interpret this as consequence of lower impact of shot noise in the definition of R_5/R_{50}, because light-based analysis is effectively carried out using only a small number of tracers (the most massive among the main sequence stars) due to the highly non-linear relation between stellar luminosity and mass ($L \approx M^4$).

In contrast, we notice that the choice of a lower cut-off in the MS significantly affects the parameters of the linear relation (4.2) (see Table 4.2). The direct effect of changing $M_{\rm min}^{\rm MS}$ is to decrease the dynamic range for main sequence mass measurements. This leads to an increase of the average stellar mass, and to a decrease of the value of mass segregation measured. Instead, the structural concentration index is not sensitive to an increase of $M_{\rm min}^{\rm MS}$ (at least to first approximation), hence if the measure of Δm decreases, then the linear relation between concentration and mass segregation becomes flatter.

4.3.4 Structural concentration index versus classical King model definition

Several definitions have been proposed in the literature to quantify the concentration in GCs (see e.g. Goldsbury et al. 2013). One of the most widely used is the ratio of the truncation radius to the core radius as defined by King (1962). The core and truncation radii are obtained by fitting the surface density (or luminosity) profile with an empirical law (see Equation 14 in that paper)[†]. When we repeat our analysis using the core radius instead of R_5, we find that the root-mean square error of the best-fit linear model significantly increases, primarily due to a clear systematic deviation from a linear relation at low values of the concentration. This further motivates and justifies the approach of resorting to the structural concentration index defined in Subsection 4.2.2 for future observational applications of the correlation.

4.3.5 Impact of different dynamical constituents on mass segregation

The panels in Fig.4.2 clearly show that different groups of initial conditions are populating different regions of the structural-concentration versus mass segregation correlation. The general trends previously noted in the literature are recovered in our study. In particular, simulations with an IMBH are characterized by both a low concentration and a low amount of mass segregation when compared to the canonical case. A similar trend is present in some of the simulations with massive stellar BHs (low metallicity ICs), while simulations where dark remnants are given large natal kicks (hence a smaller likelihood of being retained) have a

[†]Note that in case of large truncation radii, this definition of the core radius is equivalent to the radius at which the surface density (or luminosity) profile is equal to half of its central value.

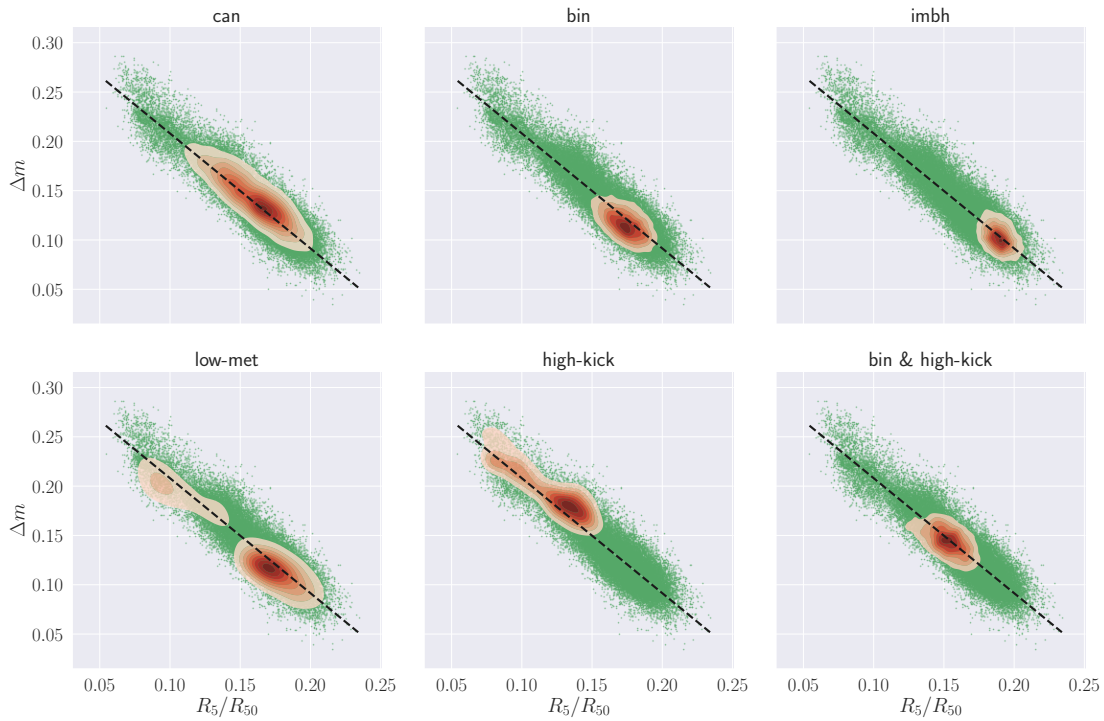

Figure 4.2: Correlation between the degree of mass segregation Δm and the concentration index R_5/R_{50} for clusters older than 7.5 Gyr. In each panel the probability density function of a single simulation group (see Table 4.1 for definitions) is over-plotted as red shaded contours against the data points from all the available simulations (green dots) and the best linear fit expressed by Eq. (4.2) (black dashed line).

higher level of mass segregation. Simulations with primordial binaries show suppression of mass segregation as well, and appear to have a slight offset from the best fit.

Further quantitative characterization of how the dynamical constituents of the system affect mass segregation and structural concentration is left to a future study.

4.4 Physical interpretation for the correlation

To understand the physical origin of the mass segregation-structural concentration correlation expressed by Equation (4.2), we develop a simplified dynamical model, which we also use to qualitatively explain the values of the best-fitting parameters derived from the data. For simplicity, we consider mass-based quantities.

First, we assume that the cluster particle distribution at late times can be described by a self-similar isothermal distribution. Under this assumption, the surface density Σ scales with the inverse of the projected radius (see Equation 4.105 in Binney & Tremaine 2008), so that the number of stars within a radial interval $[0, R]$ is

$$N(R) \propto \int_0^R \Sigma(R') R' dR' \propto R. \tag{4.3}$$

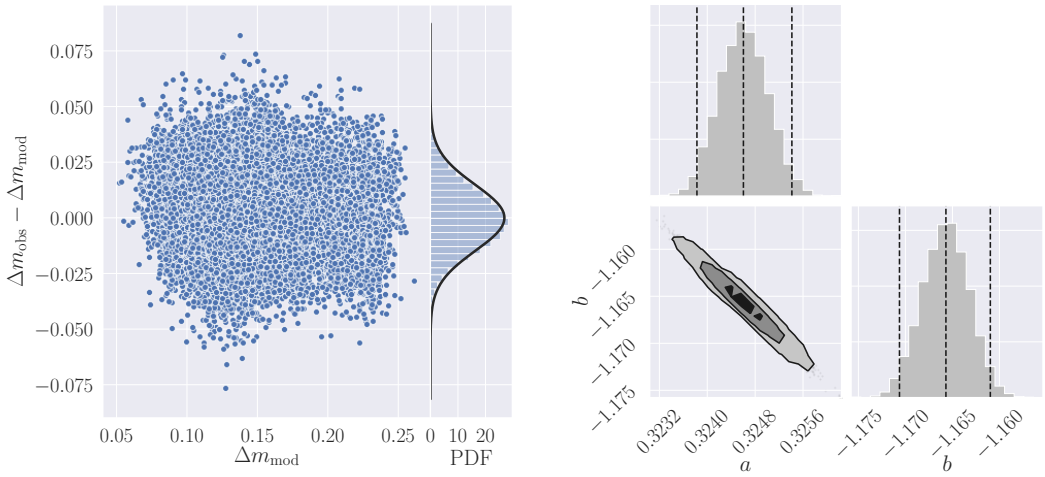

Figure 4.3: Best-fit performance. In the left panel, we plot the residuals, i.e. the difference of the mass segregation's values measured in our simulations and predicted by model (4.2), against the predicted values. We also plot the residuals' probability density distribution (PDF) and its best-fit gaussian distribution (black line). In the right panel, we show the posterior distributions for the fitting parameters of the linear model as obtained from a MCMC analysis of our simulation sample.

Table 4.2: Best-fit parameters corresponding to different observational and dynamical prescriptions used to calculate the concentration index and the amount of mass segregation for the model in Equation (4.2). For each linear model we indicate the approach used for the analysis (either light-based or mass-based); the lower mass cut-off of main sequence stars $M_{\rm min}^{\rm MS}$ in $M_\odot$; the time interval over which the linear relation is considered Δt in Gyr; the intercept (a), slope (b), and root mean square error (RMSE) of the linear fit. The first row in this table represents our canonical light-based analysis.

light	$M_{\rm min}^{\rm MS}$	Δt	a	b	RMSE
yes	-	7.5-12.5	0.3246 ± 0.0008	-1.166 ± 0.005	0.0148
yes	-	5.5-10.5	0.3437 ± 0.0011	-1.239 ± 0.006	0.0161
yes	-	10-12.5	0.3201 ± 0.0009	-1.165 ± 0.006	0.0133
no	-	7.5-12.5	0.3407 ± 0.0007	-1.285 ± 0.004	0.0096
no	-	5.5-10.5	0.3444 ± 0.0008	-1.331 ± 0.004	0.0095
no	-	10.0-12.5	0.3337 ± 0.0009	-1.227 ± 0.006	0.0096
no	0.2	7.5-12.5	0.2500 ± 0.0006	-0.935 ± 0.003	0.0085
no	0.3	7.5-12.5	0.1748 ± 0.0005	-0.649 ± 0.003	0.0078

The total mass inside the same region is given by

$$M(R) \propto \langle m \rangle_R N(R) \propto \langle m \rangle_R R, \tag{4.4}$$

where $\langle m \rangle_R$ indicates the average stellar mass inside the projected radius R. Hence, we can derive that the 5% lagrangian radius R_5 can be defined as:

$$R_5 \propto M(R_5)/\langle m \rangle_0, \tag{4.5}$$

where $M(R_5)$ is 5% of the total main-sequence mass of the cluster and we have approximated the average mass inside R_5 with $\langle m \rangle_0$ (the central value as defined in Sec 4.2.3). Similarly, we can define the relation between half-mass radius and cluster half mass, and from that we can write:

$$\frac{R_5}{R_{50}} \propto \frac{\langle m \rangle_h}{\langle m \rangle_0}. \tag{4.6}$$

Note that for an isothermal sphere without mass segregation, we would expect $R_5/R_{50} = 0.1$, while due to the presence of a flat core in actual clusters the value of R_5, which is generally close to the observational core radius, is increased to $\sim 0.3R_{50}$ (see, e.g., the observed core-to-half-light radius ratio in Fig. 3 of Trenti et al. 2010, which is a close proxy). After such empirical calibration, we can use the equation above to understand the impact of mass segregation through Eq. (4.1) and a linear expansion:

$$\frac{R_5}{R_{50}} \propto \frac{\langle m \rangle_h}{\langle m \rangle_h + \Delta m} \approx 0.3 \left(1 - \frac{\Delta m}{\langle m \rangle_h}\right), \tag{4.7}$$

where the latter is a Taylor expansion assuming small values of the ratio $\Delta m/\langle m \rangle_h$. Finally, considering that $\langle m \rangle_h \approx 0.4 M_\odot$ and rearranging the terms to follow the structure of Eq. (4.1) gives:

$$\frac{\Delta m}{M_\odot} \approx 0.4 - 1.33 \frac{R_5}{R_{50}}. \tag{4.8}$$

Despite the simplicity of the model, this equation explains both the sign (anti-correlation), i.e. negative b, and the order of magnitude of the best fitting parameters in Table 4.2 (mass-based and $M_{\rm min}^{\rm MS} = 0$).

This model is not suited for detailed quantitative analysis, because it relies on an isothermal sphere density distribution and neglects changes to the gravitational potential and particle density distribution that are induced by mass segregation. However, it is still very useful as a guide for interpretation of the data inferred from the full N-body dynamics, reinforcing the confidence in the potential use of our structural concentration index as a proxy for mass segregation. Finally, the model also suggests through Eq (4.7) that it is a change in mass segregation that induces the slow evolution of the concentration at late times observed in Fig. 4.1.

4.5 Discussion and Conclusion

In the present work we highlight for the first time the existence of a tight correlation (see Equation 4.2) between the degree of mass segregation and the concentration of dense stellar systems, as identified by proxies that can be readily compared to observations of Galactic GCs.

We presented and analyzed a new set of direct N-body simulations that include a variety of initial conditions, with particular focus on varying those dynamical constituents that are expected to mainly affect the long-term evolution of mass segregation (i.e. primordial binaries, stellar BHs and putative IMBHs). We find that the set of simulations considered do not present any significant outlier with respect to the correlation found.

In addition, we tested the robustness of the correlation against different observational prescriptions. The fit performance together with the best fit parameters for different setups is reported in Table 4.2. Among the different prescriptions, the low-mass cutoff due to the very crowded regions of GCs is the one with the most prominent impact on the parameters of the correlation. We showed how this can have a simple yet insightful explanation in terms of an order-of-magnitude model, which has been introduced in Section 4.4 to provide with a physical interpretation for the observed mass segregation-concentration correlation.

This work has important implications on the current understanding of the dynamical evolution of dense stellar systems like GCs. Because of the physical quantities adopted in our study, the linear relation (4.2) can be tested and calibrated in real observations of Galactic GCs.

Thus, this tool offers a valuable potential opportunity to infer the dynamical state of GCs through the measurement of a structural quantity like the concentration index. In fact, such quantity can be used as a proxy for mass segregation, which, in contrast, is significantly more challenging to measure even under the optimal case of high-quality space-based imaging for close Galactic GCs. In future studies we plan to validate the correlation using such observations, as well as to further exploit our set of simulations to explore the use of mass segregation as a tool to infer the dynamical constituents of old stellar clusters.

Future Perspectives

In the previous Chapter we have shown how, for a vast sample of simulations characterized by different initial conditions and considered at different ages, the concentration index is in a tight linear relation with the level of mass segregation (see de Vita et al. 2019). Such correlation offers the opportunity to infer the dynamical state of GCs through the measurement of a quantity that can be readily accessed in actual observations of Galactic (and possibly few extra-galactic) sources.

In the next future we plan to further explore the use of mass segregation as a tool to infer the dynamical constituents of old stellar clusters. To this purpose, relying on our current set of simulations (which comprises few more runs with respect to the one used in de Vita et al. 2019), we conducted a preliminary analysis that highlights the existence of a 0-th order correlation between the total black hole mass fraction in the cluster core and the degree of mass segregation (or, equivalently, the structural concentration). This correlation holds as long as the system is both dynamically relaxed and contains an old stellar population, irrespective of other parameters such as concentration, initial mass function, binary fraction. From the simulations, we derive that the BH mass fraction $\{M_{\rm BH}/M_{\rm tot}\}_{<r_5}$ defined as the ratio of the total BH mass to the total mass inside the intrinsic 5% Lagrangian radius r_5 (i.e. the radius enclosing 5% of the total mass) scales with the degree of mass segregation Δm (i.e., the difference in main sequence median mass between center and half-mass radius) as: $\{M_{\rm BH}/M_{\rm tot}\}_{<r_5} \propto \Delta m^{-3}$.

Fig. A shows the correlation between the BH mass fraction in the core and the degree of mass segregation (or the concentration index R_5/R_{50}). The data points are obtained using the entire set of available simulations (most of them are reported in Table 4.1) restricted to snapshots between 10 and 12.5 Gyr of age.

We interpolate the data from the simulations with simple power-law models in the form

$$\log\{M_{\rm BH}/M_{\rm tot}\}_{<r_5} = \alpha_{\rm ms} + \beta_{\rm ms} \log \Delta m, \tag{4.9}$$

$$\log\{M_{\rm BH}/M_{\rm tot}\}_{<r_5} = \alpha_{\rm ci} + \beta_{\rm ci} \log R_5/R_{50}. \tag{4.10}$$

Such preliminary result supports the idea of characterising the black hole content of dense stellar systems using a measurement of their dynamical state. Since mass segregation can be quantified for most Galactic globular clusters through Hubble Space Telescope observations, the correlation found makes it possible to infer the properties of the BH population in GCs, which in turn affects predictions of gravitational wave merger rates.

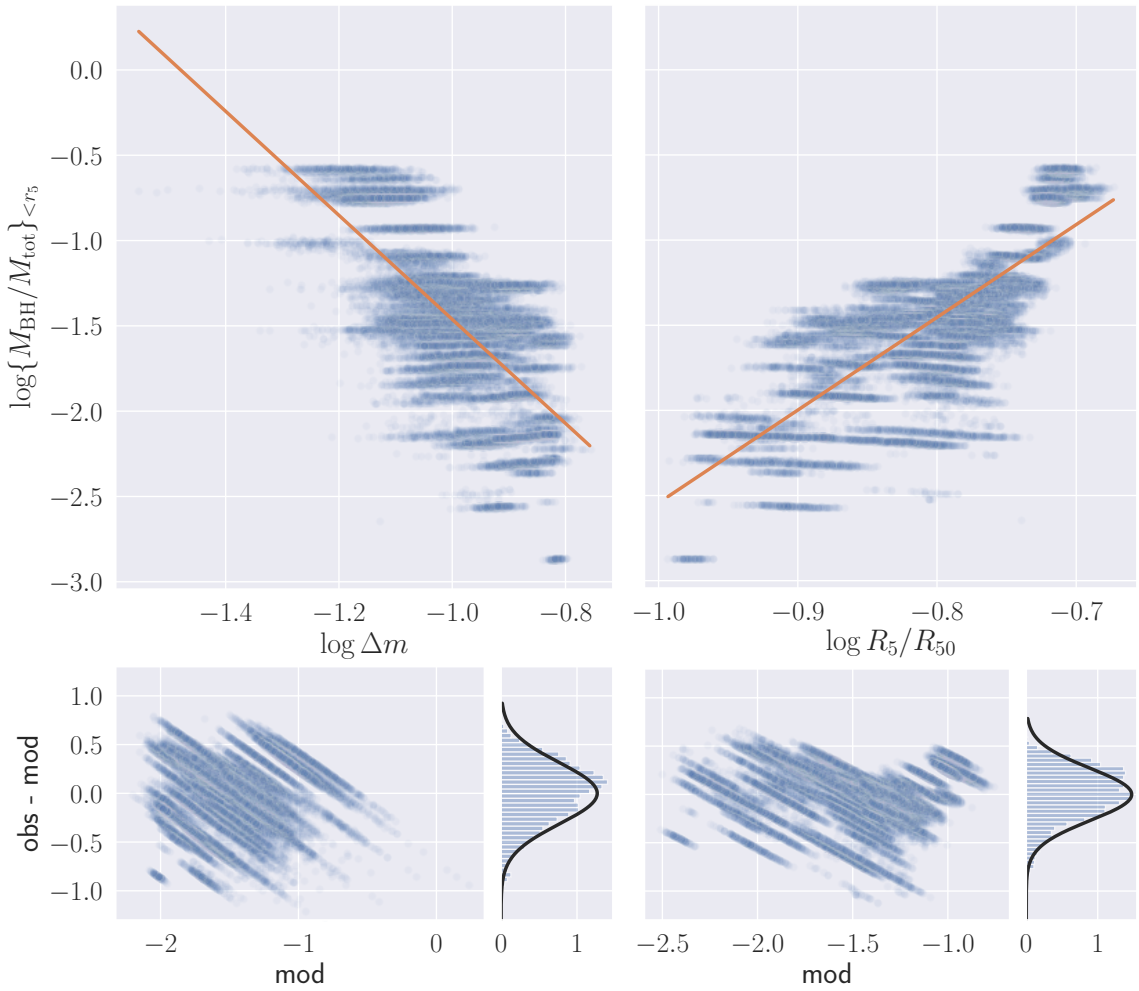

Figure A: Linear Regression of the BH mass fraction in the core as function of the degree of mass segregation (left side) and the concentration index (right side). The top panels display the linear models (orange lines) that best represents the observed data points, obtained from simulations in Table 4.1 restricted to snapshots between 10 and 12.5 Gyr of age. In the bottom panels we report the residual plots, where the residuals (y-axis) are defined as the difference in the BH mass fraction values observed in the simulations and predicted by the best fit model. The residual distributions are also shown on the right side of the residual plots together with their best fitting Gaussian distributions (solid black lines).

Conclusions

Characterising the population of black holes in dense stellar environments remains one primary goal in modern Astrophysics, with possible implications on current theories of globular cluster formation and on recent estimates of gravitational wave merging rates.

In the first part of this thesis we highlighted possible limitations in inferring the presence of IMBHs in GCs using traditional dynamical models applied to modern observations of unresolved kinematics. In particular, we produced a set of mock observations in order to test under which conditions the IMBH is recovered from the fit of a family of Jeans models to the velocity dispersion profile. Overall, our results were significantly influenced by the intrinsic stochasticity of the IFU measurements, which could lead to catastrophically-wrong estimates of the IMBH mass (about 20% of the time).

Furthermore we showed that failures in such estimates may be direct consequence of a misalignment of the cluster's gravitational centre, the IMBH position and the luminous centre determined through observations. For this reason, the aim of Chapter 3 was characterising the random motion of an IMBH around the centre of its hosting stellar system. We developed a simple model that we appled to a catalogue of 85 Galactic GCs to estimate the expected radial displacement of a putative IMBH with respect to the gravitational center. Our results suggest that, while limited for most candidates, the IMBH radial displacement might be significant (around 10 arcsec) for some clusters.

In the second part of the thesis we presented and analyzed a new set of direct N-body simulations of GCs' evolution specifically designed to include a variety of initial conditions, with particular focus on varying those dynamical constituents that are expected to mainly affect the long-term evolution of mass segregation (i.e. primordial binaries, stellar BHs and IMBHs). We highlighted for the first time the existence of a tight correlation between the degree of mass segregation and the structural concentration, as identified by quantities that can be readily compared to observations of Galactic GCs. This correlation, which has been calibrated using our simulation set, offers a valuable potential opportunity to infer the dynamical state of GCs through the measurement of a structural quantity like the concentration index. Such quantity can be used as a proxy for mass segregation, which, in contrast, is significantly more challenging to measure in actual observations.

Overall, our work reveals the central role played by black hole populations in shaping the structural properties of the hosting stellar system by affecting the level of two-body relaxation. This aspect offers support to the idea of constraining properties of a BH population by measuring the cluster's dynamical state.

Bibliography

Aarseth, S. J. 1999, *Publ. Astron. Soc. Pac.*, 111, 1333

—. 2003, Gravitational N-Body Simulations (Cambridge, UK: Cambridge University Press), 430

Abadie, J., Abbott, B. P., Abbott, R., et al. 2012, Physical Review D, 85, 102004

Abbott, B. P., Abbott, R., Abbott, T. D., et al. 2016a, Physical Review Letters, 116, 241103

—. 2016b, Physical Review Letters, 116, 061102

—. 2017, Physical Review Letters, 118, 221101

Alessandrini, E., Lanzoni, B., Ferraro, F. R., Miocchi, P., & Vesperini, E. 2016, *Astrophys. J.*, 833, 252

Anderson, J., & van der Marel, R. P. 2010, *Astrophys. J.*, 710, 1032

Arca-Sedda, M. 2016, *Mon. Not. R. Astron. Soc.*, 455, 35

Arca Sedda, M., Askar, A., & Giersz, M. 2018, *Mon. Not. R. Astron. Soc.*, 479, 4652

Ashman, K. M., & Zepf, S. E. 2008, Globular Cluster Systems (Cambridge, UK: Cambridge University Press)

Askar, A., Arca Sedda, M., & Giersz, M. 2018, *Mon. Not. R. Astron. Soc.*, 478, 1844

Askar, A., Bianchini, P., de Vita, R., et al. 2017a, *Mon. Not. R. Astron. Soc.*, 464, 3090

Askar, A., Szkudlarek, M., Gondek-Rosińska, D., Giersz, M., & Bulik, T. 2017b, *Mon. Not. R. Astron. Soc.*, 464, L36

Astropy Collaboration, Robitaille, T. P., Tollerud, E. J., et al. 2013, *Astron. Astrophys.*, 558, A33

Bañados, E., Venemans, B. P., Mazzucchelli, C., et al. 2018, *Nature*, 553, 473

Bahcall, J. N., & Wolf, R. A. 1976a, *Astrophys. J.*, 209, 214

—. 1976b, *Astrophys. J.*, 209, 214

Bailyn, C. D. 1995, Annual Review of Astronomy and Astrophysics, 33, 133

Baumgardt, H. 2017, *Mon. Not. R. Astron. Soc.*, 464, 2174

Baumgardt, H., & Makino, J. 2003, *Mon. Not. R. Astron. Soc.*, 340, 227

Baumgardt, H., Makino, J., & Ebisuzaki, T. 2004a, *Astrophys. J.*, 613, 1133

—. 2004b, *Astrophys. J.*, 613, 1143

Baumgardt, H., Makino, J., & Hut, P. 2005, *Astrophys. J.*, 620, 238

Baumgardt, H., & Sollima, S. 2017, *Mon. Not. R. Astron. Soc.*, 472, 744

Beccari, G., Pasquato, M., De Marchi, G., et al. 2010, *Astrophys. J.*, 713, 194

Belczynski, K., Kalogera, V., & Bulik, T. 2002, *Astrophys. J.*, 572, 407

Bellini, A., Anderson, J., van der Marel, R. P., et al. 2014, *Astrophys. J.*, 797, 115

Benacquista, M. J., & Downing, J. M. B. 2013, Living Reviews in Relativity, 16, 4

Bentz, M. C., Horenstein, D., Bazhaw, C., et al. 2014, *Astrophys. J.*, 796, 8

Bertin, G. 2014, Dynamics of Galaxies (Cambridge, UK: Cambridge University Press)

Bianchini, P., Norris, M. A., van de Ven, G., & Schinnerer, E. 2015, *Mon. Not. R. Astron. Soc.*, 453, 365

Bianchini, P., Norris, M. A., van de Ven, G., et al. 2016a, *Astrophys. J. Lett.*, 820, L22

Bianchini, P., Sills, A., van de Ven, G., & Sippel, A. C. 2017, *Mon. Not. R. Astron. Soc.*, 469, 4359

Bianchini, P., van de Ven, G., Norris, M. A., Schinnerer, E., & Varri, A. L. 2016b, *Mon. Not. R. Astron. Soc.*, 458, 3644

Binney, J., & Tremaine, S. 2008, Galactic Dynamics: Second Edition (Princeton University Press)

Camilo, F., & Rasio, F. A. 2005, in Astronomical Society of the Pacific Conference Series, Vol. 328, Binary Radio Pulsars, ed. F. A. Rasio & I. H. Stairs, 147

Cappellari, M., & Emsellem, E. 2004, *Publ. Astron. Soc. Pac.*, 116, 138

Casertano, S., & Hut, P. 1985, *Astrophys. J.*, 298, 80

Chen, C. W., & Chen, W. P. 2010, *Astrophys. J.*, 721, 1790

Chiosi, C., & Maeder, A. 1986, *Ann. Rev. Astron. Astrophys.*, 24, 329

Contenta, F., Varri, A. L., & Heggie, D. C. 2015, *Mon. Not. R. Astron. Soc.*, 449, L100

Czerny, B., You, B., Kurcz, A., et al. 2016, *Astron. Astrophys.*, 594, A102

de Vita, R., Bertin, G., & Zocchi, A. 2016, *Astron. Astrophys.*, 590, A16

de Vita, R., Trenti, M., Bianchini, P., et al. 2017, *Mon. Not. R. Astron. Soc.*, 467, 4057

de Vita, R., Trenti, M., & MacLeod, M. 2018, *Mon. Not. R. Astron. Soc.*, 475, 1574

—. 2019, *Mon. Not. R. Astron. Soc.*, 485, 5752

Falcke, H., Körding, E., & Markoff, S. 2004, *Astron. Astrophys.*, 414, 895

Farrell, S. A., Servillat, M., Pforr, J., et al. 2012, *Astrophys. J. Lett.*, 747, L13

Ferrarese, L., & Merritt, D. 2000, *Astrophys. J. Lett.*, 539, L9

Ferraro, F. R., Paltrinieri, B., Fusi Pecci, F., et al. 1997, *Astron. Astrophys.*, 324, 915

Forbes, D. A., & Bridges, T. 2010, *Mon. Not. R. Astron. Soc.*, 404, 1203

Foreman-Mackey, D., Hogg, D. W., Lang, D., & Goodman, J. 2013, *Publ. Astron. Soc. Pac.*, 125, 306

Fryer, C. L., Belczynski, K., Wiktorowicz, G., et al. 2012, *Astrophys. J.*, 749, 91

Gebhardt, K., Bender, R., Bower, G., et al. 2000, *Astrophys. J. Lett.*, 539, L13

Ghez, A. M., Salim, S., Weinberg, N. N., et al. 2008, *Astrophys. J.*, 689, 1044

Gieles, M., Balbinot, E., Yaaqib, R., et al. 2017, ArXiv e-prints, arXiv:1709.06874

Gieles, M., & Zocchi, A. 2015, *Mon. Not. R. Astron. Soc.*, 454, 576

Giersz, M. 1998, *Mon. Not. R. Astron. Soc.*, 298, 1239

Giersz, M., Leigh, N., Hypki, A., Lützgendorf, N., & Askar, A. 2015, *Mon. Not. R. Astron. Soc.*, 454, 3150

Gies, D. R., & Bolton, C. T. 1986, *Astrophys. J.*, 304, 371

Gill, M., Trenti, M., Miller, M. C., et al. 2008, *Astrophys. J.*, 686, 303

Goldsbury, R., Heyl, J., & Richer, H. 2013, *Astrophys. J.*, 778, 57

Grindlay, J. E., Heinke, C., Edmonds, P. D., & Murray, S. S. 2001, Science, 292, 2290

Gültekin, K., Richstone, D. O., Gebhardt, K., et al. 2009, *Astrophys. J.*, 698, 198

Haggard, D., Cool, A. M., Heinke, C. O., et al. 2013, *Astrophys. J. Lett.*, 773, L31
Harris, W. E. 1996, *Astron. J.*, 112, 1487
—. 2010, ArXiv e-prints, arXiv:1012.3224
Haster, C.-J., Antonini, F., Kalogera, V., & Mandel, I. 2016, *Astrophys. J.*, 832, 192
Heggie, D., & Hut, P. 2003, The Gravitational Million-Body Problem: A Multidisciplinary Approach to Star Cluster Dynamics (Cambridge, UK: Cambridge University Press)
Heggie, D. C. 1975, *Mon. Not. R. Astron. Soc.*, 173, 729
Heggie, D. C., Trenti, M., & Hut, P. 2006, *Mon. Not. R. Astron. Soc.*, 368, 677
Hertz, P., & Grindlay, J. E. 1983, *Astrophys. J.*, 275, 105
Hobbs, G., Lorimer, D. R., Lyne, A. G., & Kramer, M. 2005, *Mon. Not. R. Astron. Soc.*, 360, 974
Hurley, J. R. 2007, *Mon. Not. R. Astron. Soc.*, 379, 93
Hurley, J. R., Pols, O. R., & Tout, C. A. 2000, *Mon. Not. R. Astron. Soc.*, 315, 543
Hurley, J. R., Tout, C. A., & Pols, O. R. 2002, *Mon. Not. R. Astron. Soc.*, 329, 897
Jalali, B., Baumgardt, H., Kissler-Patig, M., et al. 2012, *Astron. Astrophys.*, 538, A19
Kamann, S., Husser, T.-O., Brinchmann, J., et al. 2016, *Astron. Astrophys.*, 588, A149
King, I. 1962, *Astron. J.*, 67, 471
King, I. R. 1966, *Astron. J.*, 71, 64
Kızıltan, B., Baumgardt, H., & Loeb, A. 2017, *Nature*, 542, 203
Konstantinidis, S., Amaro-Seoane, P., & Kokkotas, K. D. 2013, *Astron. Astrophys.*, 557, A135
Kroupa, P. 2001, *Mon. Not. R. Astron. Soc.*, 322, 231
Kruckow, M. U., Tauris, T. M., Langer, N., Kramer, M., & Izzard, R. G. 2018, *Mon. Not. R. Astron. Soc.*, 481, 1908
Lanzoni, B., Dalessandro, E., Ferraro, F. R., et al. 2007, *Astrophys. J.*, 663, 267
Lanzoni, B., Mucciarelli, A., Origlia, L., et al. 2013, *Astrophys. J.*, 769, 107
Larson, R. B. 2000, in ESA Special Publication, Vol. 445, Star Formation from the Small to the Large Scale, ed. F. Favata, A. Kaas, & A. Wilson, 13
Libralato, M., Bellini, A., van der Marel, R. P., et al. 2018, *Astrophys. J.*, 861, 99
Liddle, A. R. 2007, *Mon. Not. R. Astron. Soc.*, 377, L74
Lützgendorf, N., Gebhardt, K., Baumgardt, H., et al. 2015, *Astron. Astrophys.*, 581, A1
Lützgendorf, N., Kissler-Patig, M., Noyola, E., et al. 2011, *Astron. Astrophys.*, 533, A36
Lützgendorf, N., Kissler-Patig, M., Gebhardt, K., et al. 2013a, *Astron. Astrophys.*, 552, A49
Lützgendorf, N., Kissler-Patig, M., Neumayer, N., et al. 2013b, *Astron. Astrophys.*, 555, A26
Lynden-Bell, D. 1967, *Mon. Not. R. Astron. Soc.*, 136, 101
MacLeod, M., Trenti, M., & Ramirez-Ruiz, E. 2016, *Astrophys. J.*, 819, 70
Madau, P., & Rees, M. J. 2001, *Astrophys. J. Lett.*, 551, L27
Mandel, I., Brown, D. A., Gair, J. R., & Miller, M. C. 2008, *Astrophys. J.*, 681, 1431

Mapelli, M. 2018, ArXiv e-prints, arXiv:1809.09130
McLaughlin, D. E., & van der Marel, R. P. 2005, *Astrophys. J. Suppl.*, 161, 304
Merloni, A., Heinz, S., & di Matteo, T. 2003, *Mon. Not. R. Astron. Soc.*, 345, 1057
Merritt, D. 2001, *Astrophys. J.*, 556, 245
Mezcua, M. 2017, ArXiv e-prints, arXiv:1705.09667
Mezcua, M., Roberts, T. P., Sutton, A. D., & Lobanov, A. P. 2013, *Mon. Not. R. Astron. Soc.*, 436, 3128
Miller, M. C., & Hamilton, D. P. 2002, *Mon. Not. R. Astron. Soc.*, 330, 232
Miller-Jones, J. C. A., Wrobel, J. M., Sivakoff, G. R., et al. 2012, *Astrophys. J. Lett.*, 755, L1
Mirabel, F. 2017, *New Astron. Rev.*, 78, 1
Nitadori, K., & Aarseth, S. J. 2012, *Mon. Not. R. Astron. Soc.*, 424, 545
Noyola, E., Gebhardt, K., & Bergmann, M. 2008, *Astrophys. J.*, 676, 1008
Noyola, E., Gebhardt, K., Kissler-Patig, M., et al. 2010, *Astrophys. J. Lett.*, 719, L60
Orosz, J. A., McClintock, J. E., Aufdenberg, J. P., et al. 2011, *Astrophys. J.*, 742, 84
Pasquato, M., Miocchi, P., Won, S. B., & Lee, Y.-W. 2016, *Astrophys. J.*, 823, 135
Pasquato, M., Trenti, M., De Marchi, G., et al. 2009, *Astrophys. J.*, 699, 1511
Pasquini, L., Brucalassi, A., Ruiz, M. T., et al. 2012, *Astron. Astrophys.*, 545, A139
Peuten, M., Zocchi, A., Gieles, M., Gualandris, A., & Hénault-Brunet, V. 2016, *Mon. Not. R. Astron. Soc.*, 462, 2333
Peuten, M., Zocchi, A., Gieles, M., & Hénault-Brunet, V. 2017, *Mon. Not. R. Astron. Soc.*, 470, 2736
Pooley, D., & Rappaport, S. 2006, *Astrophys. J. Lett.*, 644, L45
Portegies Zwart, S. F., Baumgardt, H., Hut, P., Makino, J., & McMillan, S. L. W. 2004a, *Nature*, 428, 724
Portegies Zwart, S. F., Dewi, J., & Maccarone, T. 2004b, *Mon. Not. R. Astron. Soc.*, 355, 413
Portegies Zwart, S. F., & McMillan, S. L. W. 2002, *Astrophys. J.*, 576, 899
Quinlan, G. D. 1996, *New Astron.*, 1, 35
Ricotti, M., Parry, O. H., & Gnedin, N. Y. 2016, *Astrophys. J.*, 831, 204
Robertson, D. R. S., Gallo, L. C., Zoghbi, A., & Fabian, A. C. 2015, *Mon. Not. R. Astron. Soc.*, 453, 3455
Rodriguez, C. L., Chatterjee, S., & Rasio, F. A. 2016, *Phys. Rev. D*, 93, 084029
Rodriguez, C. L., Pattabiraman, B., Chatterjee, S., et al. 2015, ArXiv e-prints, arXiv:1511.00695
Salvatier, J., Wiecki, T., & Fonnesbeck, C. 2016, PeerJ Computer Science, 2:e55
Samsing, J., MacLeod, M., & Ramirez-Ruiz, E. 2014, *Astrophys. J.*, 784, 71
—. 2017, *Astrophys. J.*, 846, 36
—. 2018, *Astrophys. J.*, 853, 140
Silk, J., & Arons, J. 1975, *Astrophys. J. Lett.*, 200, L131
Spera, M., Mapelli, M., & Bressan, A. 2015, *Mon. Not. R. Astron. Soc.*, 451, 4086
Spera, M., Mapelli, M., Giacobbo, N., et al. 2019, *Mon. Not. R. Astron. Soc.*, 485, 889
Spera, M., Mapelli, M., & Jeffries, R. D. 2016, *Mon. Not. R. Astron. Soc.*, 460, 317

Spitzer, L. 1987, Dynamical evolution of globular clusters (Princeton, NJ, Princeton University Press, 1987, 191 p.)

Spitzer, Jr., L. 1969, *Astrophys. J. Lett.*, 158, L139

Stiefel, E., K. P. 1965, Journal für die reine und angewandte Mathematik, 218, 204

Strader, J., Chomiuk, L., Maccarone, T. J., et al. 2012, *Astrophys. J. Lett.*, 750, L27

Trenti, M., Ardi, E., Mineshige, S., & Hut, P. 2007a, *Mon. Not. R. Astron. Soc.*, 374, 857

Trenti, M., Heggie, D. C., & Hut, P. 2007b, *Mon. Not. R. Astron. Soc.*, 374, 344

Trenti, M., & Hut, P. 2008, ArXiv e-prints, arXiv:0806.3950

Trenti, M., Padoan, P., & Jimenez, R. 2015, *Astrophys. J. Lett.*, 808, L35

Trenti, M., & van der Marel, R. 2013, *Mon. Not. R. Astron. Soc.*, 435, 3272

Trenti, M., Vesperini, E., & Pasquato, M. 2010, *Astrophys. J.*, 708, 1598

Ulvestad, J. S., Greene, J. E., & Ho, L. C. 2007, *Astrophys. J. Lett.*, 661, L151

van de Ven, G., van den Bosch, R. C. E., Verolme, E. K., & de Zeeuw, P. T. 2006, *Astron. Astrophys.*, 445, 513

van der Marel, R. P. 2003, in Bulletin of the American Astronomical Society, Vol. 35, American Astronomical Society Meeting Abstracts, 1370

van der Marel, R. P., & Anderson, J. 2010, *Astrophys. J.*, 710, 1063

Vesperini, E., McMillan, S. L. W., D'Ercole, A., & D'Antona, F. 2010, *Astrophys. J. Lett.*, 713, L41

Vesperini, E., & Trenti, M. 2010, *Astrophys. J. Lett.*, 720, L179

Vink, J. S. 2018, *Astron. Astrophys.*, 619, A54

Vishniac, E. T. 1978, *Astrophys. J.*, 223, 986

Volonteri, M. 2010, *Astron. Astrophys. Rev.*, 18, 279

Volonteri, M., Haardt, F., & Madau, P. 2003, *Astrophys. J.*, 582, 559

Volonteri, M., & Rees, M. J. 2005, *Astrophys. J.*, 633, 624

Wang, L., Spurzem, R., Aarseth, S., et al. 2016, *Mon. Not. R. Astron. Soc.*, 458, 1450

Weatherford, N. C., Chatterjee, S., Rodriguez, C. L., & Rasio, F. A. 2017, ArXiv e-prints, arXiv:1712.03979

Webb, J. J., & Vesperini, E. 2016, *Mon. Not. R. Astron. Soc.*, 463, 2383

—. 2017, *Mon. Not. R. Astron. Soc.*, 464, 1977

Webb, J. J., Vesperini, E., Dalessandro, E., et al. 2017, *Mon. Not. R. Astron. Soc.*, 471, 3845

Zocchi, A., Gieles, M., & Hénault-Brunet, V. 2017, *Mon. Not. R. Astron. Soc.*, 468, 4429

—. 2018, ArXiv e-prints, arXiv:1806.02157